Imaging the Assembly of the Staphylococcal Pore-Forming Toxin α-Hemolysin

A dissertation by

James R. Thompson

Submitted to the University of Oxford in partial satisfaction of the requirements for the degree of DOCTOR OF PHILOSOPHY

Major-Subject: Physical Chemistry

Wadham College

January 2009

Abstract

Imaging the Assembly of the Staphylococcal Pore-Forming Toxin α-Hemolysin
James R. Thompson - Wadham College - University of Oxford
Submitted for the degree of Doctor of Philosophy in Hilary Term 2009

α-Hemolysin is a pore-forming toxin secreted by pathogenic *Staphylococcus aureus*. Its spontaneous oligomerization and assembly into a trans-bilayer β-barrel pore is a model for the assembly of many other pore-forming toxins. It is studied here *in vitro* as a means to probe general membrane protein oligomerization and lipid bilayer insertion. This thesis details the results of experiments to develop and implement a novel *in vitro* lipid bilayer system, Droplet-on-Hydrogel Bilayers (DHBs) for the single-molecule imaging of α-hemolysin assembly.

Chapter 2 describes the development of DHBs and their electrical characterization. Experiments show the detection of membrane channels in SDS-PAGE gels post-electrophoresis and DHBs use as a platform for nanopore stochastic sensing.

Chapter 3 describes the engineering and characterization of fluorescently-labelled monomeric α-hemolysin for use in protein assembly imaging experiments described in chapter 6.

Chapter 4 describes the characterization of DHB lipid fluidity and suitability for single-molecule studies of membrane protein diffusion. In addition, a novel single-particle tracking algorithm is described.

Chapter 5 describes experiments demonstrating simultaneous electrical and fluorescence measurements of α-hemolysin pores embedded within DHBs. The first multiple-pore stochastic sensing in a single-lipid bilayer is also described.

Chapter 6 describes experiments studying the assembly of α-hemolysin monomers in DHBs. Results show that α-hemolysin assembles rapidly into its oligomeric state, with no detection of long-lived intermediate states.

Declaration

The work described in this thesis was carried out between September 2005 and January 2009, in the laboratory of Dr. Mark Wallace at the Chemistry Research Laboratory of the University of Oxford. All the work described within this thesis is entirely my own. Collaborative experimental assistance was given by Dr. Andrew J. Heron, Dr. Amy E. Mason and Dr. Bríd Cronin. This work has not been submitted previously for any other degree at the University of Oxford or any other university. Publications stemming from this work are detailed prior to the document contents.

James R. Thompson

January 2009

Abbreviations

AFM	atomic force microscopy
αHL	α-hemolysin / α-toxin
ATP	adenosine triphosphate
B. anthracis	*Bacillus anthracis*
BAPTA	1,2–bis(o-aminophenoxy)ethane–N,N,N',N'–tetraacetic acid
βCD	β-cyclodextrin
BIS-TRIS	2–[bis(2-hydroxyethyl)imino]–2–(hydroxymethyl)–1,3–propanediol
BLAST	basic local alignment and search tool
BLM	black lipid membrane
βME	2-mercaptoethanol
βPFT	β-pore-forming toxin
CCD	charge-coupled detector
CKF	Chung-Kennedy filter
DHB	droplet-on-hydrogel bilayer
DIB	droplet interface bilayer
D_{lat}	lateral diffusion coefficient
DMF	dimethylformamide
DMPC	1,2–dimyristoyl–*sn*–glycero–3–phosphocholine
DMSO	dimethylsulphoxide
DNA	deoxyribonucleic acid
dNTP	deoxyribonucleotide triphosphate
DOPC	1,2–dioleoyl–*sn*–glycero–3–phosphocholine
DPhPC	1,2–diphytanoyl–*sn*–glycero–3–phosphocholine
DTT	dithiothreitol
E. coli	*Escherichia coli*
EDTA	ethylenediamminetetraacetic acid
EGTA	ethylene glycol tetraacetic acid
EM	electron microscopy / electron micrograph
emCCD	electron-multiplying charge-coupled detector
ESI	electrospray ionisation
FPLC	fast protein liquid chromatography

FRET	Förster resonance energy transfer
γCD	γ-cyclodextrin
GFP	green fluorescent protein
hβCD	heptakis(2,3,6-tri-O-methyl)-β-cyclodextrin
HEPES	4–(2–hydroxyethyl)–1–piperazineethanesulfonic acid
HPLC	high-performance liquid chromatography
IASD	4–acetamido–4'–[(iodoacetyl)amino]stilbene–2,2'–sulphonic acid
IMAC	immobilised metal-affinity chromatography
IPTG	isopropyl β-*D*–1–thiogalactopyranoside
IVTT	coupled-*in vitro* transcription and translation
LB	Luria-Bertani
Luk	Leukocidin protein
MD	molecular dynamics
MES	2-(N-morpholino)ethanesulphonic acid
MOPS	3-(N-morpholino)propanesulphonic
MQ	MilliQ Water
MSD	mean-squared displacement
Na_iPO_4	sodium phosphate buffer
Nd:YAG	neodymium:yttrium aluminium garnet
NIH	National Institutes of Health
NTA	nitrilotriacetic acid
PAGE	polyacrylamide gel electrophoresis
PALM	photoactivated localization microscopy
PBS	phosphate buffered saline
PCR	polymerase chain reaction
PCT	photoinduced charge transfer
PDA	photodiode array
PDB	protein databank
PEG	polyethylene glycol
PEGm	maleimido-polyethylene glycol
PMMA	polymethyl methacrylate
POPC	1–palmitoyl–2–oleoyl–*sn*–glycero–3–phosphocholine

POPE	1–palmitoyl–2–oleoyl–*sn*–glycero–3–phosphoethanolamine
POPG	1–palmitoyl–2–oleoyl–*sn*–glycero–3–[phospho-*rac*–(1–glycerol)]
POPS	1–palmitoyl–2–oleoyl–*sn*–3–glycerophosphoserine
PSF	point-spread function
PVL	Panton-Valentine Leukocidin toxin
QD	colloidal nanocrystalline semiconductor - quantum dot
RCSB	Research Collaboratory for Structural Bioinformatics
RNA	ribonucleic acid
RP	reverse-phase
rRBCM	rabbit red blood cell membranes
S. aureus	*Staphylococcus aureus*
SCOP	Structural Classification of Proteins - Database
SDS	sodium dodecyl sulphate
SLB	supported lipid bilayer
smFRET	single-molecule Förster resonance energy transfer
SNARE	SNAP and NSF attachment receptors
SPFF	sulphonyl-propyl fast-flow
SPT	single particle tracking
TCEP	tris(2–carboxyethyl)phosphine
TE	TRIS-EDTA
TICT	twisted intramolecular charge transfer
TIR	total internal reflection
TIRF	total internal reflection fluorescence
TIRFm	total internal reflection fluorescence microscopy
TOF	time-of-flight
TRICINE	N–(2–hydroxy–1,1–bis(hydroxymethyl)ethyl)glycine
TRIS	2–amino–2–hydroxymethyl–propane–1,3–diol
TRITC-DHPE	N–(teramethylrhodamine–6–thiocarbamoyl)– –1,2–dihexadecanoyl–*sn*–glycero–3–phosphoethanolamine
UV	ultra-violet light
Vis	visible light

List of Publications

Articles and Letters

1. Heron, A. J., Thompson, J. R., Mason, A. E., and Wallace, M. I. Direct detection of membrane channels from gels using water-in-oil droplet bilayers. *J. Am. Chem. Soc. 129*, 51 (2007), 16042–16047.

2. Thompson, J. R., Heron, A. J., Santoso, Y., and Wallace, M. I. Enhanced stability and fluidity in droplet on hydrogel bilayers for measuring membrane protein diffusion. *Nano Lett. 7*, 12 (2007), 3875–3878.

3. Heron, A. J., Thompson, J. R., Cronin, B., and Wallace, M. I. Simultaneous measurement of ionic current and fluorescence from single protein pores. *J. Am. Chem. Soc.* 131 (2009), 1652–1653.

Reviews

1. Thompson, J. R. Hot off the press: Review. *Mol. Biosystems 3* (2007), 814–814.

2. Bayley, H., Cronin, B., Heron, A., Holden, M., Hwang, W., Syeda, R., Thompson, J., and Wallace, M. Droplet interface bilayers. *Mol. Biosystems 4*, 12 (2008), 1191–1208.

Intellectual Property

Heron, A.J., Holden, M.A., Thompson, J.R., and Wallace, M.I.
Bilayers *UK Priority Application*, (0716264.7).

Acknowledgments

Firstly, I must thank Dr. Mark Wallace for his choosing me for the D.Phil studentship position. That decision in August of 2005 undoubtedly changed my life forever for the better, and for that I will be eternally grateful. It has been immense fun starting out in a new lab. Mark has had to sacrifice his beloved experiments in return for more paperwork, and I know it's been difficult for him to see us enjoying ourselves in the lab doing his so-called 'crazy' experiments, when he would really rather be there with us. His guidance during these last three years has been immeasurable, and I hope he can be as proud of this work as I am, given that none of it would have been possible without his help and patience. I only hope I can be fortunate enough to work with such similarly talented scientists in the future. The early help Prof. Hagan Bayley gave us in starting this project was also invaluable, and undoubtedly without which, we would have had a much harder time getting the project off the ground.

Thank you very much to my examiners Dr. Richard Berry and Dr. Justin Molloy. I very much appreciate your time given to read and travel to Oxford to examine me.

To all the members of our burgeoning group and that of Hagan's, thank you also for your scientific help. Our collaborations, comedy-moments and coffee breaks have made this last three years some of the best of my life. These experiments wouldn't have been possible without the collaborative help of Dr. Andrew Heron, Dr. Amy E. Mason and Dr. Bríd Cronin. Working on these research projects with you has been immense fun, and I think extremely fruitful.

To my 'Thesis Task Force', thanks for reading my early drafts through to the final product. My early drivel was transformed by you guys into a document I am extremely proud of. Thank you individually to my friends Dr. Sebastian '∇-Roy' Leptihn, Dr. Amy 'Tron-Q' Mason, Protodoctor 1st Class Lydia Harriss, Anne 'Hämmer-rôge' Hammerstein,

Doyle Bramhall II (for his music) and in particular Dr. Bríd 'Q-Bríd' Cronin for her immense help with the final stages of research in this D.Phil and repeated critical reading of my thesis manuscript.

Perpetual thanks go to my Mum, Dad, Lucy, Sam and Charlie for supporting me. I am forever indebted to my parents for giving me my education. I hope this work goes some way to proving it wasn't all in vain.

Maria, cara mia, grazie mille. Grazie per avere letto la mia tesi, sono in debito con te!!! Good luck with your D.Phil, I hope you find it as enjoyable an experience as I did!

For
Janet and David Thompson

Contents

1 General Introduction **1**

1.1 α-Hemolysin (α-Toxin) . . . 2

1.1.1 α-Hemolysin Pore-Formation . . . 3

1.1.2 α-Hemolysin Evolution . . . 8

1.1.3 The Postulated Mechanism of Assembly . . . 9

1.2 Lipid Bilayer Membranes . . . 10

1.2.1 General Overview . . . 10

1.2.2 Lipid Bilayers . . . 11

1.2.2.1 Supported Lipid Bilayers . . . 12

1.2.2.2 Langmuir-Blodgett Technique Lipid Bilayer Derivatives . . . 16

1.2.2.3 New Methods . . . 18

1.2.2.4 Protein Incorporation into *In Vitro* Lipid Bilayers. . . . 18

1.3 Introduction to Single-Molecule Biological Measurements . . . 19

1.4 Fluorescence . . . 20

1.5 Single-Molecule Fluorescence Microscopy at Room Temperature . . . 22

1.5.1 TIRF microscopy . . . 23

1.5.1.1 Cyanine Dye Photophysics . . . 26

1.5.1.2 Cation-Chelating Fluorophores . . . 27

1.5.2 Single-Particle Tracking . . . 29

1.6 Single-Channel Electrical Recording . . . 30

1.6.1 Stochastic Sensing . . . 30

2 Droplet-on-Hydrogel Bilayers **32**

2.1 Droplet Bilayers Introduction . . . 32

2.1.1 Historical Background . . . 32
2.1.2 The Droplet-on-Hydrogel Bilayer . . . 33
2.1.3 Physical Characteristics of DHBs . . . 35
2.1.3.1 Lipid Bilayer Longevity . . . 35
2.1.3.2 Interfacial Chemistry in DHBs . . . 36
2.2 Results . . . 38
2.2.1 Lipid Bilayer Capacitance . . . 38
2.2.2 DHB Manipulation . . . 39
2.2.3 SDS Electrophoresis of Membrane Channel Proteins . . . 41
2.2.4 α-Hemolysin Gel Scanning . . . 41
2.2.5 Detection of Low Concentration Membrane Channels in Gels . . . 43
2.2.6 Stochastic Sensing and Analyte Detection with DHBs . . . 44
2.2.7 Electrical Recording of Other Membrane Channels . . . 47
2.3 Discussion . . . 47
2.4 Conclusions . . . 49
2.5 Materials and Methods . . . 50
2.5.1 General Methods . . . 50
2.5.2 *In vitro* transcription and translation of proteins . . . 50
2.5.3 Electrophoresis of IVTT proteins . . . 50
2.5.4 Extraction and Electrophoresis of Crude Membrane Preparations from *E. coli* . . . 51
2.5.5 Porin-expressing and Porin-free *E. coli* Gel Scanning . . . 51
2.5.6 DHB gel scanning . . . 52
2.5.7 Electrical measurements and bilayer imaging . . . 52

3 Engineering α-Hemolysin for Single-Molecule Fluorescence Imaging 53
3.1 Introduction . . . 53
3.1.1 Experimental Design and Theoretical Considerations . . . 54
3.1.1.1 Fluorophore Selection Rationale . . . 54
3.1.1.2 Structural and Functional Considerations in Labelling . . . 56
3.1.1.3 Labelling Chemistry . . . 59
3.2 Results . . . 60

3.2.1 Engineering of a Suitable Protein Construct 60
3.2.1.1 PCR 60
3.2.1.2 Protein Activity Verification 61
3.2.1.3 Overexpression Trials 63
3.2.2 Cysteine Reactivity Assay 65
3.2.3 Large-Scale Purification and Labelling 67
3.2.4 Bulk Characterization of Labelled Monomeric α-Hemolysin 69
3.2.4.1 Labelling α-Hemolysin Heptamers during IMAC 71
3.3 Discussion 73
3.4 Conclusions 74
3.5 Materials and Methods 75
3.5.1 Materials 75
3.5.2 Cloning and Overexpression 75
3.5.3 IMAC 76
3.5.4 Hemolytic Assays 77
3.5.5 Disulphide Bond Reduction and Gel Filtration 77
3.5.6 Labelling and Cation Exchange 77
3.5.7 Bulk Characterization 78
3.5.8 Heptamer Labelling 78
3.5.9 Protein Storage 79

4 Protein and Lipid Diffusion in Droplet-on-Hydrogel Bilayers 80
4.1 Introduction 80
4.2 Results 82
4.2.1 Droplet-on-Hydrogel Bilayer Characterization 82
4.2.2 α-Hemolysin Analysis 86
4.3 Discussion 86
4.4 Conclusions 87
4.5 Materials and Methods 88
4.5.1 Materials 88
4.5.2 Supported Lipid Bilayers 88
4.5.3 Droplet-on-Hydrogel Bilayers 89

4.5.4 Protein Preparation . . . 89
4.6 Tracking experiments . . . 91
4.6.1 Fluorophore Tracking Algorithm . . . 92
4.6.1.1 Initial Image Analysis . . . 92
4.6.1.2 Spot Detection . . . 93
4.6.1.3 Track Reconstruction . . . 93
4.7 Data Analysis . . . 95
4.7.1 Lateral Diffusion Coefficient Calculations . . . 95
4.7.2 Population Multi-Component Analysis . . . 95

5 Simultaneous Fluorescence and Electrical Recording in Droplet-on-Hydrogel Bilayers 97

5.1 Introduction . . . 97
5.1.1 Optical Patch-Clamping and *In Vitro* Measurements . . . 98
5.1.2 Experimental Introduction . . . 99
5.1.3 Calcium Indicator Dyes . . . 100
5.2 α-Hemolysin Tracking Experiments . . . 101
5.3 Parallel Optical Stochastic Detection of Single-Molecules . . . 103
5.4 Membrane Protein Concentration in DHBs . . . 105
5.5 Discussion . . . 106
5.6 Conclusions . . . 107
5.7 Materials and Methods . . . 108
5.7.1 Materials . . . 108
5.7.2 Protein Preparation . . . 108
5.7.3 DHB Methods . . . 109
5.7.4 Electrical Recording . . . 110
5.7.5 Fluorescence Imaging . . . 110

6 Imaging α-Hemolysin Assembly 111

6.1 Introduction . . . 111
6.1.1 A Summary of Hypothetical Models of Assembly . . . 112
6.1.2 α-Hemolysin Protomers Bind to Phosphocholine Lipid Monolayers and Diffuse Laterally . . . 116

6.1.3 The Evidence for a Prepore Intermediate . . . 118
6.1.3.1 Evidence for Prepores in other Pore-Forming Toxins . . . 120
6.2 Experimental Objectives . . . 121
6.3 Results . . . 124
6.3.1 Initial α-Hemolysin Observations . . . 124
6.3.1.1 Lipid Bilayer Binding and Dissociation . . . 124
6.3.2 Elucidation of Complex Stiochiometry through Photobleaching and Spot-Intensity Analysis . . . 127
6.3.3 Direct Observation of Insertion of α-Hemolysin Channels into DHBs . 133
6.3.3.1 Calcium-Flux Imaging with Single-Molecule Fluorescence Localization - Probing Prepore→Pore Conversion . . . 134
6.4 Discussion . . . 136
6.5 Materials and Methods . . . 139
6.5.1 Materials . . . 139
6.5.2 Protein handling . . . 139
6.5.3 DHB Methods . . . 140
6.5.4 Imaging and Microscopy . . . 140
6.5.5 Electrical Recording . . . 141
6.5.6 Single-Particle Tracking . . . 141
6.5.7 Spot Intensity Analysis . . . 141
6.5.8 Photobleaching Analysis . . . 142

7 Conclusions **144**
7.1 Current Experiments . . . 145
7.2 Future Prospects . . . 145

Bibliography **148**

8 Appendix **178**
8.1 Gene Sequences . . . 178
8.2 Apparatus Details . . . 180
8.3 Patch-Clamp Amplification Details . . . 181

Chapter 1

General Introduction

Membrane proteins are responsible for some of the most fundamental biological processes. Such processes include chemotaxis [251], ATP generation [18], nervous signal transduction [197] and intercellular signalling [221]. They are ubiquitous in all kingdoms of life, and are found in viruses [81, 215]. This ubiquity combined with involvement in varied biological processes has made them the source of much research worldwide. They are also industrial targets of research, where membrane proteins represent a large proportion of pharmaceutical targets [205].

Many membrane proteins exist as obligate oligomers. Therefore, they may only function as a complex or remain in a natured state as a complex. These oligomers are either homomeric or heteromeric, and in the majority of cases must be directly inserted into the lipid bilayer by cellular machinery, evolutionarily conserved in nature [173]. Often signal sequences cotranslated with the functional protein direct the nascent polypeptide chain to the Sec translocon. The translocon exists in the innermost membrane of bacteria [89], or the endoplasmic reticulum in eukaryotes. It forms a conduit channel through which the protein is inserted laterally into the lipid bilayer. This process has been shown to require energy input in bacteria and plants [271]. When a protein is inserted into the lipid bilayer, its subsequent folding to form the correct conformation is presumably driven by minimisation of the free energy in the polypeptide chain [63], as is the case for other water-soluble proteins.

The study of membrane proteins *in vitro* requires that the protein is reconstituted from its native folded state in a lipid bilayer and manipulated in aqueous solution. Thereafter, the protein must be reconstituted into an artificial lipid bilayer. The overexpression, recovery

and reconstitution of natured intrinsic membrane proteins from an expressing organism is usually very difficult [12, 83]. This is one reason for the comparatively small amount of high-resolution X-ray crystallographic information for membrane proteins versus water-soluble proteins. To date (January 2009), there are in existence only 179 unique membrane proteins with known three-dimensional structure [293], in comparison to 44015 separate structures in total stored in the RCSB Protein Data Bank (PDB) [223].

Experiments with membrane proteins able to catalyse their own insertion into the lipid bilayer provide a more straightforward means to not only overexpress and reconstitute the protein into a lipid bilayer *in vitro*, but also to perform downstream functional experiments. It is for this reason that experiments studying the model pore-forming toxin α-hemolysin of *Staphylococcus aureus* are of particular value to the study of membrane proteins in general. This project aimed to understand in greater detail the means by which a membrane protein can oligomerize and insert a transmembrane domain into the lipid bilayer. The work describes efforts to develop, characterize and use a novel artificial lipid bilayer system for the imaging of the assembly pathway of α-hemolysin at the single-molecule level.

1.1 α-Hemolysin (α-Toxin)

As part of the human nasopharyngeal flora *Staphylococcus aureus* is a commensal, but can become pathogenic. It is responsible for a large proportion of nosocomial infections, and now certain strains are classed as 'superbugs' due to their increasing antibiotic resistance [174]. Upon adherence of the Gram-positive bacterium to extracellular matrix surface proteins, it can begin to colonise tissues [72, 187].

Toxins secreted by the bacterium upon infection, of which α-hemolysin is one, are responsible for a range of tissue damage and elicit a varied immune response [174]. In certain instances α-hemolysin sepsis can be lethal [174]. In human erythrocytes, α-hemolysin induces cell lysis due to osmotic imbalance [22], and on T-lymphocytes it induces necrosis or apoptosis [68]. It is however inactive against granulocytes [275]. Low titres of α-hemolysin are also tolerable by lymophocytes [127]. Certain lymphocytes are able to internalize α-hemolysin pores through endocytosis, thought to prevent cell lysis by minimising the osmotic imbalance [127]. Thereafter, the toxin is exocytosed in exosomal-like particles, which are extremely resistant to degradation [127].

α-Hemolysin has been adopted as the archetypal pore-forming toxin, not least due to the long history of study in a purified form, but also because of its relatively straightforward handling in the laboratory and relatively weak toxicity to humans [113]. It belongs to a fold of proteins termed β-pore-forming toxins (βPFTs) (SCOP - 56958), and to the protein superfamily of leukocidins. These proteins all form β-barrel transmembrane pores on lipid bilayers of target cells through the oligomerization of protomeric subunits secreted into solution by the bacterium. These membranes generally contain phosphatidylcholine lipids [23]. This process forms pores allowing the cellular contents to diffuse through into the bacterial milieu. It also often leads to lysis of the target cells through the disruption of the cellular osmotic balance with its environment. This causes the release of cellular cargo, which can be taken up by the pathogen for its own survival.

Curiously, rabbit erythrocytes show greatly enhanced susceptibility to lysis by α-hemolysin compared to human erythrocytes [113]. This is thought to be due to the presence of a specific receptor which the monomer can bind to preferentially, enhancing the rate of oligomerization. However, to date no such receptor has been isolated.

1.1.1 α-Hemolysin Pore-Formation

The general topology of the β-PFTs can be described as being 'Ig-like', a typical greek-key fold. The oligomer protomers have a β-sandwich core, with a β-barrel formed from a β-hairpin contributed from each protomer of the oligomer. The leukocidins are often said to have the general form of a mushroom, with a large water-soluble cap domain protruding from the lipid bilayer on the extracellular side.

Given the large quantity of β-sheet in the protein, it is highly thermodynamically stable and extremely soluble in aqueous solution (∼0.3 mM) [249]. Circular dichroism shows that the core protomer undergoes no significant diversion from its β-structure during oligomerization and conformational change to form the mature pore in deoxycholate [249, 268]. Indeed, so stable is the structure that it can form oligomers when N- and C- terminal halves are co-translated as separate fragments, or if they are mixed post-translationally [287]. As a membrane-embedded oligomer the structure is extremely stable, remaining unaffected by high salt concentrations (1 M monovalent salt), basic pH (pH 12) and chaotropic agents (SDS) [21, 77]. Only through heating the oligomer in SDS at concentrations higher than the CMC above ∼65°C will it dissociate into monomer

[180, 285]. Indeed, this stability has enabled the exploitation of the pores for biotechnological applications at high-temperatures [146]. The general structural features of the pore and its protomer subunits are now reviewed (Figures 1.1 and 1.2).

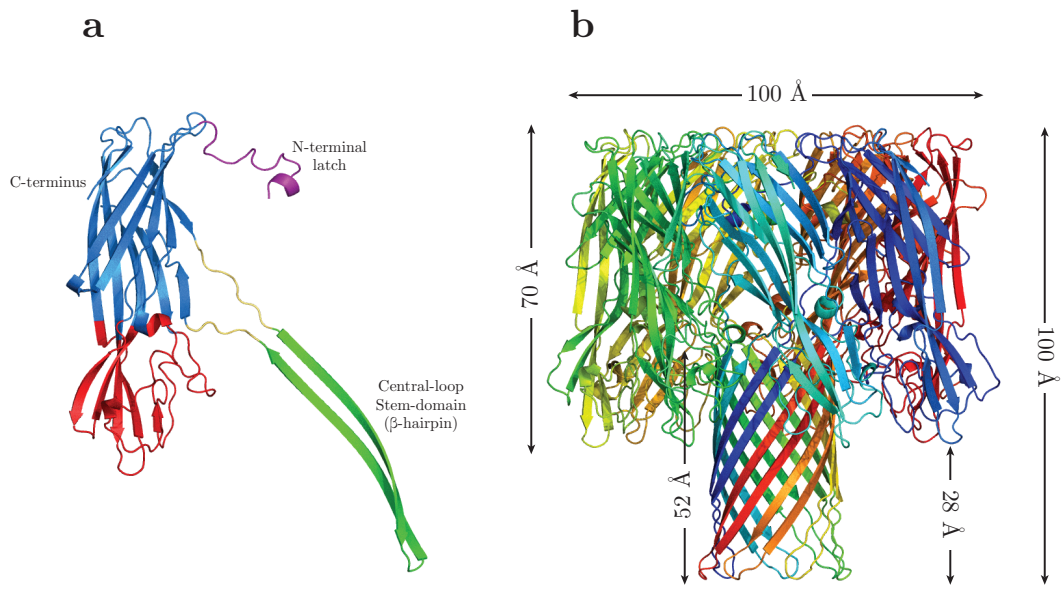

Figure 1.1: *α-Hemolysin representations illustrating the domain architecture and dimensions of the complex (PDB code 7ahl). (A) A protomer subunit from the α-hemolysin heptamer rendered as a cartoon. Here the cap domain is illustrated in blue, the rim-domain in red, the triangle region in yellow, the central loop stem-domain in green and the N-terminal latch in purple. Each protomer subunit in the pore is equivalent. (B) The α-hemolysin heptamer rendered as a cartoon. Here the seven protomer subunits comprising the α-hemolysin pore are illustrated as separate colours. The dimensions of the pore are illustrated by the arrows. The figures were created using PyMol, Delano Scientific, USA.*

The oligomeric state of the mature pore was thought to be a hexamer for the majority of 20^{th} century [23, 249]. However, current evidence suggests the oligomer consists of seven subunits. Key to this shift in thinking was the successful crystallization and elucidation of the pore structure in 1996 [249]. Since the advent of single-channel electrical recording, capable of measuring the conductance of individual pores, the electrical properties of α-hemolysin have been examined in detail [17, 66, 146, 156, 182]. Over 90% of pores belong to a well-defined single conductance distribution [182]. Recently, the heptameric state of the protein has been attributed to this high conductance value through computational simulations of ion conductance [3, 50, 201]. The large percentage of pore conductances in this category, coupled with crystal structures [79, 90, 249], subsequent imaging of oligomers by atomic force microscopy (AFM) [41, 70], biochemical evidence of the oligomeric state [156, 285] and single-molecule counting of subunits through photobleaching [57] indicate that the predominant

oligomeric state is heptameric.

Lower conductance values than the peak value described by Menestrina have been observed [182]. Whilst these lower conductance states are observed less frequently ($\lesssim$ 10% of pores), they have been attributed to a possible hexamer. Since the publication of the crystal structure, a low-resolution AFM study of oligomers in lipid bilayers reported a preponderance for densely hexagonally packed α-hemolysin oligomers with roughly six-fold symmetry [55]. This study avoided the use of any detergent during the oligomerization process, dissimilar to the other stoichiometric measurements except for that of Krasilnikov *et al.* [156]. Other work has gone on to predict the hexameric state of the oligomer by computational means, justified by a theoretical appraisal of the feasibility of the α-hemolysin protomer β-hairpins being able to form a 12-stranded barrel [76]. Given the contradictory evidence for the viability of a hexameric state of α-hemolysin in lipid bilayers, its existence cannot be ruled out.

The crystal structure of the pore illustrates the five key domains of the protein responsible for its binding to lipid bilayers, oligomerization and pore insertion [79, 249] (Figure 1.1A). The cap domain forms the water-facing peak of the protein, which is the region of the protein exposed to the extracellular side of the target cell. The rim-domain forms the portion of the protein in contact with the lipid bilayer, containing a large number of aromatic residues [79, 249]. The triangle region forms the link between the β-sandwich core of the protomers and the central loop stem-domain. The mutation of particular residues in this link between the protein's β-sandwich core and the central loop stem-domain has been shown to abolish pore forming ability entirely [249, 283]. The central loop stem-domain is a β-hairpin which comprises two of the β-strands of the 14-stranded β-barrel. The β-hairpins predominantly form hydrogen bonds with their neighbouring strands, creating the β-barrel. The N-terminal latch attaches to the lumen of the vestibule cavity of the corresponding protomer subunit, clockwise from its position. The C-terminus faces the bulk solvent on the outside of the cap domain.

The heptameric pore measures roughly $\sim$100 Å in length in all three dimensions. The β-barrel penetrates directly through the two leaflets of a lipid bilayer to make a water-filled pore, 14 Å wide at its narrowest constriction in the vicinity of the top of the β-barrel (Figure 1.2). Each protomer subunit buries approximately a third of its solvent-accessible surface in contacting the other protomers in the structure. Residues critical for pore formation and

hemolytic activity such as His^{35}, His^{48}, Asp^{24} and Asp^{100} are all present at the interprotomer contacts [157, 183, 249, 283]. This illustrates the key role of the contact between protomers in the assembly process of the pore.

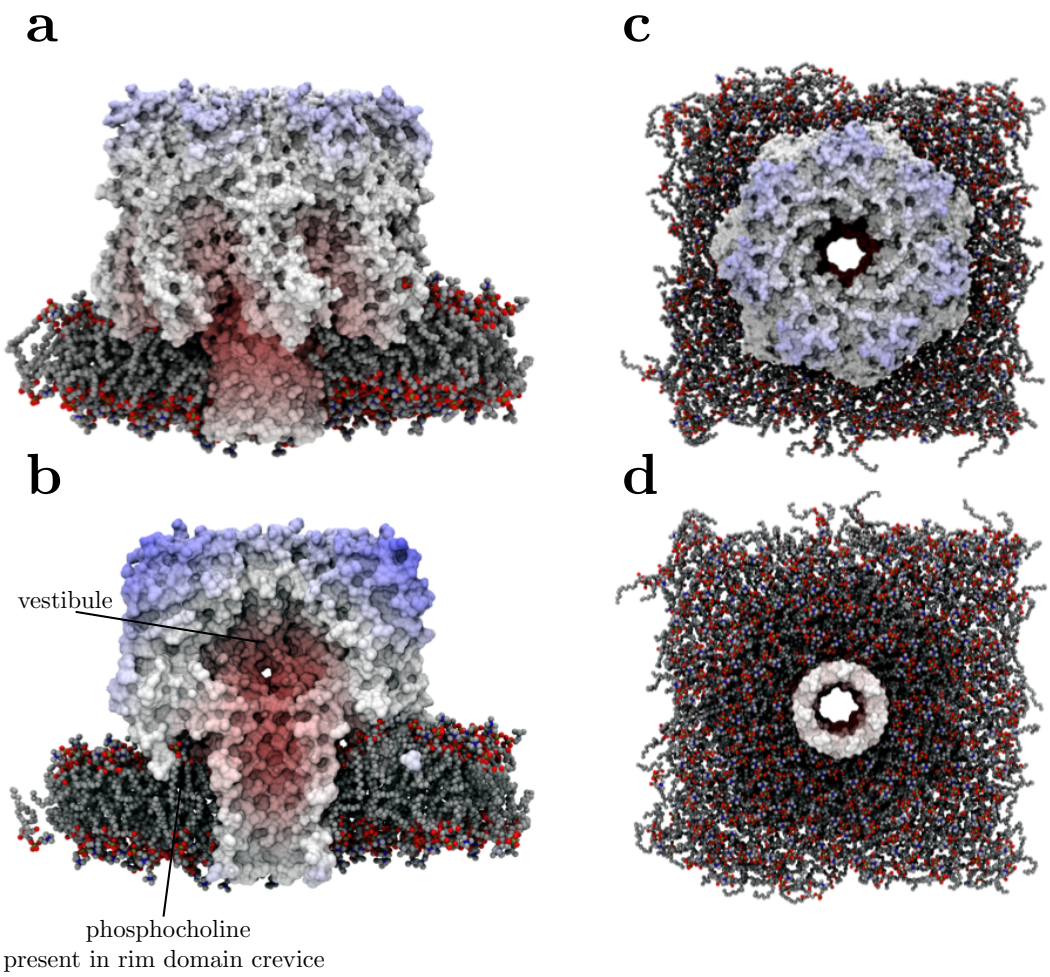

Figure 1.2: *Simulated atomistic trajectories of α-hemolysin in a DMPC lipid bilayer (courtesy of Dr. Syma Khalid, University of Southampton). α-hemolysin (PDB code 7ahl) was placed in a simulated DMPC lipid bilayer and allowed to relax for 10 ns with no restraints on any species inside the established lateral boundary for the lipid bilayer. (A) A slice through half of the lipid bilayer illustrates the depth of the rim-domain into the lipid bilayer. (B) A slice through the heptameric pore and lipid bilayer. The vestibule cavity is illustrated, as well as the head-group of a DMPC lipid resident in the rim-domain crevice. (C) The entire pore visualised from the top, showing the entrance to the pore from the cap domain. (D) The β-barrel exit underneath the lipid bilayer showing the water-filled pore penetrating the entire lipid bilayer. Figures were rendered using the Tachyon ray tracing engine by John Edward Stone, in VMD [125].*

The oligomerization of the monomer is inhibited if it is incubated with phosphatidylethanolamine, phosphatidylserine, phosphatidylglycerol or phosphatidylinositol liposomes [291]. The strict requirement for phosphatidylcholine to catalyse oligomerization to form a heptameric pore has been demonstrated through the co-crystallization of the

protein with phosphatidylcholine lipids [79]. Cation-π interactions and water-mediated hydrogen bonding with phosphatidylcholine are shown in a crevice situated in rim-domain formed by Tyr^{182}, Arg^{200} and Trp^{179}. A representation of the protein embedded in a dimyristoyl phosphatidylcholine (DMPC) lipid bilayer is shown (Figure 1.2).

To date, no X-ray crystal structure exists for the water-soluble monomeric precursor of α-hemolysin secreted by *Staphylococcus aureus*. An analogous structure for the close genetic relative bi-component leukocidin pore F-class subunit (LukF) is however available [204]. The only major differences in the two structures are the relative locations of the central loop stem-domain and the N-terminal latch domain (Figure 1.3). These domains are folded back into the core β-sandwich structure of the LukF protein. The α-hemolysin water-soluble monomer is thought to be almost identical in structure, given the very similar physiological properties of the two proteins [16, 138, 204]. A detailed comparison of the two structures is made in Chapter 3 in the context of the fluorescent-labelling of α-hemolysin monomers.

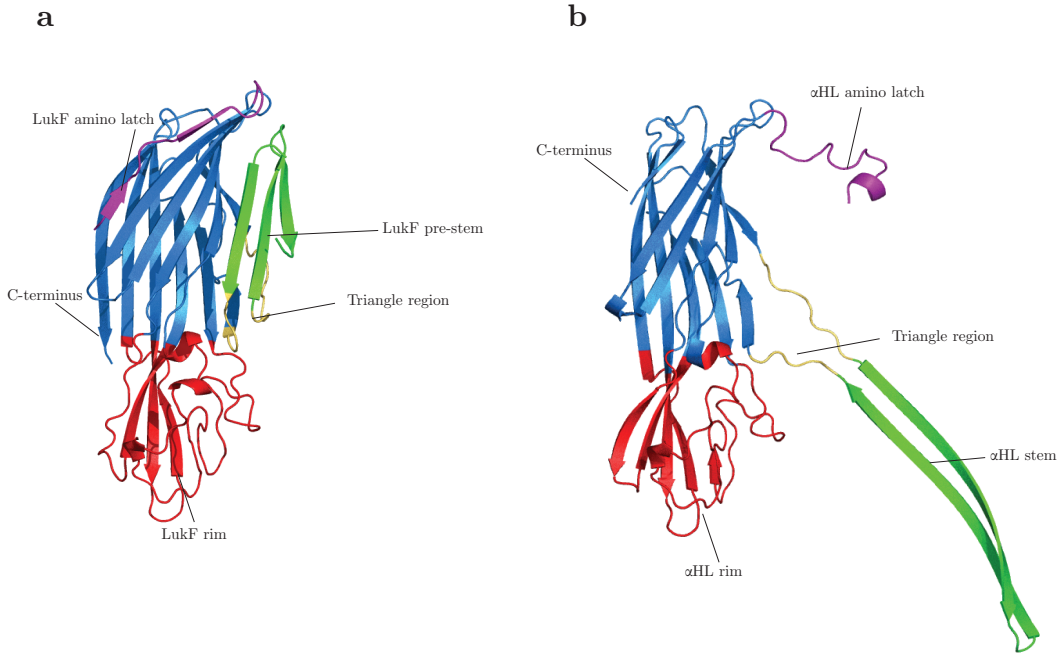

Figure 1.3: *(A) The LukF monomer crystal structure (PDB code 1lkf) [204]. (B) A protomer subunit of the heptameric α-hemolysin crystal structure (PDB code 7ahl) [249]. Here, the key domain rearrangements of the central loop stem-domain and the amino latch are clear. The figure was created using PyMol, Delano Scientific, USA.*

1.1.2 α-Hemolysin Evolution

The α-hemolysin gene (*hly*, NCBI Entrez Gene ID = 5776959) is found on the *Staphylococcus aureus* chromosome [210]. It is expressed following bacterial colonisation of the host in response to growth with a wide range of other toxins [23]. The other major class of βPFT secreted in concert with α-hemolysin are the bi-component leukocidins, which are the Panton-Valentine leukocidin (PVL) and leukocidin (Luk) proteins [192]. Both PVL and Luk differ from α-hemolysin in that they require two different types of subunit to form. Subunits must both come from the so-called F class, and the S class. As their name suggests, they are hemolytic towards leukocytes but not erythrocytes in humans [253]. In terms of functionality and sequence, leukocidin and α-hemolysin are the most similar toxins.

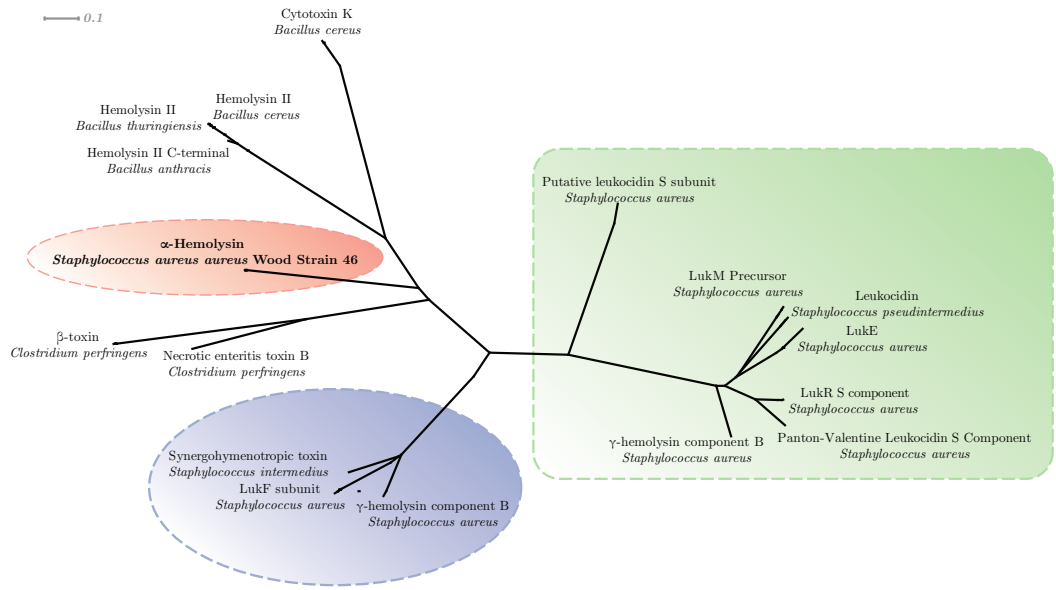

Figure 1.4: *A phylogenetic tree illustrating the evolutionary similarity of many closely related homologous toxic agents to α-hemolysin. Units in evolutionary distance terms, between 0 and 1. The phylogenetic tree is rooted by α-hemolysin's primary amino acid sequence derived from the Wood Strain 46 strain of Staphylococcus aureus (Red). Blue indicates F-class subunits and relatives, green indicates S-class subunits and relatives. Tree derived from NCBI BLAST search of all known bacterial genomes and their phage (phage hits not shown). Dendrogram generated using Dendroscope 1.4 by Daniel H. Huson, University of Tübingen, Germany from an NCBI BLASTp Newick tree.*

α-hemolysin has evolved divergently from a common ancestor shared with many other βPFTs, leading to high primary amino acid sequence homology with many other toxins from closely-related pathogens and commensals. This class of toxin can be found in Gram-positive bacteria including *Bacillus cereus, Bacillus anthracis, Bacillus thuringiensis, Clostridrium perfringens* and Staphylococci including *Staphylococcus intermedius* and the

origin of the protein of interest in this work, *Staphylococcus aureus*. A simple BLASTp (Basic Local Alignment and Search Tool - Proteins) search yields many tens of proteins already in sequence databases hosted by the National Institutes of Health (NIH, USA). The closest primary sequence analogues are displayed in a radial phylogenetic tree, rooted by *Staphylococcus aureas* Wood Strain 46 α-hemolysin (Figure 1.4).

α-hemolysin's evolutionary heritage places it in close proximity to a number of key toxins from major human pathogens. Information regarding its assembly should therefore be applicable to other βPFTs in general.

1.1.3 The Postulated Mechanism of Assembly

A conserved mode of assembly has been suggested to be shared for both α-hemolysin and leukocidin [139]. **(i.)** The water-soluble α-hemolysin monomer is secreted by the bacterium into the host. **(ii.)** The monomeric protein binds to a target membrane [23]. **(iii.)** The monomers diffuse whilst adsorbed to the cell membrane and interact to assemble into a ring-shaped complex termed a prepore. **(vi.)** Upon prepore formation, a spontaneous conformational change is triggered, causing each protomer to insert its central loop stem-domain into the lipid bilayer forming a trans-bilayer β-barrel.

The sensitivity of a cell to the action of the toxin is thought to be governed by an as yet unknown receptor [16]. However, caveolin has been implicated in certain cell types [278]. Nevertheless, the α-hemolysin monomer is able to bind to artificial lipid bilayers and vesicles *in vitro* [6, 70, 73, 156] as well as lipid monolayers [33].

The interaction of the monomers on the lipid bilayer is the least well characterized process in the assembly pathway [16]. The presence of an abundance of information suggesting there may be a kinetically competent prepore intermediate existing between the membrane-adsorbed monomer and the heptameric pore states, has led to the convergence of theories on the assembly pathway [16, 70, 151, 282, 285, 286, 288]. The evidence for a prepore intermediate has also been studied by similar experiments in other pore-forming toxins, such as pneumolysin [267], perfringolysin O [56, 111, 120, 121], streptolysin [112], anthrax protective antigen [150, 185, 248] and the leukocidins of *Staphylococcus aureus* [199]. These experiments all indicated that the protomeric monomers, which make up the mature pores, come into contact to form a ring-shaped structure prior to penetration of the transmembrane domain.

The nature of the prepore to pore conversion in wild-type α-hemolysin, or a variant which is not conformationally constrained, has yet to be studied. This process is examined in depth in Chapter 6.

1.2 Lipid Bilayer Membranes

1.2.1 General Overview

Lipid bilayer membranes are conserved in all domains of nature. They are non-covalent supramolecular assemblies of amphiphilic lipid molecules which serve to compartmentalise the cell or intracellular organelles. Through envelopment of an entire cell (plasma membrane) or organelle, they serve as a mediator of the control of selective transfer of molecules across the membrane. They are comprised of two asymmetric leaflets, with phospholipids being the most abundant lipids. Phospholipids are not used for the direct storage of energy as in the case of triglycerides. Instead, their assembly as a bilayer allows a barrier to form between the inside and outside of a cell or compartment. This facilitates the establishment of gradients of ions and protons, and hence electrical charge. This electrical charge can be used for important processes in energy generation, intercellular signal transduction and hence nervous communication. Plasma membranes also serve as a host for multiple recognition molecules (peripheral membrane proteins) and anchors for extracellular matrices. Along with hosting important enzymes for cellular metabolism (integral membrane proteins), they serve as a conduit for the import and export of molecular species with the cell.

Phospholipids in bacterial and eukaryotic membranes are derived from one of two core components linking the head-group to the fatty acyl-chains. These cores are either glycerol or sphingosine. Phosphoglycerides, which are the lipids used in the experiments in this thesis, are linked to the fatty acyl chains and phosphoric acid by ester bonds. The phosphate moiety is then linked through another ester bond to an alcohol, commonly serine, ethanolamine, choline, glycerol or inositol.

The most common lipid used in this thesis is 1,2–diphytanoyl–*sn*–glycero–3–phosphocholine (DPhPC). This lipid resembles the lipids of archaea in that it has methyl groups decorating the saturated acyl chains. However, unlike archaeal lipids, the acyl chains are esterified to the head-group instead of having an ether linkage. The structures of lipids used in experiments in this thesis are shown (Figure 1.5).

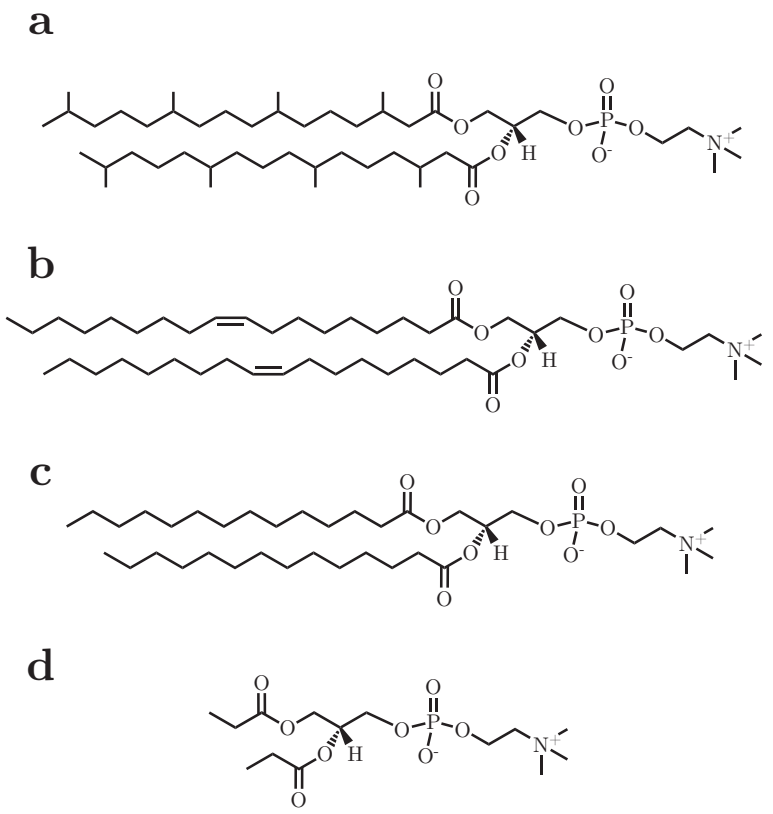

Figure 1.5: *Structures of phosphocholine lipids mentioned in this thesis. (A) The structure of 1,2–diphytanoyl–sn–glycero–3–phosphocholine (DPhPC). (B) The structure of 1,2–Dioleoyl–sn–glycero–3–phosphocholine (DOPC). (C) The structure of 1,2–dimyristoyl–sn–glycero–3–phosphocholine. (D) The structure of dipropanoyl–sn–glycero–3–phospocholine (DiC$_3$PC).*

1.2.2 Lipid Bilayers

The structure of lipid bilayers *in vivo* is asymmetric. On the extracellular leaflet of a plasma membrane, many other features are present. In particular, glycolipids derived from sphingosine, which separate roughly into two types: the simple cerebroside containing either glucose or galactose, and the more complicated branched polysaccharides termed gangliosides. Such glycolipids make up the matrix of the glycocalyx surrounding many plasma membranes. Eukaryotic lipid bilayers also contain a large quantity of the steroid lipid cholesterol, which is thought to play a role in the stabilisation of lipid domains in the plasma membrane [64].

The key difference between any *in vivo* lipid bilayer and an *in vitro* lipid bilayer is the abundance of protein. Natural lipid bilayer membranes are swelled with a large quantity of protein embedded and anchored to the surface, whereas in typical *in vitro* lipid bilayer experiments, the levels of proteins used are far reduced. In addition, in lipid bilayers used

in the experiments described in this thesis hydrocarbon solvent is able to partition into the hydrophobic core inter-leaflet space. This can cause the thickness of the lipid bilayer to change, depending on the properties of the lipid tails and the hydrocarbons used as a solvent (see Section 1.6 and Subsection 2.2.1).

In vitro, a phospholipid bilayer will form as a self-assembled structure, either as a curved vesicle (liposome) or flat sheet (Figure 1.6). The driving force for this process is the exclusion of fatty-acyl chains from the aqueous solvent [260]. Typically, phospholipids will self-assemble into a lamellar bilayer mesophase at hydration levels greater than only approximately 20% [119], demonstrating the high-propensity for lamellar bilayer phase formation in solution.

The lipid bilayer exists as a liquid crystalline phase under physiological conditions. This is as opposed to an ordered gel-like phase at lower temperatures. The phase transition temperature between the two states is typically lower for unsaturated lipids versus saturated lipids (as is the case for DPhPC) [36]. Lipid molecules are free to diffuse in the plane of the lipid bilayer in the liquid crystalline state.

Descriptions of the properties of different *in vitro* artificial or synthetic lipid bilayers are now reviewed, with particular emphasis on methods used or mentioned in this thesis.

1.2.2.1 Supported Lipid Bilayers

Supported lipid bilayers (SLBs) represent one of the most widely used *in vitro* lipid bilayer technologies [38], not least due to the fact that a solid support can often render the bilayers straightforward to image. They are typically derived from either vesicle fusion to a flat surface (such as a coverslip or mica) or from a Langmuir-Blodgett film balance [225].

Vesicle-fused SLBs are usually prepared by sonication or extrusion of lipids in a buffered aqueous solution, followed by pipetting of the suspension onto a flat hydrophilic surface [167, 220]. Thereafter, vesicles have been shown to either rupture immediately upon contact with the surface, or alternatively remain intact for an extended period of time prior to rupture and deposition [225, 226]. This gradually forms a flat planar unilamellar lipid bilayer patch upon the surface. The driving force for this process is thought to be molecular crowding of intact vesicles upon the surface [225]. The exposure of a lipid bilayer patch edge upon rupture is thermodynamically unfavourable [149]. These free edges are thought to promote the rupture of other vesicles or the joining of nearby patches to create large homogeneous

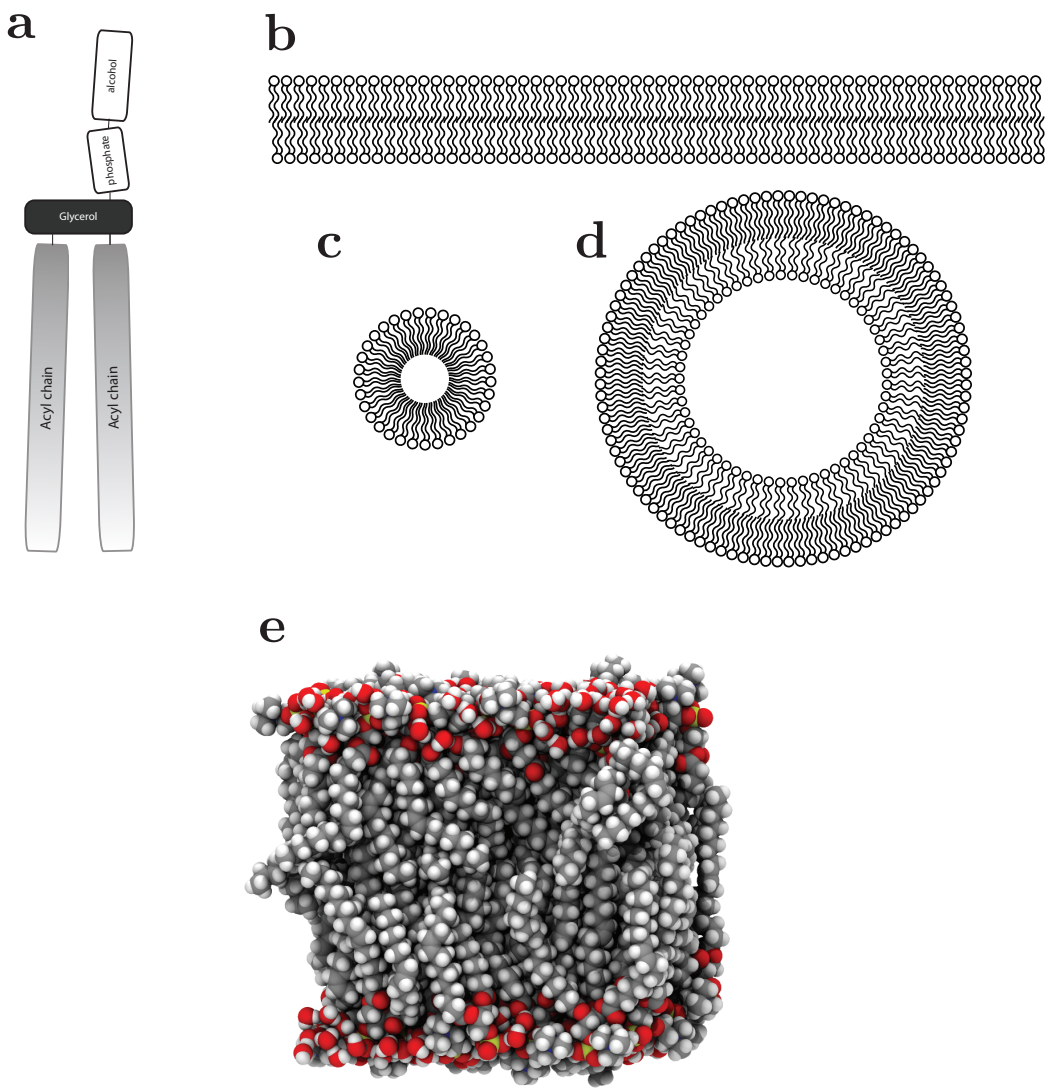

Figure 1.6: *Phosphoglycerides, their molecular architecture and structures in aqueous solution. (A) A diagram of the core components of a phosphoglyceride. (B) A schematic diagram of a unilamellar lipid bilayer (circles are the head-groups, zig-zagged lines are the two acyl chains). (C) Lipid micelles are the simplest structures that are able to form, comprising only a single leaflet of lipids. (D) A unilamellar lipid vesicle (also termed a liposome) is a spheroid lipid bilayer structure comprising two leaflets of lipids forming a bilayer. (E) An atomistic molecular dynamics simulation trajectory of a liquid crystalline state DOPC lipid bilayer following a 200 ns simulation in low hydration conditions showing interdigitating lipid bilayer leaflets. Reproduced from the results of simulations performed by the Scott Feller Laboratory at Wabash College, USA [71].*

zones of lipid bilayer. The process of SLB formation is affected by pH, temperature and the presence of divalent metal cations [225].

Defects in vesicle-fused SLBs are often reported in the literature [158, 224, 226]. If the coalescence of lipid bilayer patches is not complete, large areas of the surface may be open to the subphase. The lateral mobility of lipids in SLBs has been revealed to be considerably lower than for lipids in unsupported lipid bilayers [250]. The cause of the reduced fluidity is thought to be frictional coupling between the lipids in the lower leaflet and the substrate [158]. SLBs often form within 1-2 nm of the solid-support. This short space means it is often difficult to incorporate membrane proteins, which often have significant water-soluble globular domains protruding into the bulk water [87].

It is also possible to create SLBs on intermediate substrates between the solid support and lipid bilayer, such as gels [88, 158, 167, 237, 257–259, 295], as well as to tether a leaflet of the lipids directly onto the solid substrate [279]. This approach sometimes allows the incorporation of certain functional membrane proteins into the lipid bilayers [88, 259]. Analogous to this method of creating a wetted spacer between the solid substrate and lipid bilayer is the use of tethered lipids to facilitate the formation of lipid bilayers at a controlled distance from the solid substrate. Such tethers are usually attached to either gold or silica through thiols or silanes respectively [38]. This approach has begun to show promise for the functional incorporation of more complicated multimeric membrane protein complexes [152, 280].

The Langmuir-Blodgett film transfer technique has been used to measure phase transition temperatures of lipids, as well as to observe dynamic defect formation upon cooling of previously homogeneous lipid bilayers [258]. More recently, the same approach has been used for functional incorporation of t-SNARE complexes and to image their diffusion and interaction with lipids [281]. The approach has even shown promise in the area of asymmetric lipid bilayer creation, where the two leaflets can be created with different constituents [51, 154].

A diagrammatic summary of the different supported lipid bilayer techniques is given (Figure 1.7). All such techniques suffer from one major flaw; namely that the lipid bilayers created by these techniques contain defects and therefore are leaky to ions. Electrically, this means the lipid bilayers have poor resistivities. In the context of electrical measurements of ion channels, this means that electrical recording of single ion channel currents is impossible.

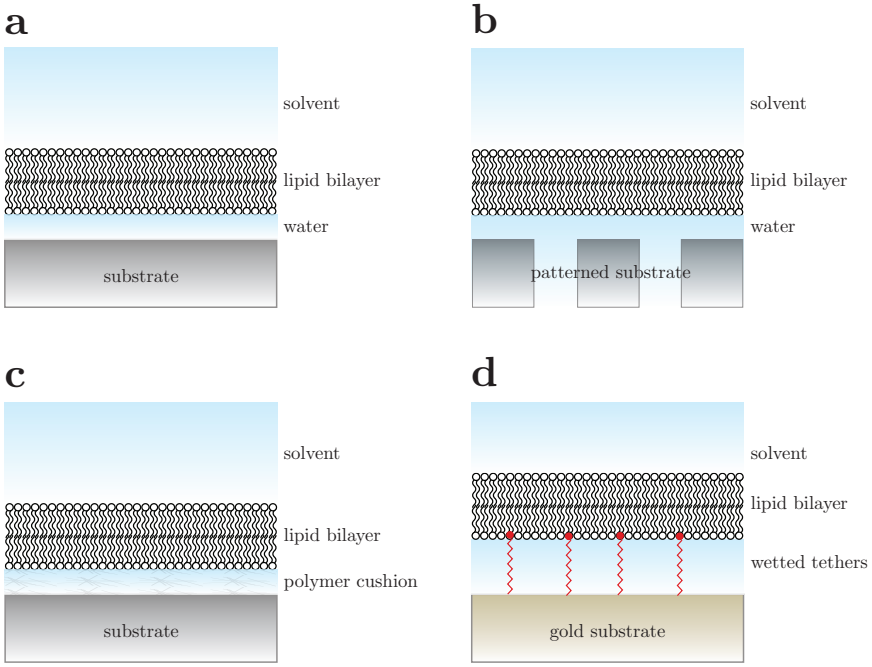

Figure 1.7: *Supported Lipid Bilayers. (A) A lipid bilayer may be created by vesicle-deposition and fusion, or using a Langmuir trough, onto a flat solid substrate. (B) A lipid bilayer may be created on a micro- or nano-patterned solid substrate. (C) A cushion of a polymer may be prepared on a flat solid substrate upon which a lipid bilayer may be created. (D) Tethered polymer chains may be attached to a reactive surface (e.g. gold) using silane or thiol chemistry, upon which a lipid bilayer may be formed on top.*

The ability to layer a lipid bilayer through tethering onto a gold or semiconducting surface is useful, as the surface can used as an electrode [259]. However, to date a gigaohm lipid bilayer seal has remained impossible to achieve with SLBs.

1.2.2.2 Langmuir-Blodgett Technique Lipid Bilayer Derivatives

Unsupported lipid bilayers derived from the Langmuir-Blodgett technique have been used since the 1970s for electrical measurements of lipid bilayers and embedded molecules [191]. Langmuir-Blodgett troughs create a monolayer of lipids at an interface between water and air. Building on this simple system, Montal and Müller adapted it for the reproducible generation of high-resistance lipid bilayers. Essentially, a small aperture in a hydrophobic film passivated with an alkane is raised and lowered between two separated Langmuir-Blodgett troughs. They termed the resulting lipid bilayer that forms between the separate water-filled chambers a black lipid membrane (BLM) [191, 193]. The fundamentals of such lipid bilayers are reviewed in a diagram (Figure 1.8).

Montal-Müller lipid bilayers are metastable. The presence of a limited hydrocarbon annulus phase results in eventual lipid bilayer failure over the course of at most a few hours. In addition, lipid bilayers formed by this technique are susceptible to mechanical vibrations, osmotic pressure and changes in hydrostatic pressure.

These lipid bilayers constitute a form of so-called unsupported lipid bilayer as both lipid leaflet head-groups face into bulk water. Their lipid phase fluidities have been characterized at the single-molecule level, revealing greatly enhanced fluidity versus solid substrate SLBs [250]. In addition, their electrical and mechanical properties allow for high-resolution ion channel electrical recording, due to high lipid bilayer resistivities [191, 269, 294]. Due to the separation of the aqueous phases on either side of the lipid bilayer, control of individual chamber buffer constituents is straightforward.

Unsupported lipid bilayers can also be formed by direct painting of lipids across an aperture in a hydrophobic septum. This method has been used to attempt to recreate unsupported lipid bilayers in platforms for microscopic visualisation [133, 203, 250].

Membrane protein complexes can be routinely reconstituted into unsupported lipid bilayers such as Montal-Müller bilayers. To date, α-helical bundle-type channels, such as ion channels, as well as porins and other β-barrel proteins have been incorporated for functional electrical assays [14, 117, 294]. Montal-Müller lipid bilayers are often thought of as the *de*

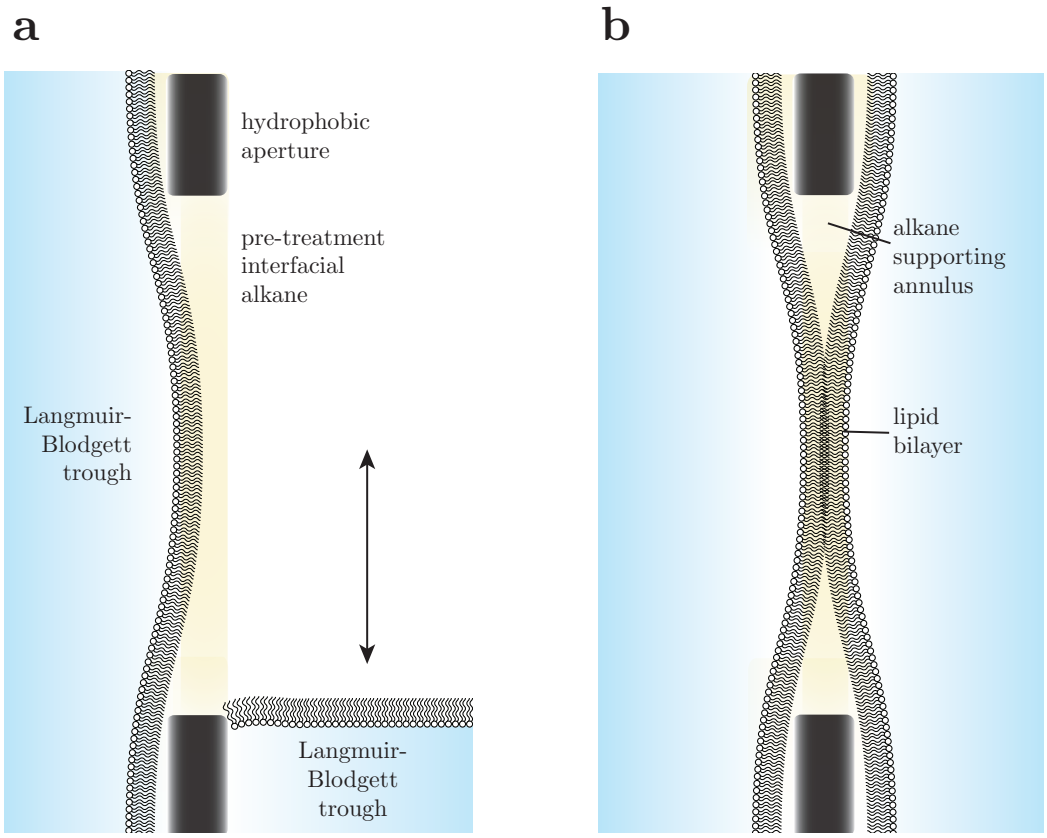

Figure 1.8: *The Montal-Müller lipid bilayer. (A) Two compartments are separated by a thin hydrophobic film (∼ 50 µm thick, n.b. aspect ratio in image not drawn to scale), typically polytetrafluoroethylene (PTFE - Teflon), with a centrally placed aperture of a diameter on the order of ∼100 µm. The aperture is pretreated by pipetting a small volume of a hydrophobic liquid, e.g. an n-alkane such as decane or hexadecane. The two separated compartments are filled with aqueous buffer, upon which a lipid solution in a volatile organic solvent (e.g. pentane) is pipetted. As the solvent evaporates the lipids will create a Langmuir monolayer at the air water interface. These monolayers can be brought into contact with the pretreated aperture in the dividing space by raising and lowering the levels of the air-lipid-water surfaces through pipetting or dipping the aperture into the troughs. (B) The resultant lipid bilayer that can form is suspended by an annulus of the pretreatment alkane. The lipid bilayer forms in the centre of the trough and consists of permeating alkane in the inter-leaflet space. The thickness of which reduces with time.*

facto standard *in vitro* planar lipid bilayer for single-channel electrical recording [14, 116–118, 228].

1.2.2.3 New Methods

Recently, a number of methods have been reported in the literature which try to marry the excellent electrical properties of Montal-Müller lipid bilayers with techniques which facilitate other biophysical measurements. For example, the goal of many groups has been to adapt high-resistance lipid bilayer membranes for imaging on microscopes [29, 132–134], as well as to automate lipid bilayer formation [131, 229]. All of such methods require complicated micro-machined apparatus, and generally show relatively poor levels of reproducibility.

Recently, emulsion based techniques have alleviated some of these difficulties mentioned, enabling high-resolution and reproducible single-channel electrical measurements. These techniques are reviewed in depth in the following chapter.

1.2.2.4 Protein Incorporation into *In Vitro* Lipid Bilayers.

A major obstacle in the use of *in vitro* lipid bilayers is the means to incorporate the protein of interest for biophysical measurements [116]. If integral membrane proteins are harvested from an overexpression system, for example *E. coli*, it is always the case that the protein of interest must be either solubilised in a detergent, or refolded using detergents. Such detergents usually interfere with lipid bilayer stability. Indeed, in order for the integral membrane protein of interest to be soluble in water, its membrane-spanning hydrophobic domains must be encapsulated in a detergent micelle. The dilemma is therefore that detergent is required for protein purification and handling, but its prescence is usually a trigger for lipid bilayer instability.

In recent years work has shown that it is possible to mechanically introduce integral membrane proteins by direct contact of a detergent-solubilised sample of protein at low concentration with a lipid bilayer [116]. This probe-based technology has also been adapted to allow for direct membrane protein transfer using a capillary. The capillary is touched to a bacterial colony expressing the integral membrane protein of interest, which is then used to penetrate the lipid bilayer, transferring the protein [117]. Other techniques have developed microfluidic pumping of high-concentration detergent-solubilised protein samples past a lipid bilayer, whereupon channel or pore insertion, the concentration of detergent can

be reduced [229].

One of the most commonly used methods for circumventing the high-concentration detergent problem is to exchange the detergent by dialysis with unilamellar lipid vesicles [108, 140]. Lipid vesicles can then fuse to the lipid bilayer and transfer the already lipid-bilayer integrated protein into the system, without having troublesome levels of detergent present.

Recently, fluorinated and hemi-fluorinated surfactants have been shown in the literature to demonstrate exceptional transfer abilities from solution to planar lipid bilayers, without greatly affecting lipid bilayer stability [32, 206, 209, 227]. This novel surfactant chemistry holds great promise for the facile reconstitution of fragile multimeric channels [118, 256].

1.3 Introduction to Single-Molecule Biological Measurements

For the majority of the 20^{th} century biochemical experiments were limited to those on ensembles of molecules. Kinetic measurements of this kind usually entail the synchronisation of a population of molecules followed by subsequent perturbation of an equilibrium, yielding an observable and measurable change. It is usually the case that the behaviour of the molecule of interest is not directly observable whilst at equilibrium. Single-molecule approaches have gone someway to alleviate this hindrance, and allow the direct observation of biomolecular behaviours and structures at equilibria, with far greater resolution than ensemble measurements [142, 222].

Single-molecule measurements are capable of measuring individual molecular dynamics, versus an averaged value in an ensemble measurement. Sub-populations of behaviours, structures and interactions are discretized and analysed statistically in single-molecule measurements, allowing insights into previously hidden '*averaged*' situations. In addition, extremely rare events can be observed which are often invisible in ensemble measurements, or were potentially classified as noise, and which could have been of great importance in a biochemical context.

Fluorescence microscopy is one such means to observe single-molecule behaviour at room temperature [297]. The technique is now well established and has produced many breakthroughs in many different areas of biology and chemistry over the past decade. Below,

a brief overview of the principles of fluorescence relative to the technique and to this work is given.

1.4 Fluorescence

The process of fluorescence occurs as a molecule in an excited state relaxes through vibrational interactions, rotation and translation in its medium followed by a spontaneous return of the excited electron back to the ground state. The prior energy loss from molecular interactions results in a shift in the emitted photon's wavelength. The process of absorption of a photon is rapid and occurs in approximately 10^{-15} s. The lifetime of the excited state thereafter is dependent on the fluorophore and its environment, but generally ranges between 10^{-10} to 10^{-7} s [163, 273].

De-excitation back to the ground state by emission of a fluorescent photon is only one of the processes which can evolve following excitation. A useful parameter to describe this is the fluorescence quantum yield (ϕ)

$$\phi = \frac{\Gamma}{\Gamma + k_{nr}} \tag{1.1}$$

where Γ is the rate constant for radiative processes and k_{nr} is the rate constant describing the non-radiative decay processes. This parameter is of particular importance in single-molecule fluorescence imaging.

The excited state of a molecule is able to undergo multiple independent de-excitation routes summarised here (Figure 1.9).

Internal conversion (IC) occurs as an excited electron relaxes through vibrational relaxation and crossing into a lower electronic state of the same spin multiplicity. This process occurs on the timescale of approximately 10^{-13} to 10^{-11} s. The spontaneous emission of a photon upon an electron dropping from the $S_1 \rightarrow S_0$ state is termed fluorescence and occurs on the order of 10^{-15} s, approximately the same rate as stimulated absorption. However, vibrational motion during this time will transfer some energy to the molecular surroundings causing a bathochromic shift (red-shift) of the emitted photon wavelength. Another major pathway of de-excitation is termed intersystem crossing (ISC). This process is a non-radiative transition from a singlet-electronic state to a triplet electronic state.

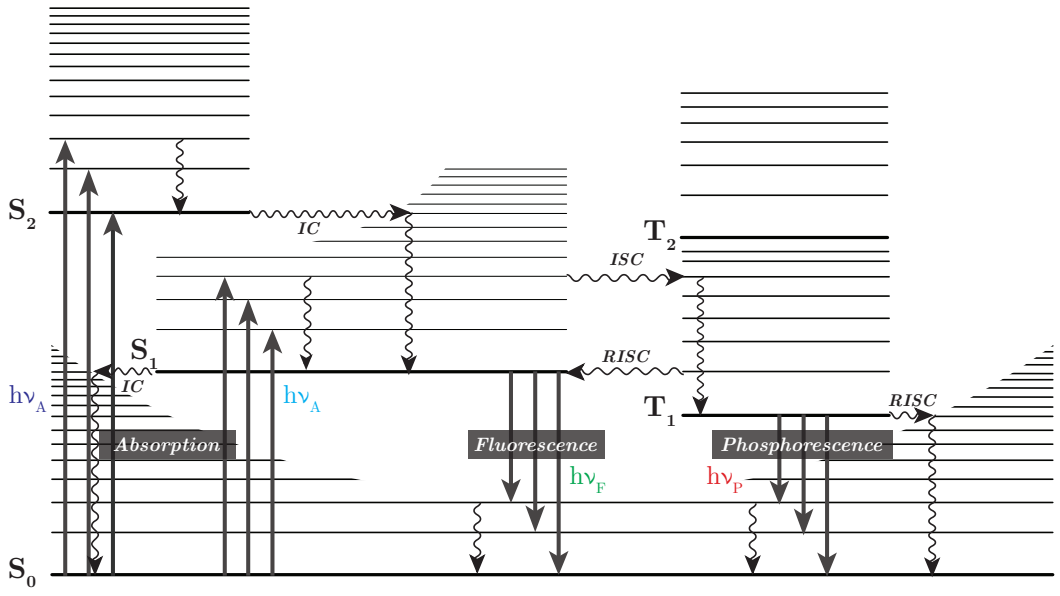

Figure 1.9: *A generalised Jablonski diagram depicting possible electronic processes undergone by an excited fluorophore. Solid lines indicate electronic transitions. Curved lines indicate vibrational transitions. IC = internal conversion, ISC = intersystem crossing, RISC = reverse intersystem crossing.S_0 is the ground singlet state, S_1 is the lowest energy excited singlet state, S_2 is a higher energy excited singlet state, T_1 is the lowest energy excited triplet state, and T_2 represents a higher energy triplet state, not ordinarily populated unless another photon is absorbed upon ISC from an excited singlet state.*

Conversion between a triplet state and singlet state is denoted here as reverse intersystem crossing (RISC). However, the causes of the two processes are identical. Upon crossing, vibrational relaxation and internal conversion will bring the molecule back to the lowest energy level. The process of intersystem crossing is in principle forbidden, however due to spin-orbit coupling (orbital magnetic moment and spin magnetic moment coupling), there is a finite probability of it occuring. This process occurs on the order of 10^{-9} to 10^{-7} s, and is therefore fast enough to compete with the singlet state de-excitation pathways. Reverse intersystem crossing may occur, enabling the delayed emission of a fluorescent photon. Alternatively radiative de-excitation from the triplet state by emission of a photon may occur, termed phosphorescence. At room temperature reverse intersystem crossing is more probable, followed by vibrational relaxation back to the S_0 state.

Of critical importance for single-molecule fluorescence studies is the phenomenon of triplet-triplet annihilation and excited-state reaction with another molecule, leading to an irreversible chemical alteration of the molecule termed photobleaching. The ground state of molecular oxygen (O_2) is a triplet state. Through direct interaction of molecular oxygen

with a fluorophore in a dark-triplet state, it may trigger de-excitation through so-called triplet-triplet annihilation. However, concomitant oxidation due to excited singlet-state molecular oxygen then reacting with the fluorophore leads to irreversible photobleaching, rendering that molecule unable to turnover fluorescently [297]. As a result, it is often the case that oxygen-scavenging molecules, for example reducing agents, are added to a specimen for observation, enhancing the fluorophore lifetime [222]. The interconversion between a fluorophore singlet-state and long-lived dark state is termed photoblinking. The affect this process has on experiments is mentioned in more detail with respect to this work throughout the thesis.

1.5 Single-Molecule Fluorescence Microscopy at Room Temperature

In fluorescence microscopy, the key factor in resolution of single-molecules is a sufficiently high signal-to-noise ratio (SNR) for a fluorophore under observation. The primary sources of noise in a typical experiment are Raman scattered photons from water molecules in the specimen, and background fluorescent species in the sample [163]. The amount of scattered light is typically minimised in single-molecule fluorescence experiments by reducing the volume of detection. By minimising the illumination volume, a dramatic reduction in the background noise is facilitated, yielding a sufficient signal-to-noise ratio for the detection of light emitted light from a single fluorophore.

The rate of photon emission from a single-molecule, which is dependent upon illumination intensity, absorption cross-section [297] and its relative quantum yield, must also be sufficiently high to register above the detector's noise threshold to give an appreciable SNR. Therefore, detector efficiency is also critical to single-molecule fluorescence detection. Recently, ultra-sensitive high acquisition rate detectors have been developed enabling resolution of single-molecules whilst they are diffusing in two and three dimensions. Whilst confocal volumes, typically analysed using avalanche photodiodes are able to be rasterised across a surface or 3D volume, for the imaging of a surface such as a lipid bilayer, it is far simpler to use a wide-field imaging technique such as total internal reflection fluorescence microscopy (TIRFm). The commonly used means to detect single-molecules using a TIRFm geometry is with a charge-coupled detector (CCD). Of interest in this work is the back-

illuminated electron-multiplying CCD, which is capable of detecting single-molecules at millisecond time resolutions.

The diffraction limit of the light microscope is given by the Rayleigh criterion thus,

$$d_R \;=\; 0.61\lambda/N.A. \tag{1.2}$$

where λ is the wavelength of the emitted photons and $N.A.$ is the numerical aperture of the microscope objective lens. This relationship describes the fundamental limit in resolution for a visible light observation in a microscope, which is approximately half that of the wavelength of the light under observation. Light from a stationary single-molecule on a surface, will be represented in an image as an Airy disk. This feature is termed the Point-Spread Function (PSF). It can be rudimentarily approximated as a 2-dimensional Gaussian-function.

Fitting the PSF in order to localize its centroid enables fluorophores to be localized at a resolution lower than the diffraction limit [202]. In recent years, this has been achieved with near nanometre precision [300]. The accuracy of all localization techniques is mainly limited by photon noise. However, detector noise and pixelation also influence the accuracy. The accuracy of a such a PSF localization has been treated theoretically previously, yielding the hypothetical resolution in one dimension $< (\Delta x)^2 >$ given by

$$< (\Delta x)^2 > \;=\; \frac{s^2}{N} + \frac{a^2/12}{N} + \frac{4\sqrt{\pi s^3 b^2}}{aN^2} \tag{1.3}$$

where s is the width of the PSF (defined as a Gaussian function), N is the number of collected photons, a is the size of the pixel in dimension x and b is the background noise.

For experiments described in this thesis, the wide-field imaging technique TIRFm is used throughout for single-molecule imaging.

1.5.1 TIRF microscopy

When a plane light wave travelling through a transparent medium of refractive index n_1 is incident upon a dielectric interface with another medium of lower refractive index n_2 at an angle θ_i greater than the critical angle θ_c (measured from the interface normal) where,

$$\theta_c \;=\; \arcsin\,\big(\frac{n_2}{n_1}\big) \tag{1.4}$$

it will undergo total internal reflection at the interface back into the first medium. If there were no transmittance into the lower refractive index medium, it is impossible to solve the boundary conditions for the electric and magnetic fields in Maxwell's equations. Hence, mathematically some of the light must propagate into the second medium, termed an evanescent wave [10, 107].

The evanescent wave penetrates only a small distance into the second medium, propagating parallel to the plane of incidence [10]. Fluorophores at or in close proximity to the interfacial region in the second medium, defined by the depth of the evanescent field, will be illuminated by the evanescent wave. However, fluorophores above the effective illuminated space ∼100 nm will not be excited. This restriction of illumination volume serves as a means to be able to identify the fluorescence from single-molecules at dilute concentrations. The background noise associated with illuminating the entire volume under study, for example by epifluorescence microscope geometries, often renders it more difficult to resolve single-molecule fluorescence.

The intensity of the evanescent wave in the z dimension $I(z)$ decays exponentially with increasing distance d from the surface thus,

$$I(z) \;=\; I_0 \exp -(z/d) \tag{1.5}$$

where I_0 is the intensity of the field at the interface. The distance the wave penetrates is given by

$$d \;=\; \frac{\lambda_0}{4\pi}\left[n_1^2 \sin^2\theta - n_2^2\right]^{1/2} \tag{1.6}$$

for $\theta_i > \theta_c$ for light of wavelength λ_0 in a vacuum. The depth of the penetration is dependent on the magnitude of the incident angle, decreasing with increasing angle of incidence. The light intensity at the interface at $z = 0$, I_o depends on the polarisation of the incident light beam and the angle of incidence. For electric field intensities $\mathscr{F}$ incident upon the interface for s-polarised light (parallel to the plane of incidence, $\|$) and p-polarised light (perpendicular to the plane of incidence, $\perp$), the intensities of the evanescent waves for $I_0^{\|}$, and $I_0^{\perp}$ are given by:

$$I_0^{\|} \;=\; \mathscr{F}^{\|} \cdot \frac{4\cos^2\ \theta(2\sin^2\theta - n^2)}{n^4\cos^2\theta + \sin^2\theta - n^2} \tag{1.7}$$

and

$$I_0^{\perp} = \mathscr{F}^{\perp} \cdot \frac{4\cos^2\theta}{1-n^2} \tag{1.8}$$

where the refractive index ratio $n_2/n_1 < 1$. I_0 is also proportional to the square of the amplitude of the evanescent wave electric field $\mathbf{E}$ at $z = 0$.

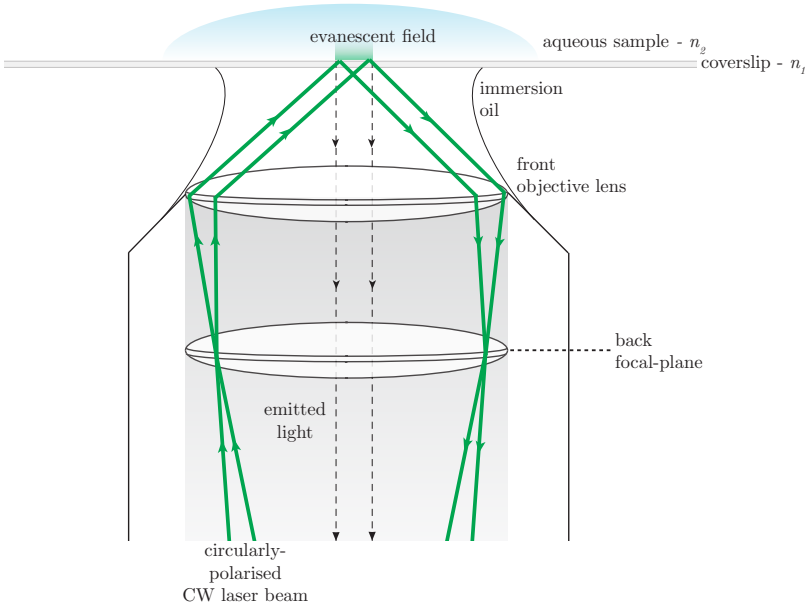

Figure 1.10: *Objective-type TIRF microscopy. A Gaussian-shaped collimated cw laser beam is focussed at the back aperture of an objective lens. The beam propagates through the objective lens incident upon an interface between a higher refractive index medium and a lower refractive index medium at an angle greater than the critical angle, according to Snell's law. The light is totally internally reflected at this interface, where it returns through the objective lens. At the interface an evanescent wave is generated which propagates in parallel with the plane of incidence and penetrates to a depth of approximately ∼100 nm. Fluorophores at the interface are illuminated, and their emitted fluorescent photons are collected through the same objective lens for imaging. In circumstances described in this thesis, this is achieved using a dichroic lens before the objective in the optical path, the emitted light is then imaged onto a detector for data capture.*

In reality, a Gaussian-shaped laser-beam is used for excitation of single-molecules in TIRF microscopy [34, 264]. The degree of penetration of the evanescent wave does not differ from Equation 1.6.

There are two means to perform TIRFm: objective-type TIRF microscopy requires a high N.A. objective lens to illuminate the sample, which is also used to collect emitted photons for imaging. Alternatively, a prism may be used to illuminate the sample, whilst detecting the emitted light through a separate objective lens. Prism-TIRFm facilitates a slight enhancement in SNR, but is cumbersome to use for biological measurements as it is difficult to implement into a standard inverted microscope. Objective TIRF, with lenses of

N.A. = 1.4 or higher were used in this work, which are capable of totally internally reflecting a laser beam at a standard coverslip surface. This scheme of imaging is illustrated (Figure 1.10).

1.5.1.1 Cyanine Dye Photophysics

Cyanine is a name attributed to dye molecules derived from a polymethine manifold, *i.e.* a polymer of an odd number of methine (C-H) groups. Of interest in this thesis is the chemistry of the closed-chain cyanines with the general formula Aryl=N^+=CH[CH=CH]$_n$–N=Aryl (Figure 1.11A) [195].

Different substitutions are often made at the 5 and 5' positions of the indole rings, affecting the photophysical properties of the dye, in general leaving the spectral shape unaltered but shifting the maxima [194]. Subtituents affect the excited singlet-state lifetime (τ_s) and the quantum yield (Φ). Singlet state lifetime is principally affected by the rotational rate constant about the carbon-carbon double bonds in the link between the heterocycles, dependent upon steric effects of the substituents. In this thesis, the indole-substituents at the 5 and 5' positions are sulphone (SO_3), which enhances solubility in water. This substituent is also electron withdrawing in character, which therefore slightly alters the carbon-carbon double bond character in the centre of the molecule, partially hindering the isomerisation of the chromophore. A diagram illustrating the various resonance forms and rotational isomers is shown (Figure 1.11C).

The ability to isomerise in aqueous solution is the principle de-excitation pathway in cyanine dyes, such as the Cy3 illustrated here (Figure 1.11C) [194, 231]. The isomerisation of the excited fluorophore from all-*trans* to mono-*cis* leads to the establishment of much greater rotational freedom of the two heterocyclic termini of the molecule. This establishes what is termed a twisted intramolecular charge transfer state (TICT) [273], resulting in an alteration of the potential energy surface of the molecule. Many more internal rotational energy levels exist in both the ground and excited states in this conformation, and hence a greater degree of overlap between the ground and excited states increases the probability of non-radiative internal conversion back to the ground state. A summary of the main photophysical processes occuring upon excitation of the molecule for a generalised cyanine is shown(Figure 1.12). At the single-molecule level, the high-propensity for photoblinking of Cy3 and other cyanines is attributed to long-lived *cis*-isomers of the chromophores, twisting

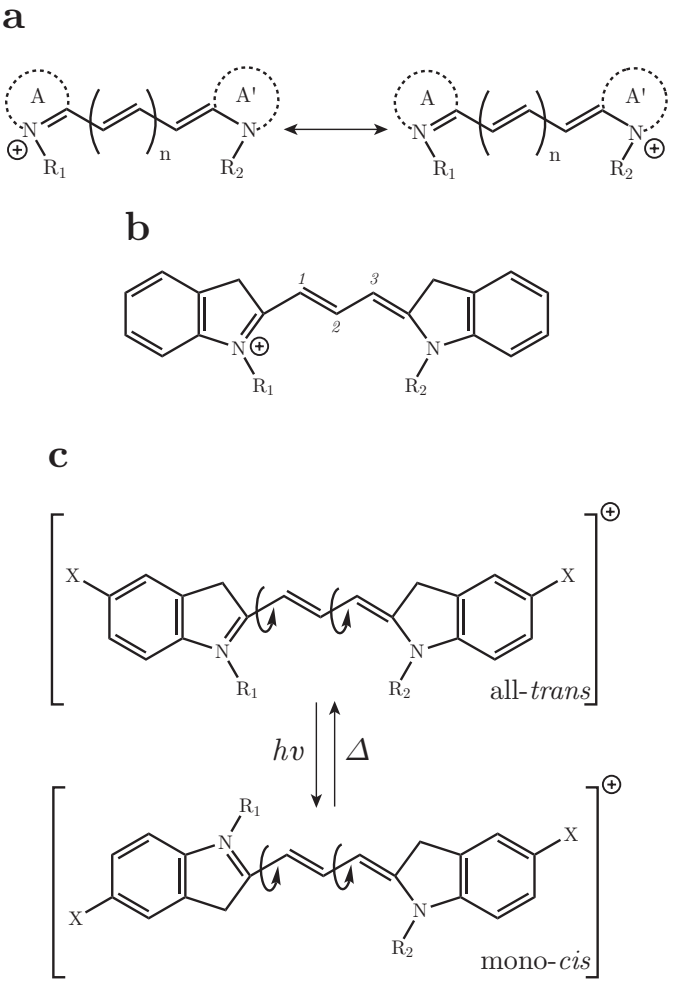

Figure 1.11: *(A) Generalised structure of closed-chain cyanines. In Cy3 dyes used in this work, the heteroaromatic base substituent is an indole derivative where X= SO_3 in this work. Nomenclature derives from the number of methine groups appending the two heteroaromatic base substituents together, i.e. Cy3 = 3. [65]. The dyes have delocalized positive charge, illustrated as two resonance forms. (B) The base structure of Cy3 dyes. Numbers indicate the non-standard numbering of the methine substituent groups as first used by Ernst et al. [65]. (C) Rotation about the central carbon-carbon single bonds gives cis-Cy3. This process accounts for ∼90% of excited state relaxations at room temperature [194, 231].*

the molecule from planarity and therefore decoupling the conjugated state, inhibiting spontaneous absorption of a photon.

1.5.1.2 Cation-Chelating Fluorophores

Fluorescence can be enhanced in certain fluorophores through interaction with a metal cation. One particular mode of enhancement is termed photoinduced charge transfer (PCT). If a fluorophore comprises an electron-donating group covalently attached to an electron-withdrawing group, upon excitation with a photon, the charge distribution in the molecule

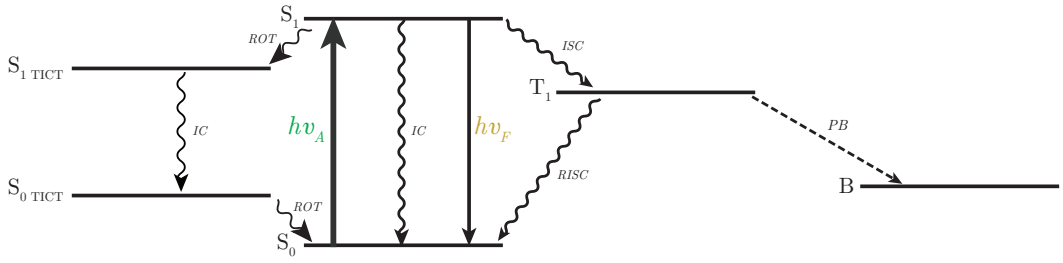

Figure 1.12: *Cyanine photophysical states. Upon absorption of a photon a cyanine molecule may rotate around one of its central bonds creating the cis isomer. This results in the creation of a TICT state (ROT). A higher degree of rotational motion here creates a large probability internal conversion and vibrational relaxation back to the ground state, whereafter rotation may occur to bring the molecule back to the trans conformation. If a photon is absorbed and intersystem crossing ensues, it may be the case that it is either quenched by triplet-triplet annihilation with ground-state molecular oxygen, or that this process triggers subsequent photobleaching (PB) by the reaction with the excited singlet-state oxygen molecule. Regular fluorescence and RISC may also occur.*

will be greatly affected. This results in a large instantaneous change in the dipole moment of the molecule. In the presence of a cationic species, such as for example calcium ions, the efficiency of such charge transfer upon excitation is altered. The strength of the interaction with either the electron-donating or -withdrawing groups as a result affects the fluorescence quantum yield [273].

The chemical structure of the calcium-indicator probe Fluo-4 is shown [82], illustrating the xanthene and BAPTA moieties and their conjugation (Figure 1.13).

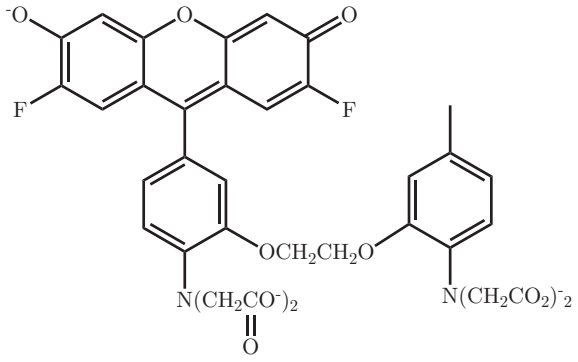

Figure 1.13: *The chemical structure of the calcium-indicator probe Fluo-4, showing the planar xanthene with a centrally-appended BAPTA moiety.*

In the case of the calcium-chelating fluorophores described in this thesis based upon xanthenes, the absorbance and emission maxima remain largely unaffected by the presence of a chelated metal cation. If the 1,2–bis(O–aminophenoxy)ethane–N,N,N',N'–tetraacetic acid (BAPTA) moiety is free to rotate because of lack of calcium, the excited state is postulated to involve a resonance form driving electron density to the xanthene moiety, causing steric

demand of co-planarity between the BAPTA and xanthene, thereby enhancing non-radiative decay probability [186]. The calcium binding to the BAPTA amino nitrogen (an electron-donating group) is expected to withhold electron density from the conjugated xanthene, increasing the quantum efficiency, and hence brightness of the dye. This straightforward chemical principle enables brightness enhancements from pure form to calcium-chelating form on the order of 40-fold.

1.5.2 Single-Particle Tracking

The point spread functions of single-molecules in TIRFm images described in this thesis are generally sufficiently resolved to enable tracking during two-dimensional diffusion at the lipid bilayer. Linking particles between one frame and the next, so-called single-particle tracking (SPT), has been used successfully to study diffusion of various different biomolecules *in vitro* and *in vivo*. Single-particle tracking (SPT) is a powerful technique for measuring dynamics and heterogeneity in biological systems [233]. In particular, the ability to observe single fluorescently-labeled molecules diffusing in and upon lipid bilayers has greatly improved our understanding of membrane biology [160, 169, 214].

The underlying basics of the technique involve two main processes [39]. The first is the definition of PSFs in a stack of images through a detection algorithm and fitting their location. The following step takes the PSF position information in all frames and derives trajectories for all PSFs in time. The means to do this are varied, however the majority of algorithms take the minimum displacement PSF in the $n^{th} + 1$ image as the link to the next frame.

In order to fit the location of a fluorophore, direct fitting through localization with centre-of-mass [86], centroid [234], Gaussian [238] or direct PSF maximum likelihood fitting [202] is often performed. Alternatively, image cross-correlation may be performed to determine a fluorophore locale by direct comparison of subsequent frames [84, 160]. The discrimination of detected PSFs in an image is usually performed post-trajectory calculation, and involves mathematical appreciation of the expected PSF functions in the linked trajectories [53].

1.6 Single-Channel Electrical Recording

To a good approximation the lipid bilayer acts as a capacitor, where for a lipid bilayer the relationship between capacitance and voltage [269] is given by

$$\Delta C \;=\; \alpha C_0 (V_{app} + \Delta\psi)^2 \tag{1.9}$$

where C_0 is the minimum bilayer capacitance for no potential difference, ΔC is the change in capacitance, V_{app} is the externally applied voltage, α is the membrane elasticity and $\Delta\psi$ represents the difference between the boundary potentials due to surface charge and dipoles at either side of the lipid bilayer's interface with bulk water [236].

In practice, by measuring the current response to an applied triangular waveform potential, it is straightforward to calculate the capacitance of the lipid bilayer during experimentation as

$$I \;=\; C\frac{dV}{dt} \tag{1.10}$$

where I is measured current and t is time. This process is simplified by measuring the magnitude of the square-wave response of a 100 pF capacitor (acting as an electrical calibration artificial lipid bilayer), to then evaluate the capacitance of the real lipid bilayer by comparison with its response.

The capacitance of the bilayer is primarily dependent on two parameters. Firstly, the thickness of the lipid bilayer, which is affected by the amount of partitioning solvent in the inter-leaflet space. Secondly, it is affected by the total area of the lipid bilayer [4, 189]. Lipid bilayer capacitances are often reported in terms of their specific capacitance per unit area, for example a typical lipid bilayer in a patch-clamp experiment would have a specific capacitance of 1 μF cm^{-2} (n.b. this value is larger than a pure lipid bilayer, free from protein, due to the large degree of protein embedded within it). Capacitance measurements are used as a means to quantify the size and thickness of a bilayer, and to monitor its stability during experiments.

1.6.1 Stochastic Sensing

Nanopore stochastic sensing is the process of observation of ion current through a single protein pore as it is stochastically transiently blocked by molecules in solution. The lengths

of blocks (τ_{off}) and residual ion currents upon blocking are analysed statistically to yield rate constants for the blocks and average residual current values. This enables the specific identification of the blocking molecules and in some cases their orientation, redox states and isomers [14, 31, 96, 171, 172, 243]. A diagram showing a hypothetical stochastic sensing experimental electrical recording is shown (Figure 1.14).

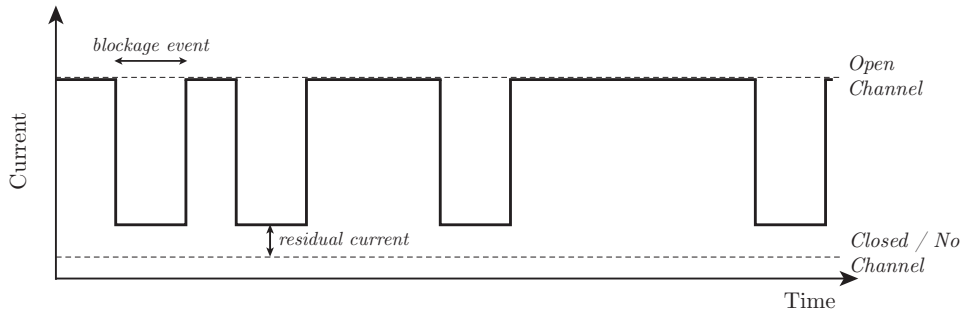

Figure 1.14: *The principles of stochastic sensing with a nanopore. The blocking at positive potential is manifested as a stepwise reduction in ion current. The lengths of such blocks are recorded along with the inter-block openings, and the residual ion current amplitudes for the blockage events. The statistical analysis of such blocks enables the identification of the blocking molecules.*

Chapter 2

Droplet-on-Hydrogel Bilayers

Abstract

The development of Droplet-on-Hydrogel Lipid Bilayers (DHBs) is described. Their use as a model synthetic *in vitro* lipid bilayer for the study of membrane protein's electrical activity is demonstrated. In order to detect the membrane channels present in cell extracts, DHBs are scanned across SDS-PAGE gels following electrophoretic separation of membrane channels. DHBs are also employed as a system for stochastic sensing using α-hemolysin.

2.1 Droplet Bilayers Introduction

2.1.1 Historical Background

2.1.2 The Droplet-on-Hydrogel Bilayer

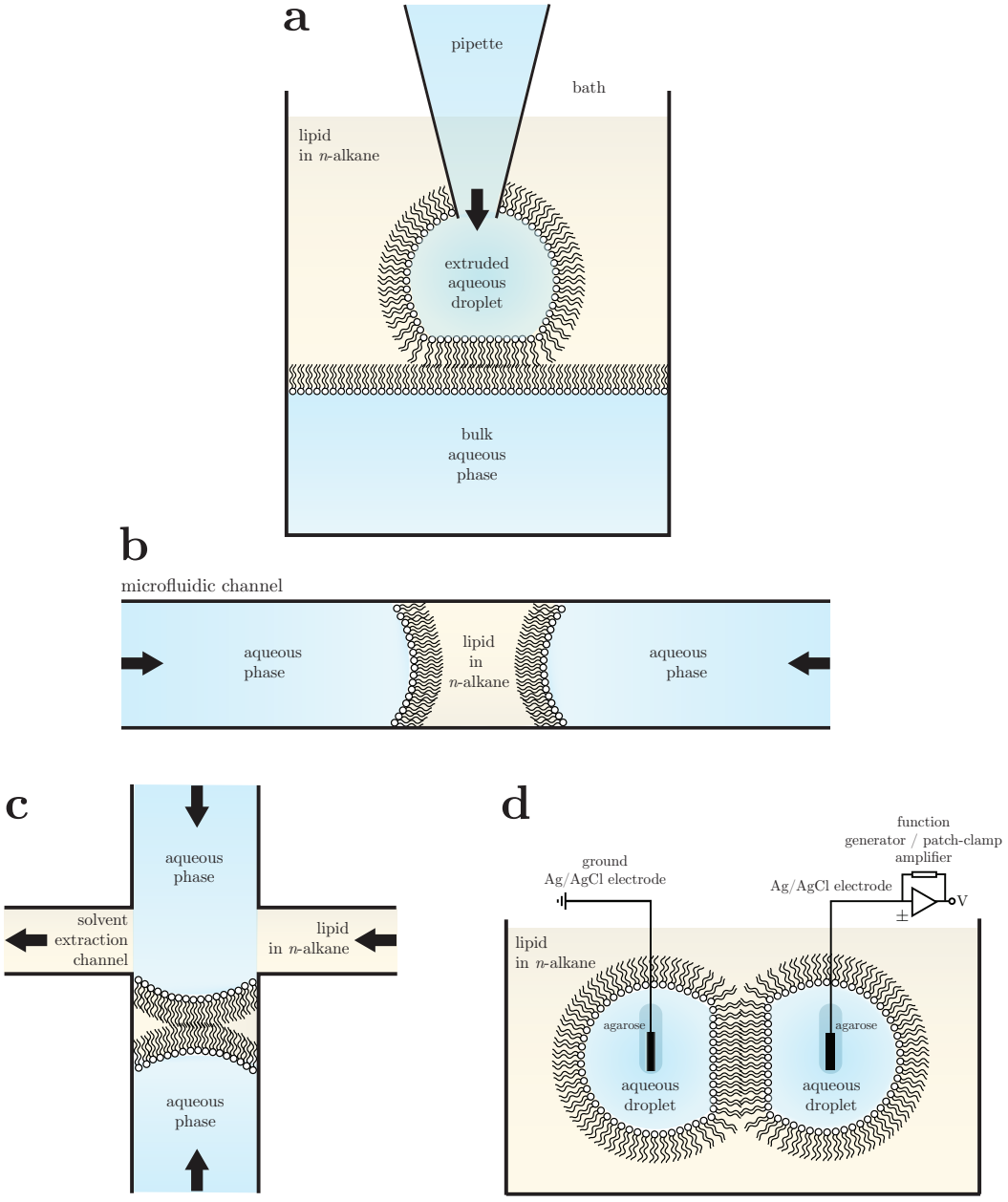

Figure 2.1: *(A) A diagram showing the general principle outlined by Tsofina et al. in their original paper in Nature in 1966 [270]. A pipette blows out a small volume of water into a bath which contains a bulk water volume supporting a hydrocarbon phase above it containing lipids. (B) An outline of the microfluidic principle devised by Malmstadt et al. at UCLA [178]. Here, two aqueous volumes are pumped in a channel towards one another in a channel filled with a hydrocarbon phase with lipids dissolved in it. (C) A demonstration of how the bulk hydrocarbon phase can be extracted in a microfluidic device, devised by Funakoshi et al. in Tokyo [75]. (D) The Holden approach to Droplet Interface Bilayer formation [118]. Two aqueous droplets are submerged under a solution of lipid in an n-alkane. When the two droplets are brought into contact through micromanipulation with agarose anchored electrodes, they spontaneously form a lipid bilayer at the contact interface.*

2.1.3 Physical Characteristics of DHBs

2.1.3.1 Lipid Bilayer Longevity

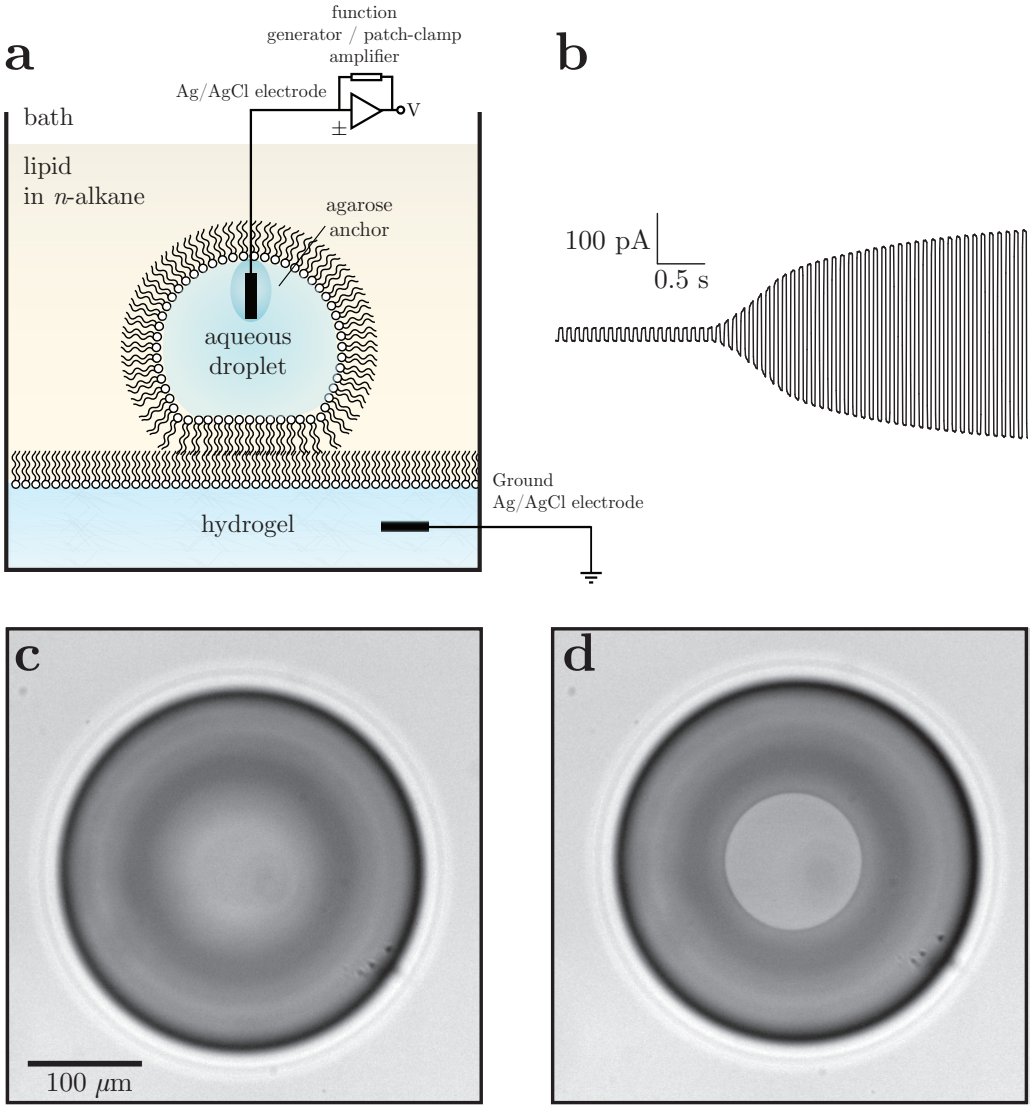

Figure 2.2: *(A) A diagram illustrating the principles of DHB formation. An aqueous droplet (approximately 100 nL in volume) is pipetted onto a hydrogel submerged underneath a volume of lipid dissolved in an n-alkane. Upon contact of the two aqueous volumes, a lipid bilayer will spontaneously form at the interface. It can then be electrically probed using a micromanipulated thin Ag/AgCl electrode with a corresponding ground electrode present in the hydrogel substrate. (B) Capacitance of the lipid bilayer is monitored through the application of a triangular sweep alternating potential and measuring the peak-to-peak current response with a patch clamp amplifier. Amplifier circuitry is described in the appendix [189]. (C) A 10 × magnified image of a droplet contacting a substrate hydrogel prior to bilayer formation, (D) and after lipid bilayer formation.*

2.1.3.2 Interfacial Chemistry in DHBs

2.2 Results

2.2.1 Lipid Bilayer Capacitance

2.2.2 DHB Manipulation

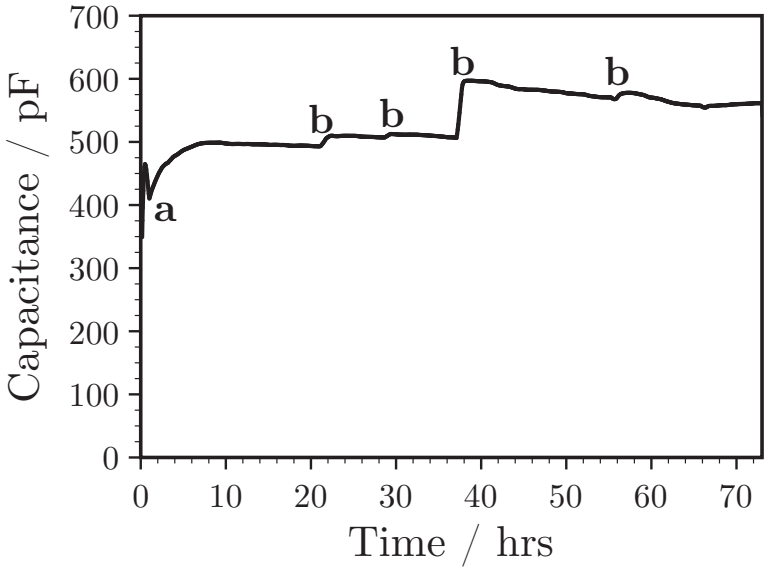

Figure 2.3: *A 72 hr test of DHB stability under operating conditions. A single 100 nL droplet was probed with a 100 μm thick Ag/AgCl electrode for electrical measurements, with a similar ground electrode present in the gel. Using a function generator and patch-clamp amplifier, a triangular sweep alternating potential (2.5 Hz, ±100 mV) was applied to the droplet to measure the current response for capacitance derivation. After the initial formation of the bilayer it expanded rapidly, yielding a rapid rise in capacitance to ∼500 pF as indicated. Immediately after this the bilayer was translated across the gel for imaging through the use of the anchored electrode inserted in the droplet. The bilayer size was slightly reduced to start the experiment (a), as the droplet and its bilayer relaxed on the electrode, the size of the bilayer increases with time yielding an increase in capacitance. At positions marked (b), the bilayer was manually adjusted to assist in imaging. After 72 hr the experiment was manually terminated with the DHB remaining intact.*

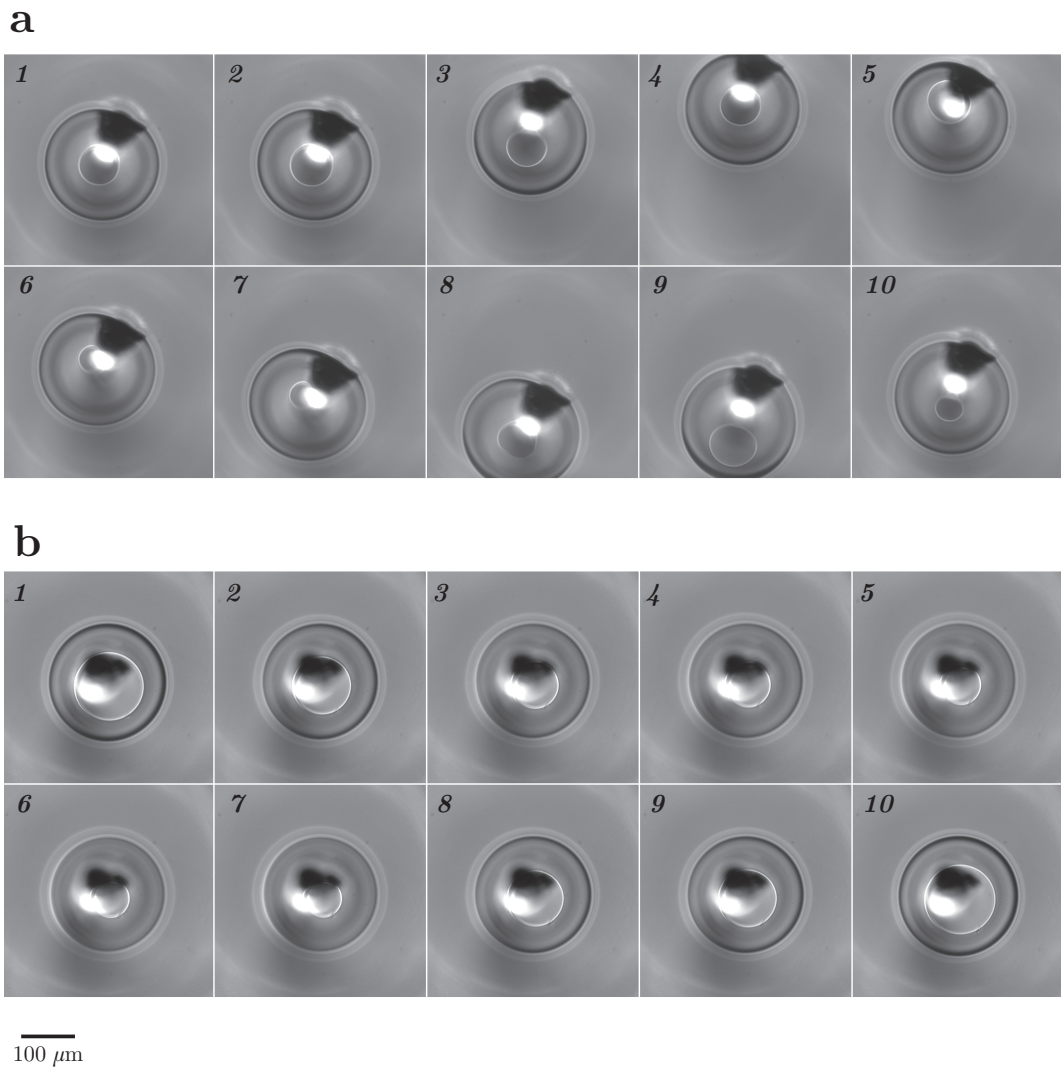

Figure 2.4: *A series of images demonstrating rapid DHB translation across a surface and dynamic lipid bilayer area alteration upon a 2% agarose gel buffered with PBS. Each frame is separated by 2 s. The scale is the same for all images as indicated at the bottom left. (A) Lipid bilayer translation. (B) Lipid bilayer size control.*

2.2.3 SDS Electrophoresis of Membrane Channel Proteins

2.2.4 α-Hemolysin Gel Scanning

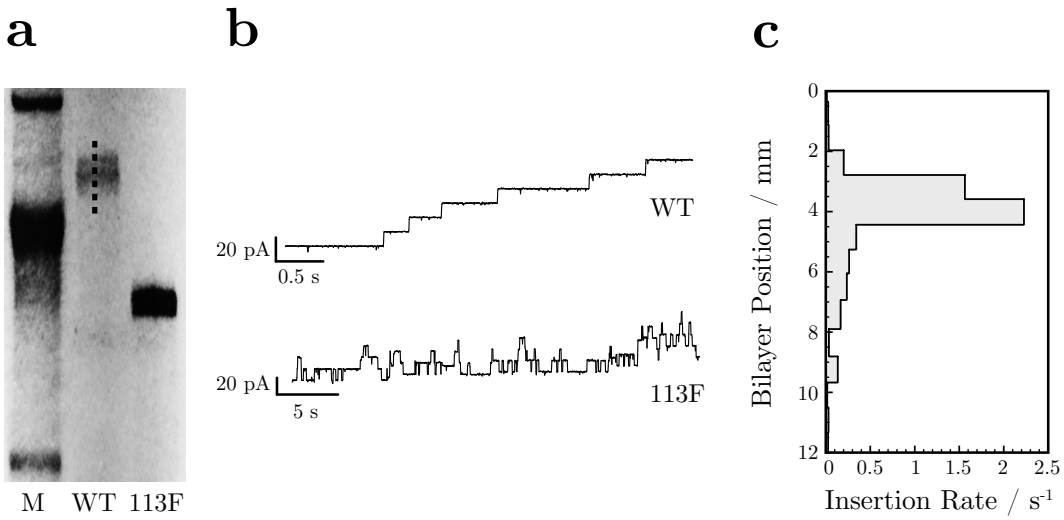

Figure 2.5: *Scanning DHBs across an SDS-PAGE gel following electrophoresis. (A) A composite image of a dried gel (with prestained marker band (M), with overlaid autoradiogram denoting the positions of two α-hemolysin variants, (WT) α-hemolysin wild-type and (113F) α-hemolysin M113F-D8. Marker bands correspond to approximate molecular weights of 210, 111 and 71 kDa. After gel dialysis in electrolyte solution (10 mM Na_iPO_4, pH 7.0, 1 M KCl) and immersion in DPhPC/C_{16} solution, the gels were scanned with 200 nL droplets containing the same buffer plus 10 μM β-cyclodextrin (βCD). (B) Protein insertion and blocking was observed by application of a voltage-clamp (+10 mV) and monitoring the ionic current across the bilayer using a patch-clamp amplifier. M113F α-hemolysin displays characteristic long-lived blocks by βCD enabling its identification versus WT α-hemolysin. (C) Protein insertion was localized around the bands illustrated in the gel. WT α-hemolysin was scanned across a 12 mm region indicated by the dotted line across the band in the gel image (A) from the top to the bottom. Protein insertion rate across this scanned region is plotted as a function of distance from the top of the dotted line indicated on the gel image.*

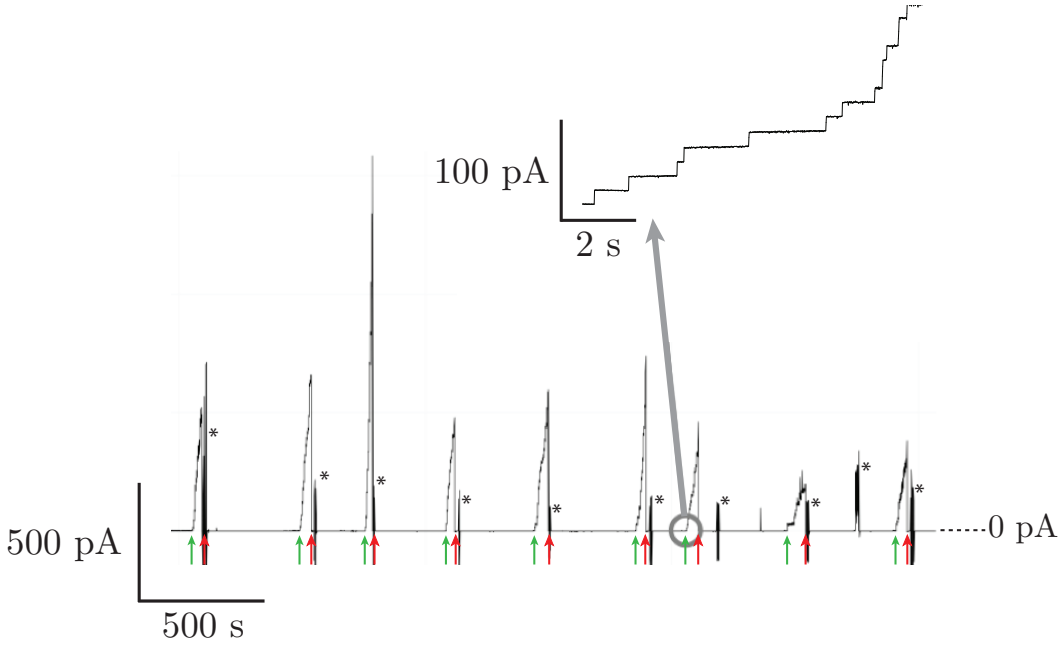

Figure 2.6: *An example of the rapid reformation of DHBs on a polyacrylamide gel with doped IVTT purified protein. DHBs are formed (green arrows)and removed in rapid succession over a period of minutes illustrating the stability of the droplets. Also, as the DHB is removed from the surface (red arrows), the proteins embedded in the bilayer are removed or denatured and are not present upon re-establishment of the bilayer. Asterisks mark manual manipulation of the droplet, causing electrical noise.*

2.2.5 Detection of Low Concentration Membrane Channels in Gels

2.2.6 Stochastic Sensing and Analyte Detection with DHBs

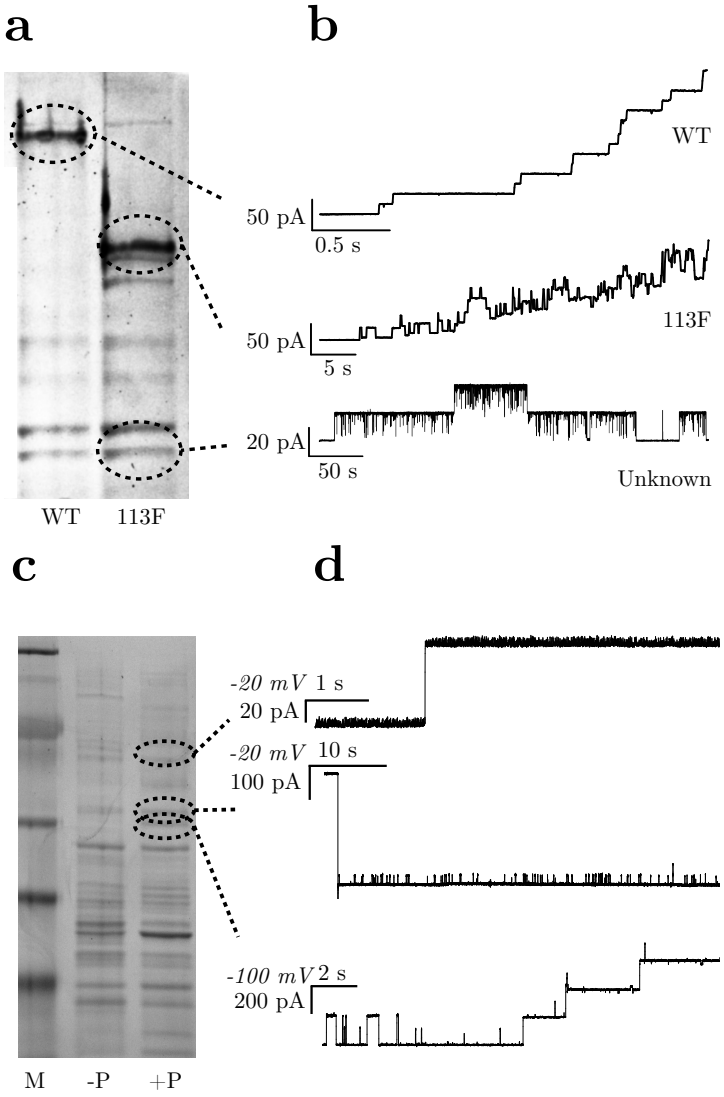

Figure 2.7: *Scanning E. coli extracts in gels using DHBs. (A) A Coomassie-stained gel after DHB scanning, showing SDS-PAGE separated E. coli cell extracts from JM109(DE3) E. coli. The E. coli transformants harbour plasmids coding separately for αHL-WT and αHL-M113F-D8. No overexpression was performed, instead the protein is produced through leaky expression. After gel dialysis in electrolyte solution (10 mM Na_iPO_4, pH 7.0, 1 M KCl) and immersion in $DPhPC/C_{16}$ solution, the gels were scanned with 200 nL droplets containing the same buffer with 10 μM βCD. Protein insertion, blocking and gating was observed by application of a various clamped voltages and monitoring the ionic current across the bilayer using a patch-clamp amplifier. (B) At the top the clear presence of αHL-WT is observed. In the centre αHL-M113F-D8 is observed. At the bottom small numbers of porin-like channels were found in the lower region of the gel. (C) A Coomassie-stained gel after DHB scanning, showing SDS-PAGE separated E. coli cell extracts from JM109(DE3) E. coli and PC2889(DE3) E. coli. (D) Various unidentified channels can be found in the JM109(DE3) (+P) lane, but not in the porin-free PC2889(DE3) lane (−P), (genotype = ΔLamB -ompR). The figure shows some example traces acquired at −20 mV (top two) and −100 mV (bottom).*

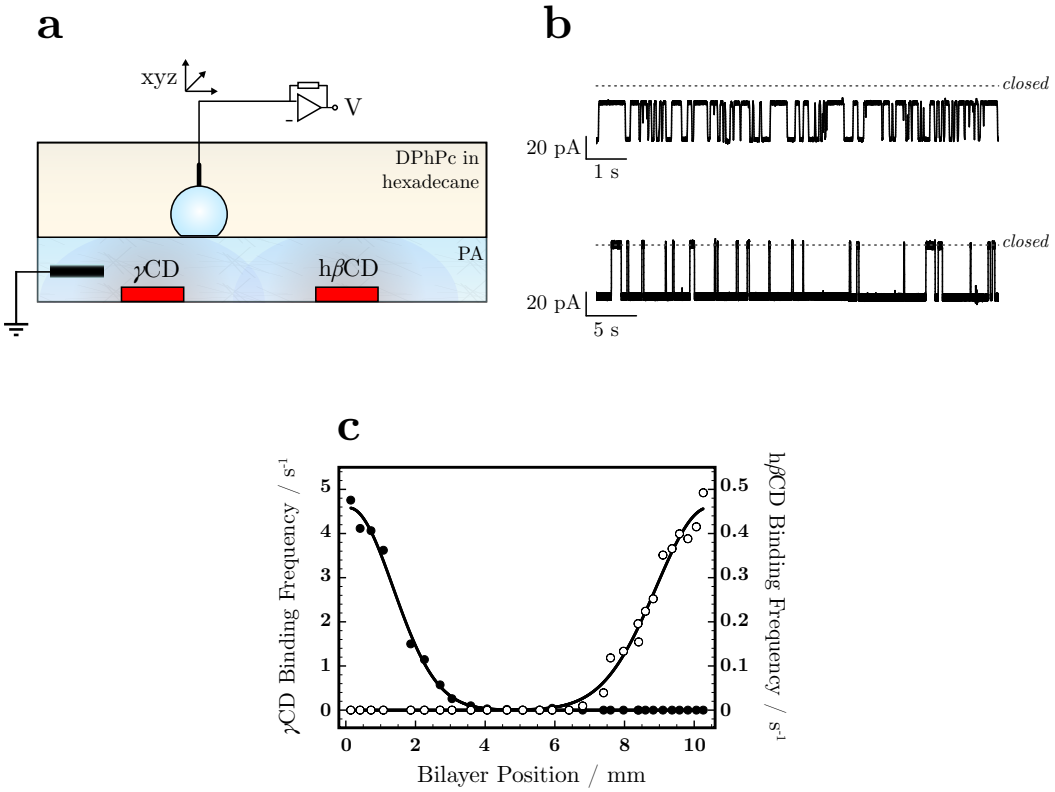

Figure 2.8: *Stochastic sensing of cyclodextrins using α-hemolysin embedded in DHBs. (A) A schematic diagram of the experiment employed to scan for gel-embedded analytes in a polyacrylamide (PA) gel. γ-Cyclodextrin (γCD) and heptakis(2,3,6-tri-O-methyl)-β-cyclodextrin (hβCD) were doped at the underside of the polyacrylamide gel 10 mm apart. After gel immersion and stabilisation in the DPhPC/C_{16} solution, the gel was scanned with droplets containing αHL-WT pores. Under a voltage-clamp the ionic current was measured using a patch-clamp amplifier whilst monitoring the bilayer position on a microscope. (B) The binding characteristics of γCD (top, 68% block) and hβCD (bottom, 95% block) to αHL-WT are clearly distinguishable in electrical recordings (−50 mV, 1 M KCl, 10 mM Na_iPO_4, pH 7.0). (C) A plot of the binding frequency of γCD (solid circles) and hβCD (hollow circles) as a function of distance in a linear scan between the two doping locations. The lines indicate Gaussian fits to the measured binding frequencies.*

2.2.7 Electrical Recording of Other Membrane Channels

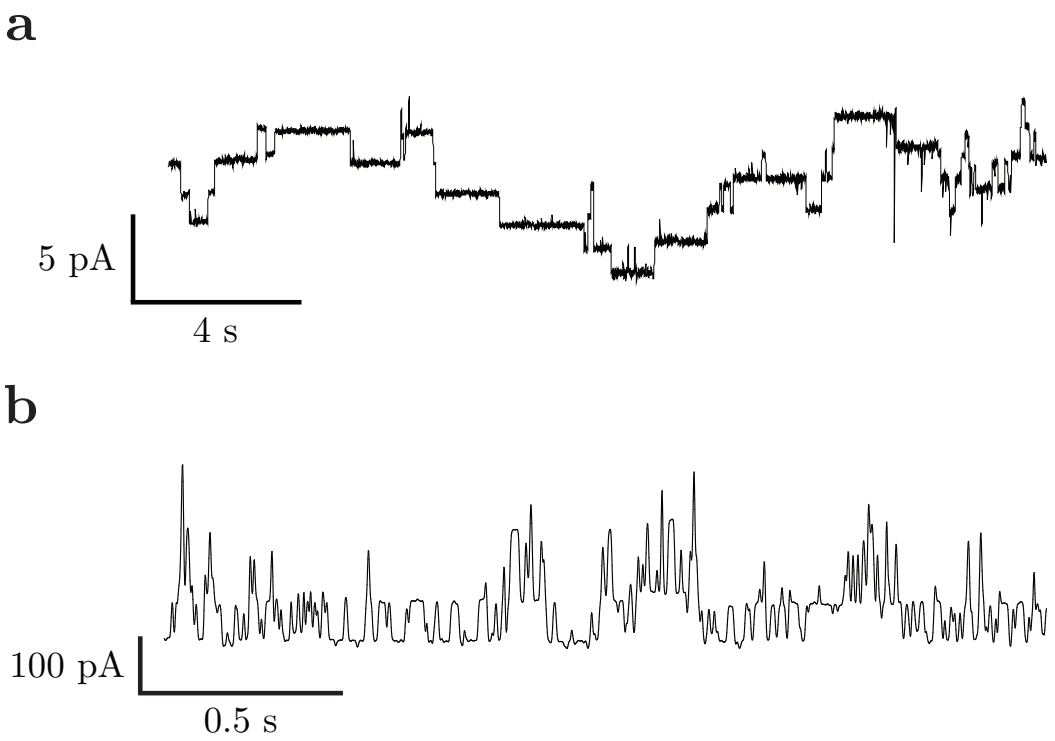

Figure 2.9: *Electrical traces showing characteristic behaviour for gramicidin and alamethicin channels in DHBs. (A) The trace shows an example of Gramicidin D (Sigma-Aldrich) channels in a DHB (−100 mV, 10 mM Na_iPO_4 buffer, pH 7.0, 1 M KCl) formed on a 2% agarose gel (10 mM Na_iPO_4 buffer, pH 7.0, 1 M KCl). The channels were introduced to the bilayer from the droplet side by means of vesicle fusion from gramicidin-containing DOPC vesicles (0.1 mg mL^{-1} 1,2-dioleoyl-sn-glycero-3-phosphocholine, 5 μg mL^{-1}). The characteristic transient appearance and disappearance of channels is manifested as a step-wise increase and decrease in membrane conductance. (B) The trace shows an example of alamethicin (Sigma-Aldrich) channels in a DHB (+100 mV, 1 M KCl in water) formed on a 2% agarose gel (1 M KCl in water). The alamethicin was incorporated into the droplet in solution at a concentration of 500 nM from a methanol stock. The characteristic transient appearance and disappearance of channels is manifested as a step-wise increase and decrease in membrane conductance.*

2.3 Discussion

2.4 Conclusions

2.5 Materials and Methods

2.5.1 General Methods

2.5.2 *In vitro* Transcription and Translation of Proteins

2.5.3 Electrophoresis of IVTT Proteins

2.5.4 Extraction and Electrophoresis of Crude Membrane Preparations from *E. coli*

2.5.5 Porin-expressing and Porin-free *E. coli* Gel Scanning

2.5.6 DHB Gel Scanning

2.5.7 Electrical Measurements and DHB Imaging

Chapter 3

Engineering α-Hemolysin for Single-Molecule Fluorescence Imaging

Abstract

This chapter describes the design, production and characterization of a singly-labelled α-hemolysin monomer and multiply-labelled α-hemolysin heptamer with the rigidified cyanine dye Cy3B. The α-hemolysin labelling product is characterized in bulk to verify the desired 1:1 labelling stoichiometry. The labelled protein described in this chapter is used in subsequent single-molecule fluorescence studies of α-hemolysin assembly.

3.1 Introduction

The obvious requirement for any fluorescence experiment is the presence of a fluorophore. Selecting the most appropriate fluorophores for biological experiments is almost always one of the most critical decisions to be made. In recent years the arsenal of available fluorescent molecules has increased dramatically [62]. However, of note is the fact that the number of available of fluorescent small organic molecules has not been expanded greatly.

For single-molecule fluorescence experiments it is important to select a fluorophore based

upon the following criteria, in no particular order of preference:

1. Brightness. A large absorption cross section and high quantum yield is required, as signal-to-noise is key to single-molecule observation.

2. The means to incorporate the fluorophore into the experiment, *i.e.* conjugation chemistry.

3. The projected expected relative risk of perturbation of the process under observation upon modification of a biomolecule with a fluorophore.

4. Fluorescence emission spectral characteristics.

5. Photophysical characteristics, such as propensity for photoblinking and relative photostability.

The criteria enumerated above are all relatively easily overcome with available dyes today, however the photoblinking and photobleaching characteristics of dyes remains a great problem [147]. The risk of perturbation of the α-hemolysin heptameric complex is the principal concern in the appending of an extrinsic fluorophore to the protein. Fortunately, the presence of high-resolution X-ray crystal structures [204, 249] enables rational decisions to be made about the placement of the dye. In addition, α-hemolysin has been extensively functionally studied by traditional molecular biological techniques. This has yielded a wealth of details surrounding the behaviour of separate domains and single amino acids in the processes of oligomerization and pore formation, enabling a highly rational and targeted approach to protein labelling.

3.1.1 Experimental Design and Theoretical Considerations

3.1.1.1 Fluorophore Selection Rationale

A review of available alternative labelling technologies separate to organic molecules is now considered.

Colloidal semiconductor nanocrystals (Quantum dots) are becoming increasingly popular in fluorescence experiments. Upon excitation of these nanocrystals with UV light, because of the confinement of the resulting electron-hole pair, they are able to fluoresce with a characteristic spectrum. The band gap energy is inversely proportional to the square of

the diameter of the nanocrystal, and hence the resulting fluorescence emission wavelength. The semiconductor cores of quantum dots are approximately 1.75 to 6.5 nm in diameter for visible wavelength emission applications. With their required passivating shells to enhance their water solubility, they are even larger, often approaching a diameter >10 nm [176], which is larger than the α-hemolysin mature pore [249]. Whilst they exhibit much greater brightness than organic fluorophores ($\sim$10 $\times$) and much improved photostability ($\sim$100 $\times$); several features render them undesirable for all applications but the tracking of dilute isolated molecules. Their large size, difficulties with photoblinking [176], stoichiometric labelling [123] and general handling made their use in this project unreasonable. Recent work has gone some way to alleviate the problems with 1:1 stoichiometric labelling using biotin ligase-based strategies with ketone isostere biotin mimics [42, 124], and through the generation of a tight-binding univalent streptavidin for biotin-streptavidin-biotin sandwich formation [122]. However only recently have successful steps been made to address the issue of QD multivalency [123]. The large surface area of passivated quantum dots usually contain multiple reactive groups for biomolecule modification. This leads to quantum dot-linked biomolecular aggregates, and also difficulty with the evaluation of labelling stoichiometry.

Fusion of the α-hemolysin gene to that of an intrinsically fluorescent protein, such as Green Fluorescent Protein (GFP) [37, 242] or other proteinaceous fluorophore derivatives has the principle advantage that 1:1 stoichiometry is guaranteed. However, as is a worry in the case of QDs, proteinaceous fluorophores are large in comparison to α-hemolysin protomers. For example, GFP and its various derivatives have molecular masses of $\sim$30 kDa, roughly the same as an α-hemolysin monomer (33 kDa).

Given the size of proteinaceous fluorophores and quantum dots, it can be argued that their appending to α-hemolysin monomers at any position would yield significant perturbations in the interaction of monomers on a membrane and their oligomerization [62]. For that reason alone, it is incumbent to chose a smaller organic molecule as the fluorescent probe, whose dimensions are comparative with a string of two or three bulky amino acids.

Many rhodamine and cyanine dyes are suitable for single-molecule fluorescence experiments. In recent years they have been incrementally improved to exhibit superior photophysical properties for single-molecule experiments. Chemical techniques have also been developed to quench the dark triplet state, hence minimising blinking [222], along with direct modifications of dyes, such as the encapsulation of both rhodamines and carbocyanines

in supramolecular assemblies [188, 299].

One particular next-generation cyanine dye (Cy3B) has been rigidified by direct chemical modification to the standard polymethine manifold [49], preventing its *cis–trans* isomerisation, as described in the general introduction (Chapter 1) [194]. The rigidification of Cy3 as Cy3B (Figure 3.1) yields a significant 7.9 × brightness improvement [49, 292]. This particular advance is appealing, as in these experiments studying α-hemolysin assembly, tracking of the fluorescent species is required over long time periods in crowded environments, where the fluorescence SNR is critical.

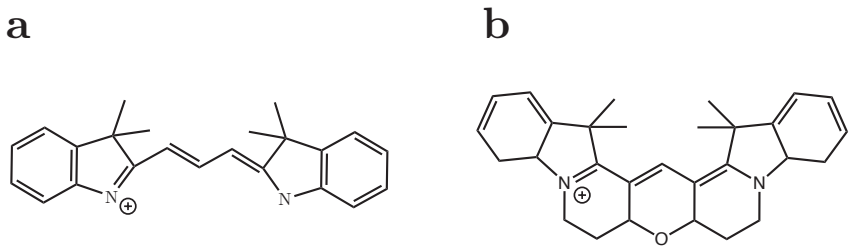

Figure 3.1: *A structural comparison of Cy3 polymethine carbocyanine dye with its next-generation derivative Cy3B.(A) The core structure of Cy3. (B) The core structure of Cy3B which is planar. The heterocycles terminating the traditional cyanine polymethine linkage are unable to rotate.*

Cy3B was hence chosen as the dye with which to label α-hemolysin. Its spectral properties allow for excitation with a standard 532 nm frequency-doubled Nd:YAG laser. A large stokes shift, large extinction coefficient of 118,000 M^{-1} cm^{-1} and a high quantum yield of 0.67, makes it particularly attractive.

3.1.1.2 Structural and Functional Considerations in Labelling

Cy3B is commercially available as a maleimide derivative. Maleimides have been shown to be highly selective and reactive with cysteine residues [91, 155]. As a result, the site-directed mutagenesis of a residue to cysteine for labelling is a sensible strategy for the conjugation of the dye with the α-hemolysin monomer.

α-Hemolysin has been shown to be exceptionally tolerant to mutations in all domains [283], with only few positions indicating significantly reduced activity upon mutation to cysteine [283]. The cavity of the pore is also able to accommodate approximately 175 exogenous amino acids ligated into the sequence genetically [143]. The lack of any endogenous cysteine residues in the wild-type sequence also widens the available positions in which a cysteine could be genetically engineered, with no concern for aberrant folding

caused by intramolecular disulphide bridge formation. In order to assist with purification, an affinity tag was introduced to enhance the ease with which the protein could be produced in large quantities and rapidly. A terminal hexahistidine motif (H_6) is short and forms little secondary structure. It is also known to produce excellent purification results in a single immobilised metal-affinity chromatography (IMAC) purification step [217].

The crystal structure of the mature α-hemolysin heptamer, solved to 1.9 Å resolution [249], shows in detail the interactions between the monomeric protomers in the mature oligomer (Figure 3.2B). However to date, no crystal structure exists of the water-soluble monomer precursor of α-hemolysin, which is the labelling target. Crystal structures do however exist for the close genetic homologue F-class protomeric subunit from the bi-component leukocidin toxin from *Staphylococcus aureus* [204], as well as of both S- and F-class monomeric subunits of the staphylococcal Panton-Valentine leukocidin (PVL) (LukS-PV and LukF-PV) [97, 212, 213]. A direct comparison of the structure in F-class monomeric subunits to the α-hemolysin monomer has been made previously [138, 204]. Despite amino acid sequence similarity of only just greater than 30%, the core of the LukF monomer structure superimposes exceptionally well onto the protomeric subunits of the α-hemolysin heptamer structure (Figure 3.2A), with the principle divergences arising from the N-terminal latch domain and the glycine-rich stem domain [48, 204]. Both domains are susceptible to proteolysis in the monomeric state, but not in the mature pore state [249, 288], indicating their presence in bulk water accessible regions of the protein. Given this information, it is reasonable to assume that if an extrinsic probe were appended to the N-terminus, conformational rearrangement upon conversion from water-soluble monomer to mature heptamer in the full length protein would be disrupted.

Genetic truncation of the N-terminal latch domain has been shown to reduce hemolytic activity on rabbit erythrocytes, although not entirely. In addition, the N-terminal latch has been shown to prevent premature oligomerization of monomers whilst diffusing freely in solution [139]. This adds to the evidence that appending Cy3B to the N-terminus could potentially be deleterious to the protein's activity. The N-terminus has also been shown to be labile in laboratory preparations, as the lysine residue at position 8 is particularly susceptible to proteolysis during expression and protein recovery in *E. coli* [41, 282].

C-terminal mutations to cysteine and their modification with 4–acetimido–4'–((iodoacetyl)amino) stilbene–2,2'–disulphonate (IASD) have been shown to affect the

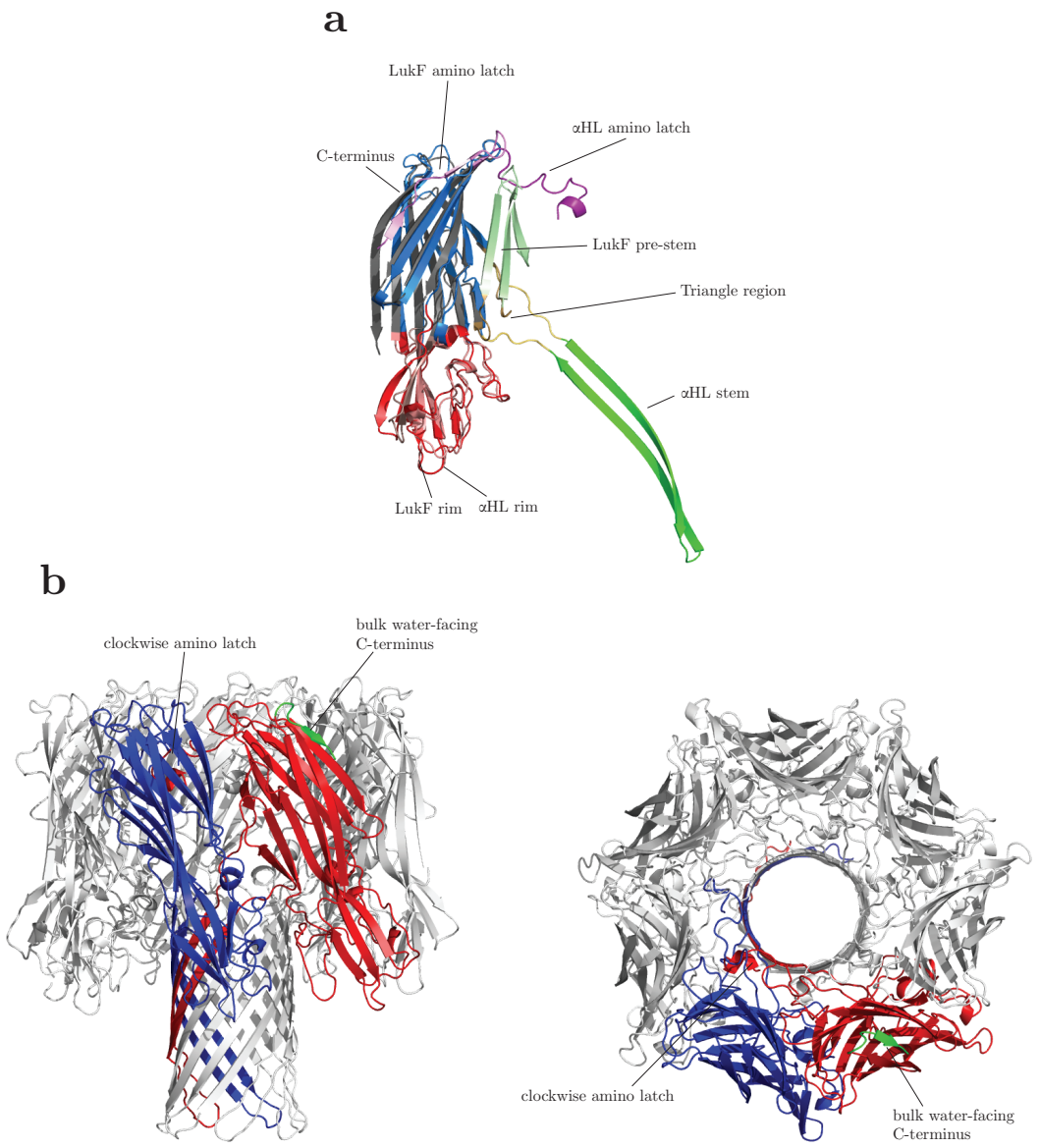

Figure 3.2: *Structural considerations in labelling the α-hemolysin monomer. (A) Superposition of the LukF crystal structure (PDB code 1lkf) with a protomer subunit of the heptameric α-hemolysin crystal structure (PDB code 7ahl). The brighter colours represent the α-hemolysin structure, the dimmer colours that of LukF. (B) Two representations of the α-hemolysin heptamer (pdb code = 7AHL). (Left = side-view) Here the amino latch from the red-coloured protomer can be seen making an interaction with the clockwise adjacent subunit inside the vestibule of the pore. The C-terminus is indicated in green protruding into the bulk water. (Right = top-view) Here the same interactions are visualised from the above the pore, showing the C-terminus facing the bulk water. The figures were created using PyMol, Delano Scientific, USA.*

hemolytic activity to a lesser extent than modifications at the N-terminus [283]. Hence, for the structural and functional reasons described above, it was decided to modify the C-terminus through a mutant cysteine with maleimido-Cy3B along with appending a hexahistidine-tag to the C-terminus.

3.1.1.3 Labelling Chemistry

Maleimides couple to thiols *via* a standard Michael addition yielding two diastereomers. Cysteine is a soft-nucleophile and does not require acidic or basic catalysis to enable conjugation to the maleimide carbon-carbon double bond. Under neutral to mildly basic conditions the reaction proceeds rapidly, yielding a succinimidyl thioether. This reaction is illustrated (Figure 3.3).

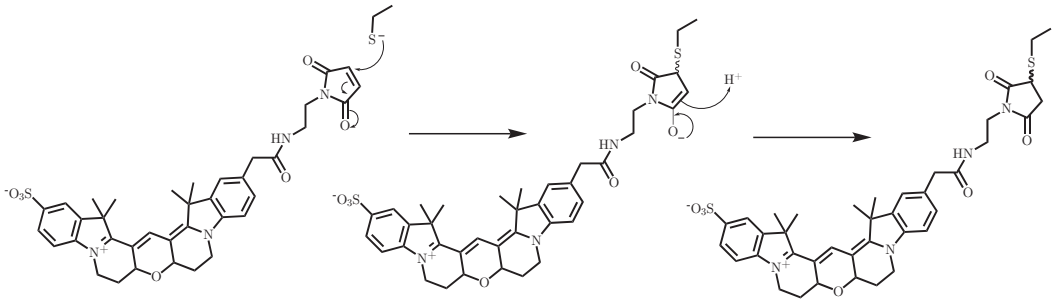

Figure 3.3: *The reaction of a thiolate anion with N-ethylmaleimido-Cy3B.*

The success of the reaction of a maleimide with the thiol in the protein depends primarily on the oxidation state of the cysteine residue, and the pH of the reaction buffer. As the reactive nucleophile is the anionic thiolate species, oxidised thiol (*i.e.* sulphonate) is unreactive, and hence it must be protected prior to conjugation. The reaction pH must also be around the pKa of the thiol to be sufficiently reactive.

The imido linkage of the maleimide to dyes has been shown to be susceptible to hydrolysis over a period of hours at pH 8.0 in TRIS buffer [91], as such it must be handled in dry conditions prior to addition to the aqueous reaction mixture containing the protein for labelling. Following labelling, the imido group of the succinimidyl moiety remains susceptible to hydrolysis under basic conditions [153]. This is however true for the majority of bioconjugations [145]. Therefore it is preferable to drop the pH of the buffering solution upon chemical attachment of the dye, in order to prevent unwanted cleavage of the dye from the protein-conjugate.

3.2 Results

3.2.1 Engineering of a Suitable Protein Construct

Two C-terminal mutants were considered for labelling-efficiency assays. The first a mutation of the threonine at position 292 to cysteine (T292→C), demonstrated previously [283]. The second an addition of a cysteine after the end of the protein at position 293+1 (294C). A hexahistidine amino acid affinity tag could be engineered after the C-terminal end of the α-hemolysin gene, enabling straightforward high-stringency purification and protein handling during labelling.

Secondary structure occuring at modified protein-termini can lead to difficult purification with affinity tags. As a result it was decided that two separate constructs would be trialled. One containing a long flexible linker between the end of the protein chain and the start of the affinity tag, the other containing a shorter two-amino acid linker before the tag, the engineering of which is described below.

3.2.1.1 PCR

The T292C-long linker-H_6 construct was engineered by PCR from a template α-hemolysin wild-type gene, containing a long-linker and hexahistidine tag[1]. The 294C-short linker-H_6 construct, albeit with a non-silent mutation, had already been prepared previously in the laboratory of Prof. Hagan Bayley and was offered as a gift.

The gene-encoding pT7-SC1 [41] vectors were linearised by restriction digestion. The use of a double digest, excising a fragment of the plasmid prior to PCR, improves the probability of recovering the mutant plasmid and not the template from transformed bacteria. This negates the requirement for the destruction of the template, through for example a DpnI endonuclease digestion. For each nicked vector, two primers were designed (one with a mutation inducing mismatch) and one as the opposing opposite strand primer. Two separate PCR reactions were performed, one for each construct to mutate the desired residues as illustrated (Figure 3.4). The procedure was identical for both constructs.

Following PCR and *in vivo* recombination of the plasmids, the products were mini-prepped and sequenced by dideoxy sequencing to verify the results of the mutagenesis.

[1] gift from Dr. Stephen Cheley

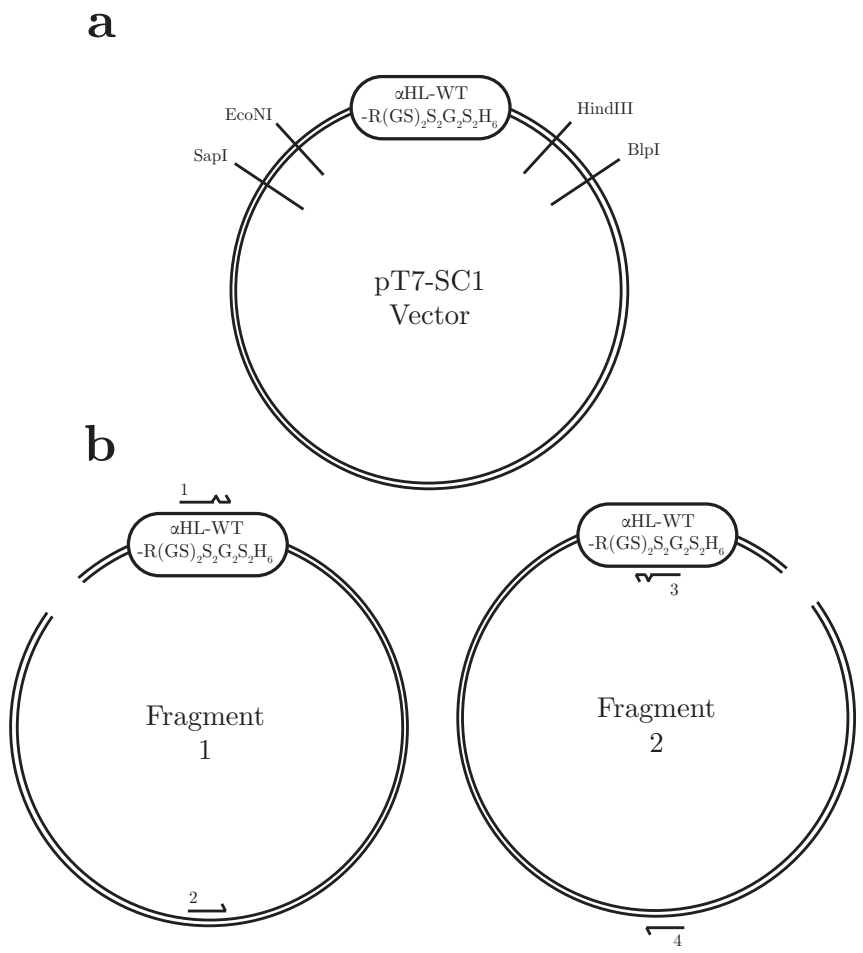

Figure 3.4: *(A) A schematic diagram of the double restriction digest pairs in the pT7-SC1 vector encoding the αHL WT-R(GS)$_2$S$_2$G$_2$S$_2$H$_6$ gene. (B) A schematic diagram of the two sets of PCR reactions performed on the two restriction fragments. Primers 1 and 2 are used to generate one half of the vector and gene (primer 1 contains the mismatch, primer 2 is perfectly complementary), primers 3 and 4 are used in a separate reaction to generate the other half of the gene and vector. Primers 1 and 3, and primers 2 and 4 are perfectly cognate. Following PCR, in vivo recombination of the two halves of the vector was performed through equimolar cotransformation of E. coli with both products to generate the final product vector encoding the (T292C-long linker-H$_6$) αHL T292C-R(GS)$_2$S$_2$G$_2$S$_2$H$_6$ gene. The process to correct the mutation in the (294C-short linker-H$_6$) αHL 294C-S$_2$H$_6$ construct was identical, using alternative primers to 1 and 3.*

3.2.1.2 Protein Activity Verification

The measurement of the activity of any protein modified with a biophysical probe versus its wild-type counterpart is an important control. Fortunately, α-hemolysin is straightforward to assay for its activity, being highly hemolytic against intact rabbit erythrocytes [113]. If rabbit erythrocytes are incubated with α-hemolysin monomers, the erythrocytes will be spontaneously lysed at a concentration-dependent rate due to pore formation and hence induced osmotic-stress. This lysis leads to a decrease in light scattering if the turbidity

is monitored in a spectrophotometer. Hemolytic assays in microtitre plates therefore allow for the direct comparison of activity between different protein constructs at a fixed concentration.

In vitro production of the α-hemolysin protomer is possible using a pT7 vector-encoded gene using *E. coli* extracts, as described in the previous chapter. This so-called coupled *in vitro* transcription and translation (IVTT) is capable of producing nanomolar concentrations of radiolabelled protein in small volumes suitable for gel-extraction and reconstitution into lipid bilayers, or assaying the activity of a particular mutant versus others. It is assumed that the IVTT expression levels of α-hemolysin protomers is equivalent for all mutants under the control of the same promoter in the same vector. Hence, hemolysis assays were performed to compare the activity of the αHL T292C-R$(GS)_2S_2G_2S_2H_6$ with respect to the αHL 294C-S_2H_6 construct (Figure 3.5). The most active mutant would be selected for subsequent labelling assays in preference of the mutant with diminished activity. Comparison of the labelled mutants with respect to the wild-type protein is discussed in Section 3.2.4. Here IVTT provides a straightforward means of protein production with calibrated quantities, enabling a simple direct comparison of the protein activities. During the comparison of activity of labelled and unlabelled protein, IVTT production was not possible as spectroscopic calibrations of protein quantity are required (Section 3.2.4).

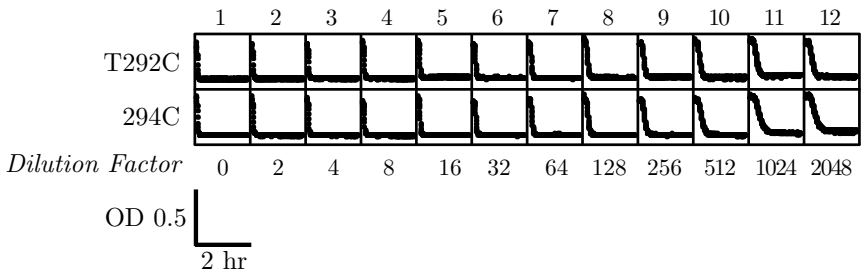

Figure 3.5: *A hemolytic assay comparing the activities of the αHL T292C-R$(GS)_2S_2G_2S_2H_6$ and αHL 294C-S_2H_6 mutants against intact rabbit erythrocytes. Each box represents a light-scatter vs. time plot (therefore monitoring the hemolysis process for a given concentration) with each box being a serial two-fold dilution going from left to right. The box axes correspond to the illustrated magnitudes at the bottom left.*

No difference in activity is observed from IVTT-produced protein between the two mutants. Both mutant constructs were as a result assayed for expression levels in bacteria.

3.2.1.3 Overexpression Trials

Overexpressed protein is a necessary requirement when high-stringency purification will be performed, resulting from the fact that large proportions of the protein will be lost as multiple purification procedures are performed in serial. Wild-type α-hemolysin is relatively straightforwardly produced from *Staphylococcus aureus* Wood Strain 46. However, mutant forms of the protein are more difficult to express. This process involves multiple cloning steps from different shuttle vectors between *E. coli* DNAs and *Staphylococcus aureus* for expression. As the protein is secreted from the cells, the purification of the protein then involves the handling of large volumes of liquid broth which must be filtered of all bacteria prior to ammonium sulphate precipitation, dialysis and ion exchange chromatography. This process is tedious, but is capable of yielding large quantities of protein.

Another critical consideration in the handling of a cysteine mutant protein is speed of preparation. Particularly when a maximal amount of reduced cysteine is required. A lengthy ammonium sulphate precipitation will require difficult cysteine protection and may hinder the chromatography processes downstream. As a result, it is incumbent to choose a strategy for overexpression which is fast, produces large yields in small culture volumes and is compatible with a straightforward rapid purification procedure.

Heptameric α-hemolysin can be prepared using IVTT protein and rabbit erythrocyte membranes (rRBCMs) for oligomerization [289]. Autoradiography is used to image gels, whereafter the appropriate band corresponding to heptamer can be excised and filtered to remove the gel matrix. An advantage of this procedure is the ability to generate thiol-containing protein rapidly and label it in one reaction mixture. However, the stringent purification of such small quantities of protein is practically impossible. In addition, monomeric α-hemolysin is intolerant to SDS in solution, which renders this means of protein production unsuitable.

Therefore, overexpression trials in standard *E. coli* strains were performed. These strains were all of the DE3 genotype (bacterial chromosomal DNA-encoded T7 polymerase), optimised for highly-regulated overexpression of pT7 vector-encoded genes with isopropyl β-D-thiogalactopyranoside (IPTG) induction. *E. coli* strains were transformed with the plasmids generated by PCR, encoding the αHL T292C-R$(GS)_2S_2G_2S_2H_6$ and αHL 294C-S_2H_6 constructs.

Results demonstrated excellent yields of both protein constructs in all three bacterial

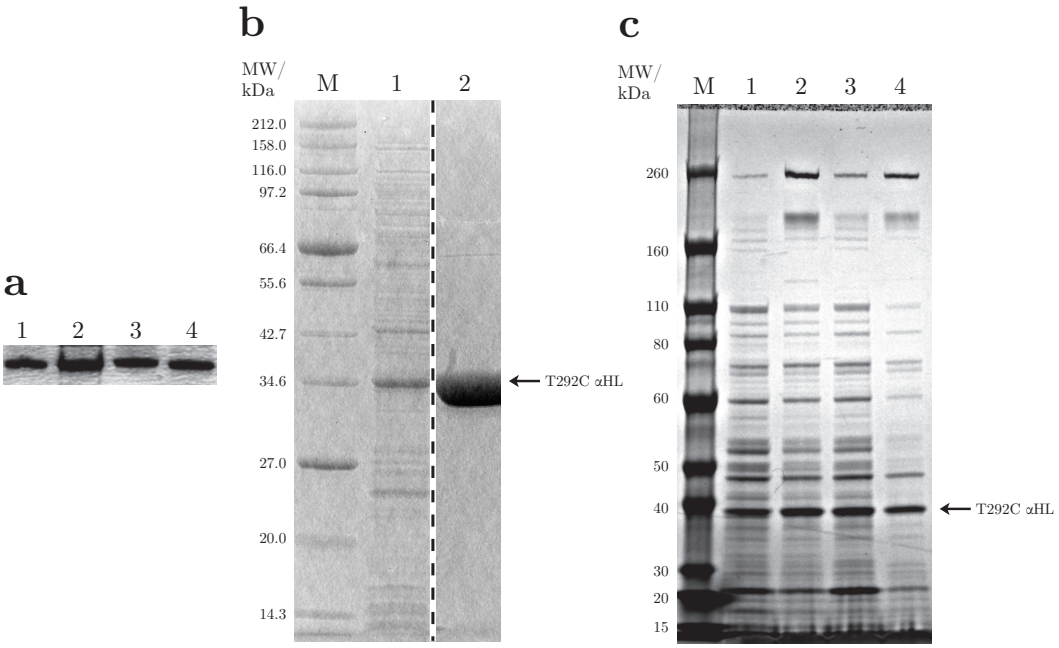

Figure 3.6: *E. coli overexpression trials results. (A) An image of a Coomassie-stained 12% BIS-TRIS SDS-PAGE gel following electrophoresis showing the relative yields of αHL T292C-R(GS)$_2$S$_2$G$_2$S$_2$H$_6$ (1,3) and αHL 294C-S$_2$H$_6$ (2,4) in JM109(DE3)(1,2) E. coli and BL21(DE3)pLysS (3,4) E. coli. (B) A composite image of a Coomassie-stained 12% BIS-TRIS SDS-PAGE gel following electrophoresis (separate lanes composited as single block from different positions on a single gel, boxes show lane edges) showing αHL T292C-R(GS)$_2$S$_2$G$_2$S$_2$H$_6$ overexpression in the cytosolic fraction of an IPTG induced BL21(DE3)pLysS E. coli culture(1), the product of a crude Ni^{2+}-NTA IMAC purification is also shown (2). The total yield from a 1 L culture equalled approximately 10 mg. (C) An image of a Coomassie-stained 4-12% Gradient TRIS-TRICINE SDS-PAGE gel following electrophoresis showing the relative yields of αHL T292C-R(GS)$_2$S$_2$G$_2$S$_2$H$_6$ in BL21(DE3)pLysS and BL21(Rosetta)pLysS strains. Lanes 1 and 2 show the uninduced and induced crude cell extracts from BL21(DE3)pLysS, lanes 3 and 4 show the uninduced and induced crude cell extracts from BL21(Rosetta)pLysS. Lanes in all gels are normalised for total protein concentration according to absorbance at 280 nm.*

strains (Figure 3.6A). The only difference in the different mutant's expression in JM109 and BL21 strains is the apparent growth rate of the bacteria. JM109(DE3) bacterial cultures reach log-phase growth considerably slower than BL21(DE3)pLysS cultures (data not shown). BL21(DE3)pLysS bacteria also harbour the pLysS plasmid encoding T7 lysozyme. Lysozyme controls the expression more tightly, down-regulating the expression of the target gene under the control of the T7 promoter without interfering with its expression post-induction with IPTG. Its presence in the cytosol of the bacteria also facilitates a more straightforward recovery of bacterial cytosolic components, easing cell lysis after overexpression.

For these reasons, the BL21 strain was chosen as the overexpression strain for subsequent

experiments. A crude Ni^{2+}-NTA IMAC purification is shown (Figure 3.6B). The total yield of αHL T292C-R$(GS)_2S_2G_2S_2H_6$ from a 1 L culture is approximately 10 mg. As there was no appreciable difference between the expression levels of αHL T292C-R$(GS)_2S_2G_2S_2H_6$ and αHL 294C-S_2H_6, the longer-linker αHL T292C-R$(GS)_2S_2G_2S_2H_6$ was chosen in preference due to its expected increased hexahistidine-tag flexibility. A direct comparison of two different strains of BL21-derived bacteria is shown (Figure 3.6C). The Rosetta strain of BL21 is optimised for expression of mammalian genes, however it is clear that the total cell content of α-hemolysin following induction is improved versus that of BL21(DE3)pLysS. This expression system was used in preference for the α-hemolysin production described below.

3.2.2 Cysteine Reactivity Assay

In order to design a suitable and efficient cysteine labelling strategy, a range of conditions were assayed using SDS-PAGE as a means to visualise protein modification, an electrophoretic mobility shift assay (EMSA). Appending a large moiety to a protein, such as a polymer, can result in a change in its electrophoretic mobility. A polyethylene glycol compound ($MW \approx 5000\ Da$) with a terminal maleimide moiety (PEGm) was used in these experiments to label the mutant cysteine residue in the αHL T292C-R$(GS)_2S_2G_2S_2H_6$ protein under a range of different conditions.

Conditions testing the required molar ratios of PEGm versus protein were assayed between 1:1 molar equivalence of PEGm and 50:1. Disulphide bond reducing agents were also assayed for their relative efficacies. The length of time of reactions was varied between 15 minutes and 16 hours. And the solution pH was found to not have a significant effect on the rate of reaction between the values of 7.0 and 8.0. Tests were also performed to deduce the preferred method for terminating the reaction, including dropping the pH of the solution dramatically and addition of a large excess of β-mercaptoethanol to quench the maleimide.

These experiments enabled the design of a reliable labelling procedure which could yield in excess of 50% of total overexpressed protein being labelled. The following reaction parameters were chosen as being optimal following multiple trial reactions. The preferred solvent for dye solubilisation is dimethylformamide (DMF), as dimethylsulphoxide (DMSO), the manufacturer's suggested solvent was found to promote thiol oxidation. A divalent metal cation scavenger, such as EDTA, or a solid-state divalent cation binding resin such

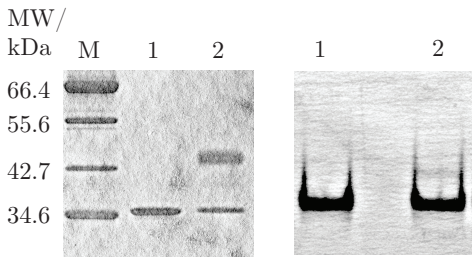

Figure 3.7: *Electrophoretic mobility shift assays for labelling efficiency. An image of a Coomassie-stained SDS-PAGE gel following electrophoresis of pure αHL T292C-R(GS)$_2$S$_2$G$_2$S$_2$H$_6$ protein and protein following labelling with PEGm. The protein prepared as described in methods and following gel filtration was incubated with TCEP for 1 hour. Lane 1 illustrates protein without any added PEGm and Lane 2 illustrates reduced protein following an hour long reaction with PEGm. The gel on the right illustrates the effectiveness of labelling if no TCEP is added. Lane 1 shows control protein with no added PEGm, Lane 2 illustrates protein following a 1 hour incubation with PEGm. In both gels reactions were performed at room temperature with degassed buffers. PEGm was dissolved in dry DMSO in both experiments and added to the protein in 10:1 molar excess. In the first gel a clear band is visible approximately 5000 Da heavier than the unreacted protein in lane 2. All experiments were terminated by addition of a large excess of β-mercaptoethanol containing gel loading buffer prior to immediate electrophoresis. All cysteine reactivity experiments were carried out in this manner, by monitoring the relative amounts and positions of molecular-weight shifted products following different reaction condition trials.*

as CHELEX can protect thiols from oxidation. Degassed reaction buffers greatly enhance the stability of the reduced state of the thiol. Reduction of disulphide bonds (cystines) was most efficient using dithiothreitol (DTT), as this reagent will always yield reduced thiol and avoids potential covalent attachment as is the case with β-mercaptoethanol or β-cysteamine. It was also found that phosphine-based disulphide reducing agents are highly reactive with the maleimide, expected given phosphine's high nucleophilicity. This was in contrast to the manufacturer's literature, however in keeping with reports which have shown this reactivity with maleimides [85, 240]. As all tested reducing agents were found to detrimentally reduce the labelling efficiency if present during the labelling reaction, their removal was of great importance before the addition of the dye to the protein solution for labelling [85].

Maleimide is susceptible to hydrolysis under basic conditions, hence an intermediate pH of 8.0 was found to be optimal for labelling the cysteine in αHL T292C-R(GS)$_2$S$_2$G$_2$S$_2$H$_6$. At a pH slightly lower than the predicted pK_a of 8.3, the reaction was found to progress to completion within 15 minutes at room temperature, where the molar excess of dye to protein was 10:1. These conditions were then translated into a larger scale purification and labelling strategy.

3.2.3 Large-Scale Purification and Labelling

A sufficient quantity of protein for labelling stoichiometry assays in bulk, as well as sufficient quantities for single-molecule experiments was required from a scaled-up preparation of α-hemolysin. Following Ni^{2+}-NTA IMAC, the disulphide bonds would be reduced by immediate addition of β-cysteamine or DTT following column elution.

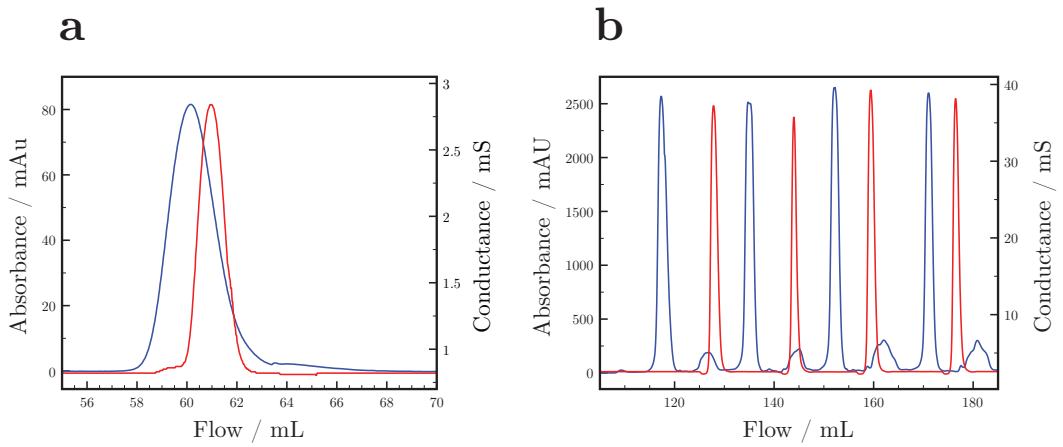

Figure 3.8: *Removal of disulphide bond reducing agents using solid-state resins. (A) A chromatogram showing unsuccessful removal of β-Cysteamine from a pure αHL T292C-R(GS)$_2$S$_2$G$_2$S$_2$H$_6$ protein sample following reduction. The small column did not enable a complete separation of reducing agent as illustrated by the overlap of the protein sample (blue trace) with the salt-peak (red trace). (B) A chromatogram showing multiple successful removals of DTT from a pure αHL T292C-R(GS)$_2$S$_2$G$_2$S$_2$H$_6$ protein sample following reduction. Here, four separate plugs of 1 mL protein were loaded onto the column at roughly 20 mL flow intervals. Efficient desalting, and therefore removal of reducing agent is evidenced by the clear separation of protein (blue trace) and salt-peak (red-trace). The columns used were as follows A = GE Healthcare HiTrap Desalting column (containing Sephadex G-25 superfine gel filtration medium), pumped at 1 mL min^{-1} flow rate, 1 mL protein plug loaded, B = GE Healthcare Tricorn Superdex 200 10/300 GL Gel Filtration column, pumped at 1 mL min^{-1} flow rate, 1 mL protein plugs loaded. Both experiments used 10 mM TRIS-HCl buffered 150 mM NaCl at pH 8.0 as the mobile phase.*

A means to remove the reducing agent from solution is required prior to the addition of the dye to protect it from quenching. The use of β-cysteamine and DTT enables efficient removal using a variety of standard lab techniques. The most straightforward means to do this is through the use of a solid-state resin in a column. Two types of column were trialled. The first, a specialised desalting column, showed poor removal of the reducing agent from solution (Figure 3.8A), whereas a larger gel filtration size-exclusion column demonstrated excellent removal (Figure 3.8B). This procedure was carried out in buffer containing no additional salt. Low ionic strength is a necessary requirement for good binding to the cation exchange resin in the next step.

Thereafter dye can be added to the solution, having been solubilised in DMF, with a final

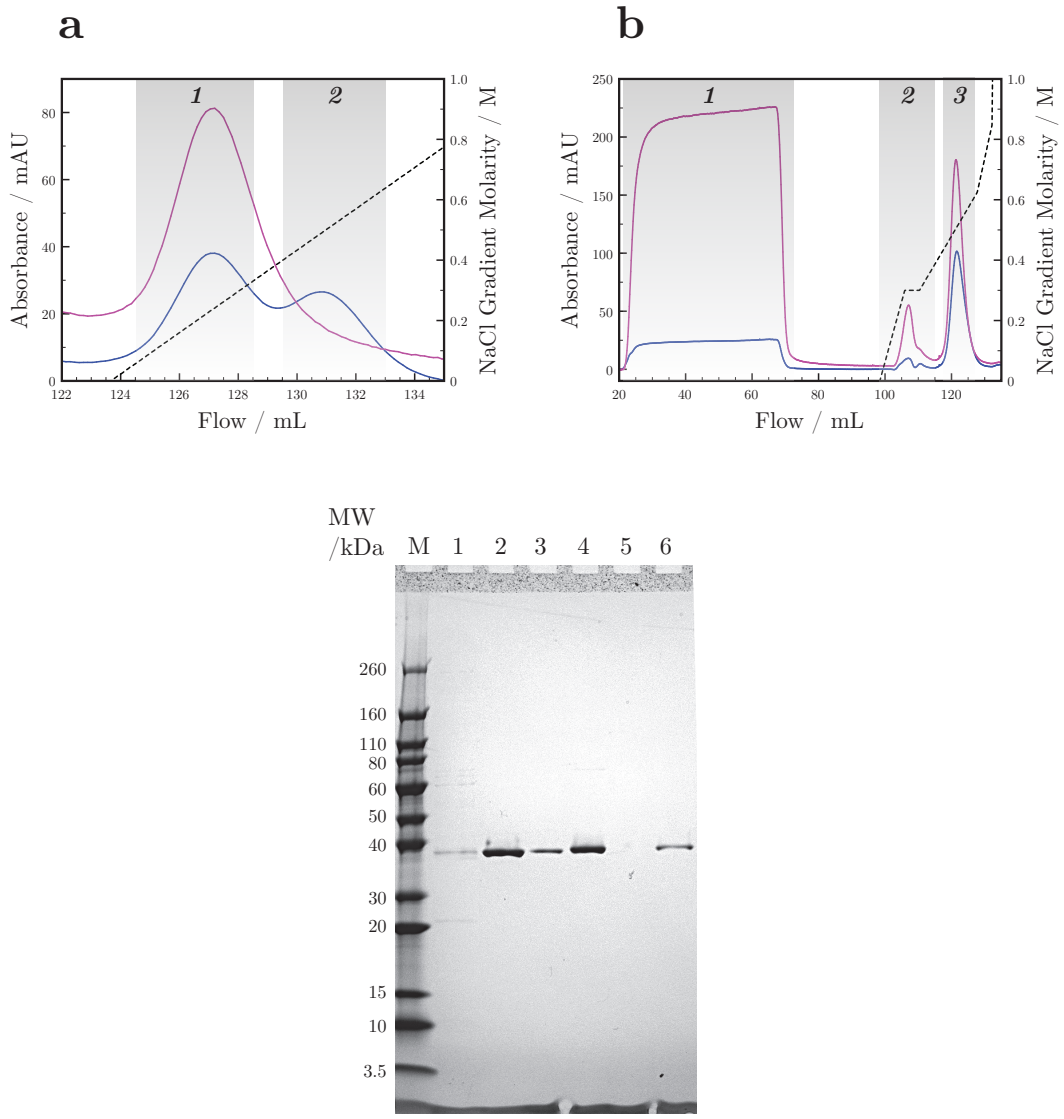

Figure 3.9: *The complete process of labelling α-hemolysin. (A) A chromatogram showing the separation of Cy3B-labelled and unlabelled αHL T292C-R(GS)$_2$S$_2$G$_2$S$_2$H$_6$ protein following reduction with β-cysteamine. The blue trace corresponds to absorbance in the UV at 280 nm (protein and dye combined), the pink trace corresponds to the absorbance of the dye at 560 nm. Band 1 shows the first eluate, labelled protein absorbing in the green/yellow and UV. Band 2 shows the secondary eluate, unlabelled protein absorbing in the UV. (B) The entire process of cation exchange chromatography for the removal of free dye from DTT-reduced and Cy3B-labelled protein. Band 1 shows the free dye eluting from the column during protein binding. Band 2 shows the elution of weekly bound labelled protein, whereas band 3 shows the elution of pure Cy3B-labelled protein. The image of a Coomassie-stained gel shows the entire process of purification and labelling from overexpression to post-cation exchange pure labelled protein. Lane 1 shows crude supernatant following resuspension of bacterial cytosol following overexpression. Lane 2 shows the principle eluate from the Ni^{2+}-NTA IMAC purification. The protein is then gel filtered using a GE Healthcare Tricorn Superdex 200 10/300 GL column following DTT reduction, lane 3. Lane 4 illustrates the protein sample after labelling but prior to cation exchange. Lane 5 corresponds to the dye flow-through band 1 in chromatogram B. Lane 6 corresponds to the final product Cy3B-labelled protein eluate band 3 in chromatogram B. All lanes were normalised by absorbance in the UV, factoring in absorbance of the dye (∼12% of 560 nm absorbance).*

concentration of DMF no greater than 1% (v:v) to avoid damaging the protein. The time the protein can persist in solution without reforming a significant quantity of disulphide bonds is not characterized, however this length of time prior to addition of dye was kept as short as possible after elution from the column. After 15 minutes at room temperature, the reaction was quenched by addition of a large excess of MES buffer at pH 5.5. The ionic strength therefore being sufficiently low, and the protein being sufficiently protonated (approximately 3 pH units lower than the pI at pH 5.5) for strong binding to the sulphonyl-propyl cation exchange resin. Elution was performed using a gradient of MES buffered 1 M NaCl at pH 5.5 (Figure 3.9B).

3.2.4 Bulk Characterization of Labelled Monomeric α-Hemolysin

Labelled protein stored in MES buffer at pH 5.5 was hemolytically assayed against intact rabbit erythrocytes, versus wild-type protein produced from *Staphylococcus aureus* Wood Strain 46[2] and hexahistidine-tagged α-hemolysin overexpressed in *E. coli* (IMAC and gel filtration purified), as described previously. Protein concentrations were normalised by Bradford assay. The results show roughly equal activities between the three proteins (Figure 3.10). This result demonstrates that the separate addition of a hexahistidine-tag and an extrinsic fluorophore to the α-hemolysin monomer has no deleterious effect upon the activity of the protein against rabbit erythrocytes.

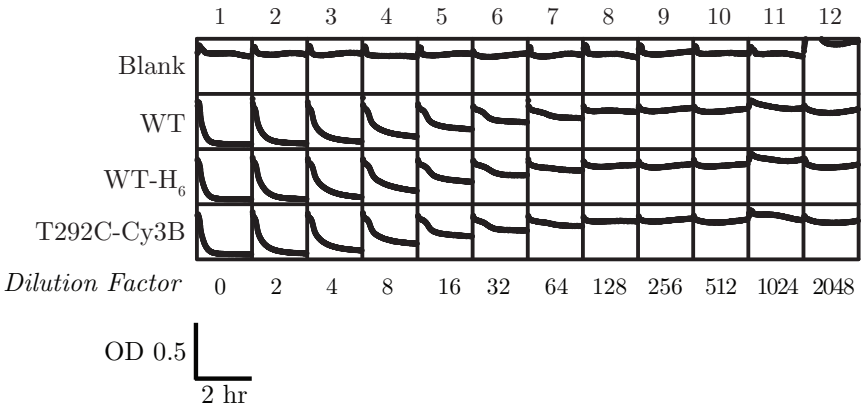

Figure 3.10: *A hemolytic assay comparing the activities of the wild-type α-hemolysin (WT) from Staphylococcus aureus Wood Strain 46 with hexahistidine-tagged wild-type α-hemolysin αHL-R(GS)$_2$S$_2$G$_2$S$_2$H$_6$ (WT-H$_6$) and Cy3B-labelled αHL T292C-R(GS)$_2$S$_2$G$_2$S$_2$H$_6$ (T292C-Cy3B) against intact rabbit erythrocytes. Numbers indicate a serial two-fold dilution going from left to right. The box axes correspond to the illustrated magnitudes at the bottom left.*

[2]gift from Qiuhong Li

In order to quantify the stoichiometry of appended Cy3B dye to protein, the absorbance of the dye in the visible spectrum was compared to that of the protein and dye in the UV (Figure 3.11B). This pure labelled protein eluate from cation exchange was separated by reverse-phase high-performance liquid chromatography (RP-HPLC), yielding a single symmetrical peak (Figure 3.11A). Briefly, the protein was injected and bound to a hydrophobic interaction C:18 column in 0.1% (v:v) formic acid, 10% (v:v) acetonitrile (AcN) and 99.9% (v:v) MQ water. The protein was then eluted by increasing the acetonitrile concentration. The Cy3B-labelled protein's absorbance spectrum was analysed as it eluted from the column by in-line UV-Vis spectrophotometry using a photo-diode array (PDA). The relative absorbance of the dye at 280 nm versus that at its absorbance maximum at 560 nm are known from spectra taken of pure dye to be 12%. Hence, the stoichiometry of the dye molecules in the sample versus protein molecules could be directly calculated from the absorbance spectrum.

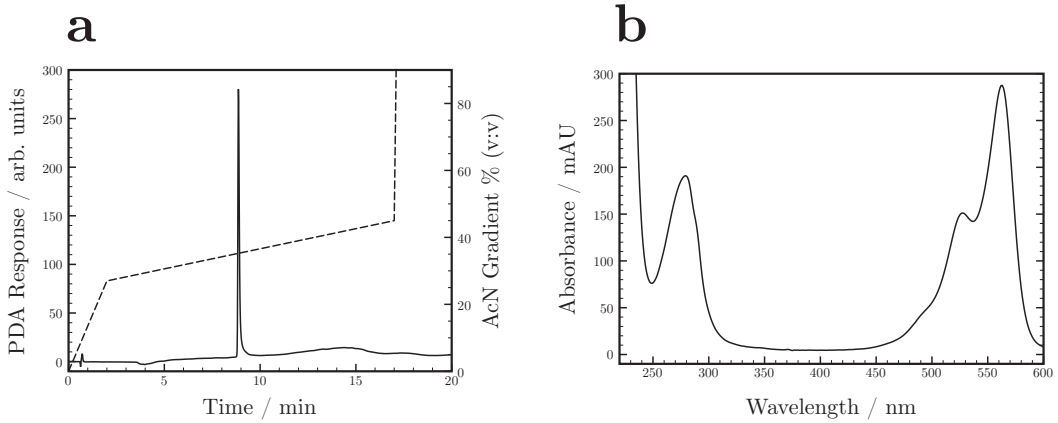

Figure 3.11: *Stoichiometric analysis of Cy3B-labelled αHL T292C-R(GS)$_2$S$_2$G$_2$S$_2$H$_6$ by UV-Vis Spectrophotometry. (A) A RP-HPLC chromatogram showing the separation of the dye-labelled protein from salt by adsorption to and elution from a hydrophobic interaction C:18 matrix. (B) The PDA-captured spectrum of the eluate shown in the chromatogram. The Cy3B dye absorbs in the UV and visible regimes, however the protein absorbs only in the UV (i.e. intrinsic aromatic residue absorbance e.g. Trp).*

The absorbance values are: 560 nm = 287.4, 280 nm = (190.6∗0.88) = 167.7. Therefore according to the Beer-Lambert relationship,

$$A = \xi C D \tag{3.1}$$

where A is absorbance, ξ is the molar absorption coefficient, C is the concentration and D

is the path length. The concentration of the dye is 2.6 μM, and the concentration of protein is 2.4 μM giving a labelling ratio of dye to protein of 1.08:1. This ratio is indicative of a highly efficient labelling procedure where on average one dye molecule is appended to every protein molecule. The single peak eluting from the hydrophobic interaction chromatography is indicative of the sample following labelling and cation exchange being extremely pure, and also therefore containing no free dye.

Further analysis was performed by mass spectrometry in order to verify the state of the Cy3B-labelled protein. Protein mass spectrometry is easily capable of resolving single amino acid substitutions, for example by mutation, and even oxidation states of amino acids or modifications such as dye molecules. An electrospray (ESI) spectrum by time-of-flight (TOF) detection was acquired for the eluate of the RP-HPLC procedure (Figure 3.12A). The spectrum was deconvolved by a maximum-entropy method to give a mass equal to 35,558.05 $\pm$ 3.61 Da, whereas the predicted mass equals 35,556.35 Da. This mass is within error of the calculated predicted mass of the protein plus the Cy3B appendage covalently attached to the engineered cysteine residue at position 292.

3.2.4.1 Labelling α-Hemolysin Heptamers during IMAC

Further work pursued the labelling and purification of preformed heptameric α-hemolysin. A method was developed to label the protein whilst immobilised on a metal affinity column. α-Hemolysin when expressed in the manner described above for monomeric labelling also exists as heptamers in the overexpressing bacteria and the heptamer is known to be stable in SDS. It can therefore be extracted from a crude suspension of bacteria following overexpression by solubilisation with SDS-containing buffer. Most of the cytosolic and membrane resident proteins will precipitate under these conditions, including the large majority of monomeric α-hemolysin molecules present.

Due to the presence of seven hexahistidine tags in the heptameric α-hemolysin complex, it is possible to bind the protein, even in the prescence of a strong denaturant such as SDS, to a Ni^{2+}-NTA column. Elution of non-hexahistidine-tagged proteins and residual monomeric α-hemolysin can be performed by increasing the concentration of imidazole in the eluent to below the critical concentration for heptamer elution. Thereafter dye can be injected into the column to react with cysteines on the matrix-adsorbed proteins. The free unreacted dye can be washed off the column with buffer as it is not adsorbed strongly to the column.

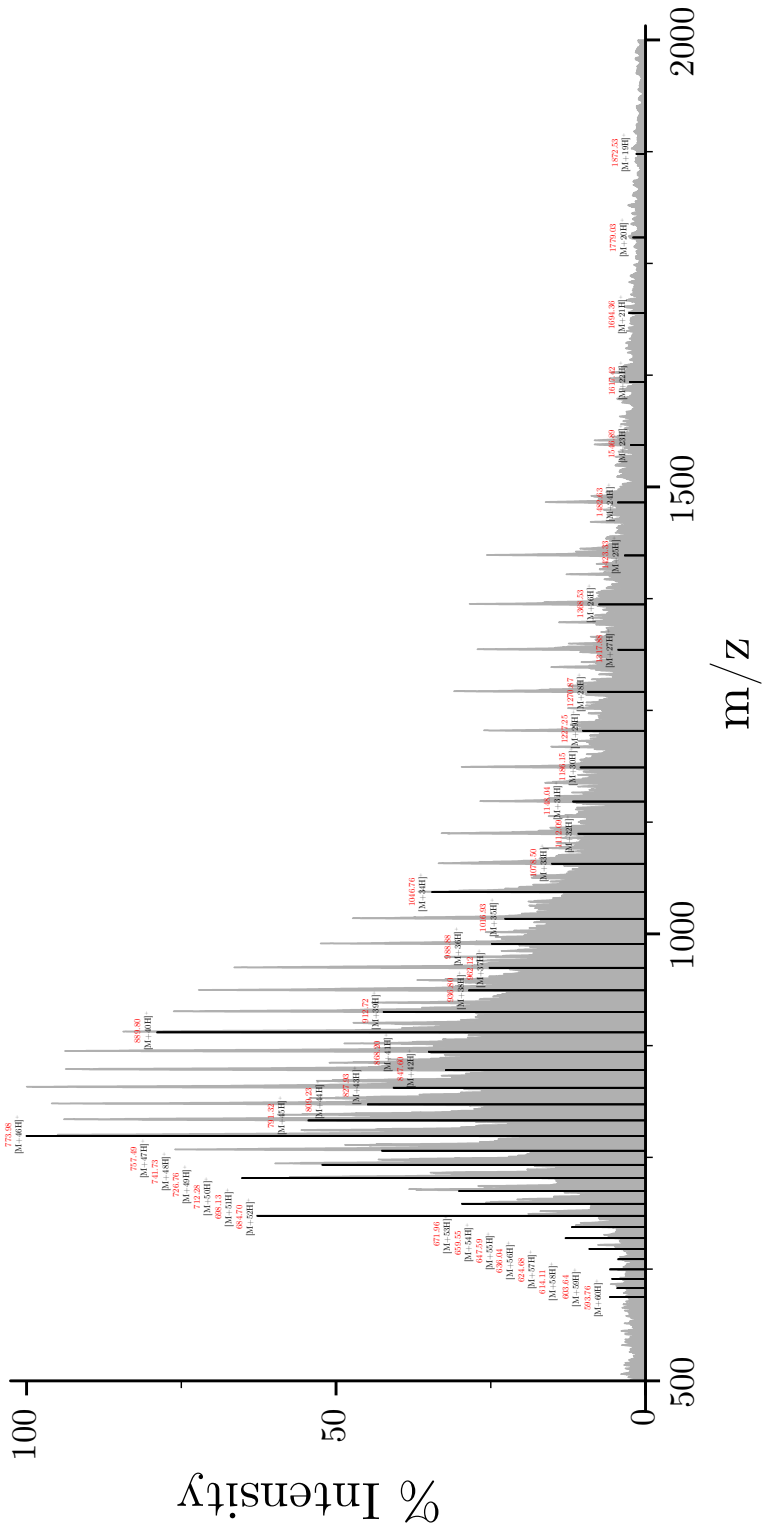

Figure 3.12: *Positive-mode ESI-TOF mass spectrum for pure Cy3B-labelled αHL T292C-R(GS)$_2$S$_2$G$_2$S$_2$H$_6$. The spectrum is deconvoluted to give a mass equal to 35,558.05 ± 3.61 Da. Peaks assigned in the deconvolution are assigned (black peaks) with their masses and proton-adduct stoichiometric classifications given.*

A standard gradient elution with imidazole can then be performed to elute the remaining dye-labelled heptameric complexes. This procedure is shown (Figure 3.13A). SDS-PAGE analysis following labelling shows that the labelled heptamer is highly pure and stable, with no monomeric α-hemolysin present in the heptamer eluate fraction(Figure 3.13B).

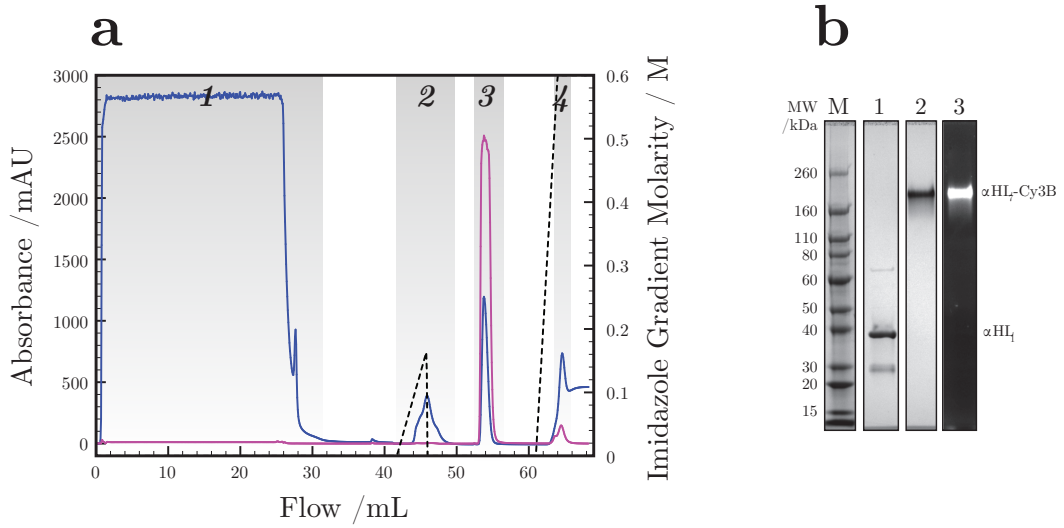

Figure 3.13: *Heptamer labelling with Cy3B during immobilisation on a Ni^{2+}-NTA column. (A) A chromatogram showing the immobilisation injection and binding of α-hemolysin heptamers in 1% (w:v) SDS solubilised heptamers to a 1 mL Ni^{2+}-NTA resin in 0.1% (w:v) SDS buffered with TRIS-HCl at pH 8.0 containing 0.5 M NaCl. Band 1 shows the elution of unbound proteins from the column. Band 2 shows the elution of weakly-bound proteins from the column using a gradient of imidazole up to 150 mM concentration. Band 3 shows the injection and elution of Cy3B-maleimide dissolved in binding buffer. The dye was left on the column for 30 minutes to react prior to elution. Band 4 shows the fraction containing heptameric α-hemolysin being eluted from the column using an imidazole gradient. (B) A composite image of a gel imaged by Coomassie staining and UV illuminated fluorescence imaging. Lane 1 shows the fraction from the chromatogram corresponding to band 2. Lane 2 shows the fraction from the chromatogram corresponding to band 4 by Coomassie staining. Lane 3 shows the same as lane 2 imaged by UV-illuminated fluorescence imaging.*

3.3 Discussion

The production of pure singly-labelled α-hemolysin is of paramount importance for single-molecule measurements of its assembly pathway using fluorescence microscopy. Any free dye or multiply-labelled monomeric α-hemolysin species could prevent accurate designation of complex stoichiometry in imaging.

Overexpression of monomeric and heptameric α-hemolysin is shown in bacteria yielding as much protein as 10 mg L^{-1} following the first stage of purification. The protection of an engineered cysteine residue at the protein's carboxyl terminus is achieved using DTT. DTT

has a high-propensity to cyclise to release itself from the protein [46], therefore yielding more reactive cysteines versus other reducing agents tested here [85]. The use of degassed buffers, DMF to solubilise the dye, EDTA to prevent oxidation of the thiol and cold-temperatures also enable a better labelling yield.

Labelling the protein construct at pH 8.0, in an excess of primary-amine containing buffer (TRIS), gives highly directed modification of the protein at the cysteine residue specifically. The pH of the reaction is too low to label any intrinsic primary amines of the protein, such as those at the amino terminus or of lysine side-chains, however it is close enough to the pKa of cysteine to ensure the cysteine is significantly anionic to be reactive towards a maleimide carbon-carbon double bond. Stoichiometric analysis following labelling and purification by cation exchange and RP-HPLC shows close to 1:1 labelling of protein molecules with the rigidified cyanine dye, Cy3B. Mass spectrometry confirms the analysis by spectrophotometry, showing a labelling product within error of the mass of the predicted labelled protein species. Final quantities of pure labelled product using this protocol from a litre culture of bacteria are approximately 1-2 mg.

Further efforts to label the preformed heptameric mature form of α-hemolysin show effective labelling of the pore and its straightforward purification in a single chromatographic step, yielding large quantities. The principle of labelling a detergent-solubilised membrane protein complex shown here could assist in the labelling of other obligate membrane protein complexes in the future for single-molecule fluorescence experiments. For example, this technique could be used with other milder detergents to fluorescently label ion channels expressed in any expression system. Whilst the stoichiometry of labelling is harder to quantify versus a monomeric water-soluble globular protein, this technique could yield significant time and effort advantages over other current techniques.

3.4 Conclusions

The selective labelling of α-hemolysin monomers for single-molecule fluorescence microscopy analysis of its assembly pathway is demonstrated. Yields are high, enabling rigorous quantification of labelling success and stoichiometry. The products shown in this chapter were used for the single-molecule imaging of the assembly pathway of α-hemolysin described in Chapter 6.

3.5 Materials and Methods

3.5.1 Materials

Unless otherwise stated, all chemicals were from Sigma (Sigma-Aldrich Ltd, Gillingham, U.K.). Triton X–100 detergent, acrylamide, β-mercaptoethanol (2–ME) and nucleic acid gel loading buffer were from Bio-Rad (Bio-Rad Laboratories, Hercules, CA). *E. coli* bacteria stocks were from Promega (Promega, Madison, WI) apart from Rosetta cells which were from Novagen (EMDBiosciences, U.K.). Doubly-deionised 18 MΩ cm^{-1} water (Millipore Corporation, Billerica, MA) was used throughout unless otherwise stated. Dioxane-free isopropyl–β–D–thiogalactopyranoside (IPTG) was from Calbiochem (EMD Biosciences Inc, San Diego, CA). All chromatography equipment and Cy-dyes were from GE Healthcare (GE Healthcare Life Sciences, Amersham, U.K.). Restriction enzymes, their buffers and additives and Phusion (Finnzymes) DNA polymerase for PCR were from New England Biolabs (Ipswich, MA).

3.5.2 Cloning and Overexpression

The pT7-SC1 vector was used throughout the cloning procedures [41]. Restriction digests were performed as per the manufacturer's instructions, briefly, 1 μg of purified recombinant plasmid (prepared by Qiagen Maxi-prep) containing the template DNA sequences were digested in two separate reactions. The first with EcoNI and SapI, the second with BlpI and HindIII overnight at 37°C. 20 μL PCR reactions were set up containing 4 μL (5×) Phusion High-Fidelity buffer, 0.4 μL 10 mM dNTPs, 2× 5 μL 1 μM sense and antisense primers, 5 μL of the digested template, 0.4 μL DMSO and 0.2 μL Phusion polymerase. PCR conditions for both mutants were identical and were as follows:

	98°C	1 min	
Melt	98°C	30 s	
Anneal	57°C	30 s	× *30 cycles*
Extend	72°C	2 min	
	72°C	10 min	
	4°C	∞	

Table 3.1: *PCR reaction parameters*

PCR products were verified by 0.8 % agarose gel electrophoresis prior to transformation of ultra-competent XL10g *E. coli* for plasmid amplification. Plasmids were purified (Qiagen

Mini-prep) and sequenced by dideoxy chain-termination Sanger sequencing. Following selection of successfully mutated genes, the plasmids were Maxi-prepped and resequenced prior to overexpression experiments.

E. coli strains used in the overexpression trials and their respective genotypes are given below:

JM109(DE3) : *end*A1, *rec*A1, *gyr*A96, *thi*, *hsd*R17 (r_k-, m_k+), *rel*A1, *sup*E44, λ-, Δ(*lac-pro*AB), [F', *tra*D36, *pro*AB, *lac*IqZΔM15], lDE3

BL21(DE3)pLysS : F-, ompT, *hsd*S_B (r_B-, m_B-), *dcm*, *gal*, λ(DE3), pLysS, Cam^r

BL21 Rosetta(DE3)pLysS : F-, ompT, *hsd*S_B (r_B-, m_B-), *dcm*, *gal*, λ(DE3), pLysSRARE, Cam^r

All three strains are lysogenic for λ-DE3 [252], which contains the T7 bacteriophage gene I, encoding T7 RNA polymerase [58] under the control of the *lac* UV5 promoter.

Overexpression was performed in LB in 500 mL volumes. Bacterial culture growth was monitored at all times by optical density measurement at 600 nm (OD_{600}). Induction with IPTG was performed by addition of 1 mM [final] to the cultures during log-phase growth between the OD_{600} values of 0.5-0.8. After induction cultures were continued for another 3 hours. Cultures were pelleted at 3500 $\times$ g and the supernatents were discarded. Cell pellets were resuspended on ice in the following buffer, 1.0% (v:v) Triton X-100, 50 mM TRIS-HCl, 150 mM NaCl, 1 unit Protease Inhibitor Cocktail I (Novagen) at pH 8.0. Thereafter the sample was sonicated on ice six times for 30 s. The cell debris was pelleted at 3500 $\times$ g and the supernatents were filtered through 0.2 μm cellulose acetate filters (Nalgene) and kept for no longer than 1 hour prior to purification at 4°C.

3.5.3 IMAC

The recovered cytosolic constituents from the bacterial resuspension and lysis were purified by immobilised metal-affinity chromatography using a Ni^{2+}:NTA column (HiTrap Chelating HP, GE) with an Äkta Purifier FPLC system (GE). Briefly, the samples would be loaded onto the column using a Superloop. The binding buffer consisted of degassed 50 mM TRIS-HCl, 0.5 M NaCl and 10 mM imidazole at pH 8.0. The elution buffer (mixed in a constant-gradient elution) contained degassed 50 mM TRIS-HCl, 0.5 M NaCl and 0.5 M imidazole at

pH 8.0. The hemolytic fraction was selected for the next stage of the procedures as described below.

3.5.4 Hemolytic Assays

Hemolytic assays were performed as described previously [139]. Briefly, a microtitre plate had all wells filled with 50 μL of buffer, 10 mM MOPS, 150 mM NaCl, 1 mg mL^{-1} BSA titrated to pH 7.4 with NaOH (MBSA), apart from the first well where 5 μL of protein sample was diluted into 95 μL of buffer and the final well which was left empty. The proteins were then serially 2-fold diluted across the plate in each consecutive well. Whole rabbit blood in EDTA (mixed sex, Harlon Scientific, U.K.) was washed repeatedly with MBSA resulting in a 1% suspension. This was rapidly pipetted into the wells starting from the most dilute side to begin hemolysis. The progress of hemolysis was followed every 30 s by a measurement of the optical density (light scattering) at 595 nm using a Bio-Rad microtitre plate read (Model 3550-UV) [40].

3.5.5 Disulphide Bond Reduction and Gel Filtration

Following IMAC the protein is present in TRIS buffer and approximately 0.5 M imidazole, 0.5 M NaCl as judged by the elution peak position versus elution buffer concentration gradient. The protein must be desalted prior to separation from dye on a cation exchange resin, hence the most logical time to do this is immediately after IMAC and disulphide bond reduction. The reducing agents β-ME, β-cysteamine, TCEP and DTT were all trialled. Protein samples from IMAC were incubated on ice with 1 mM reducing agents for 1 hour prior to gel filtration/desalting. Desalting the samples was performed in degassed 20 mM TRIS-HCl buffer containing 1 mM EDTA at pH 8.0 at a flow rate of 0.5 mL min^{-1} on a Tricorn Superdex 200 10/300 GL column (GE) in batches. Batches were immediately labelled following elution from the column.

3.5.6 Labelling and Cation Exchange

Labelling was carried out by addition of 10× molar excess of Cy3B-maleimide dye (GE) dissolved in DMF, followed by mixing in darkness and reaction at room temperature for 15 minutes. Thereafter 50-fold excess (v:v) cation exchange resin binding buffer was added

to quench the reaction. Cation exchange binding buffer, 10 mM MES at pH 5.5 was used during binding and washing, free dye did not bind to the column under these conditions (HiTrap SPFF, GE). Protein was eluted using a NaCl gradient up to 1 M in 10 mM MES at pH 5.5.

3.5.7 Bulk Characterization

Labelled protein was characterized by hemolytic assay versus an equivalent amount of unlabelled wild-type protein produced from the supernatant of a *Staphylococcus aureus* Wood Strain 46 culture. Protein purity was verified by SDS-PAGE prior to quantitation by UV-Vis and Bradford assay, using BSA for calibration as described previously [30].

RP-HPLC was performed using a Prostar LC system (Varian, U.K.) using a μRPC C2:C18 ST 4.6/100 reverse-phase column. Protein was bound to the hydrophobic interaction matrix using 99.9% (v:v) MQ water and 0.1% (v:v) formic acid, and eluted using a gradient (as shown in text) of 90% (v:v) AcN, 9.9% (v:v) MQ water and 0.1% (v:v) formic acid. The instantaneous spectrum taken by a PDA detector upon elution of the protein peak was used for quantitation of stoichiometry of labelling, as described in the text.

Mass spectrometry was performed using a Synapt ESI–Q-TOF (Waters) mass spectrometer using a Nanomate ESI chip system (Advion) for positive-mode ionisation. The system was calibrated using a horse-heart myoglobin standard. The recovered protein mass spectrum was deconvoluted using a maximum entropy method using Waters' software, yielding a single principal peak as stated in the text.

3.5.8 Heptamer Labelling

As is the case with overexpressed monomer recovery from bacterial cytosol, the same buffer is used for bacterial resuspension with 1% SDS (w:v) added to 1.0% (v:v) Triton X-100, 50 mM TRIS-HCl, 150 mM NaCl, 1 unit Protease Inhibitor Cocktail I (Novagen) at pH 8.0. The majority of protein precipitates and was removed by repeated centrifugation and retention of supernatant at 20,000 $\times$ g. The sample was filtered through a 0.2 μm cellulose acetate filter (Nalgene) and kept for no longer than 1 hour prior to purification at 4°C. Purification and labelling were carried out as described in the text using an identical buffer to that described for monomer IMAC however also containing 0.1% (w:v) SDS. Cy3B-maleimide dye was added to the column for labelling at 1 μM concentration in binding buffer diluted

from a stock in DMF. Protein labelling was analysed by SDS-PAGE as described in the text. Protein was frozen at -80°C for storage.

3.5.9 Protein Storage

Following labelling and bulk characterization, the labelled α-hemolysin monomer was stored in the cation exchange elution buffer at +4°C.

Chapter 4

Protein and Lipid Diffusion in Droplet-on-Hydrogel Bilayers

Abstract

The fluid properties of Droplet-on-Hydrogel Bilayers are investigated by single-particle tracking. Fluorescently labelled lipids and protein are incorporated into DHBs and imaged using TIRF microscopy. The diffusion of individual lipids and the pore-forming toxin α-hemolysin in DHBs is studied using a novel single-particle tracking algorithm derived from an astronomical point-spread function detection process.

4.1 Introduction

The text of this chapter cannot currently be made available via ORA. Only the section headings and figures are available in this PDF. The content of the chapter has been published as: Thompson, J. R., Heron, A. J., Santoso, Y., and Wallace, M. I. (2007). 'Enhanced stability and fluidity in droplet on hydrogel bilayers for measuring protein diffusion', Nano Lett. 7(12), 3875-3878.
[Available at http://dx.doi.org/10.1021/nl071943y].

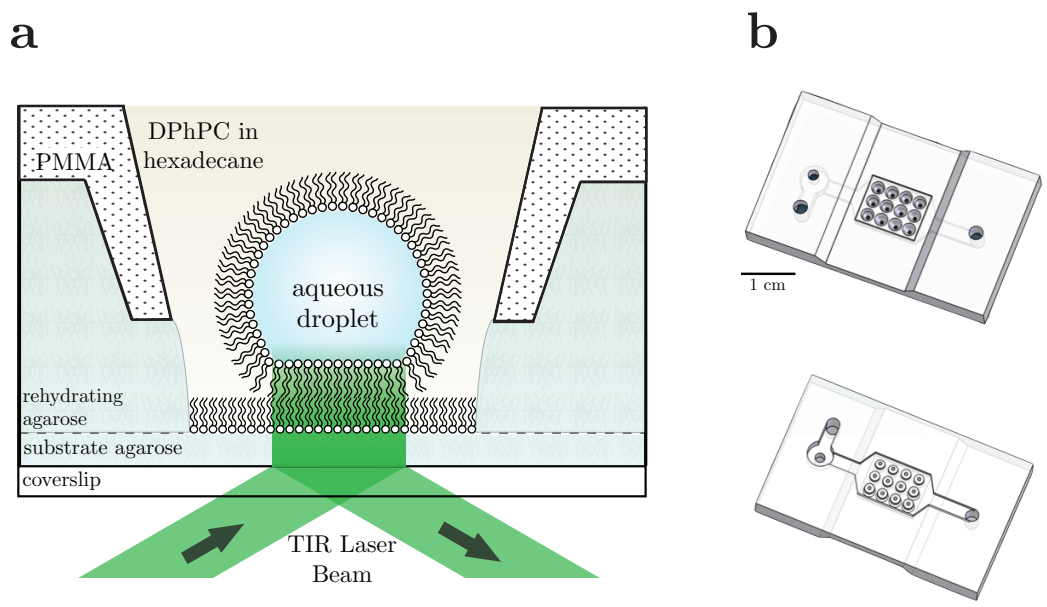

Figure 4.1: *A schematic diagram of TIRF microscopy on DHBs: (A) A supporting substrate comprised of a thin layer of agarose is formed on a glass coverslip. This thin substrate film is rehydrated by filling a PMMA micro-channel device (B) with aqueous agarose. The device wells are filled with a solution of lipid in oil. An aqueous droplet (approximately 50 nL in volume) is placed on top of the hydrogel underneath the oil. A lipid bilayer (approximately 200 µm in diameter) forms at the interface between the two aqueous phases. The evanescent wave propagates through the thin hydrogel supporting substrate into the DHB illuminating the lipid bilayer and fluorophore-tagged proteins in the droplet.*

4.2 Results

4.2.1 Droplet-on-Hydrogel Bilayer Characterization

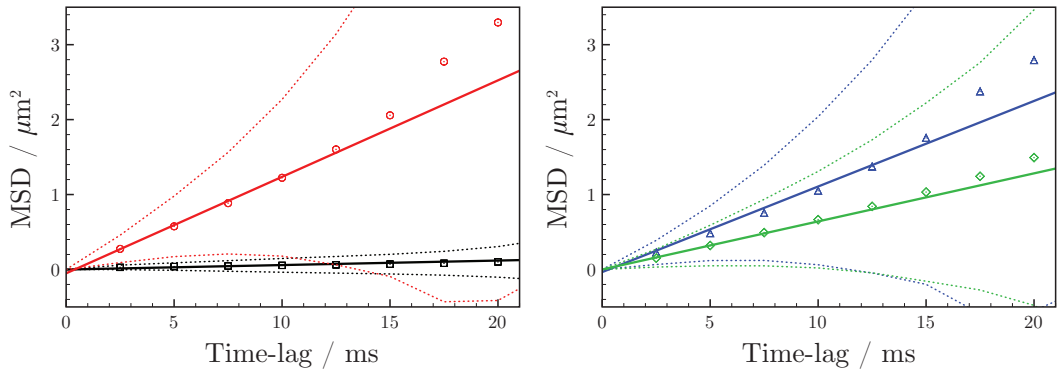

Figure 4.2: *Mean MSD versus time-lag for all experimental data for each diffusing species studied. SLB lipid (black squares) with corresponding weighted linear fit (black solid line) show the slowest lateral diffusion coefficient (D_{lat} = 1.5 ± 0.8 μm^2 s^{-1}). DHB lipid (red circles) with corresponding weighted linear fit (red solid line) show the fastest lateral diffusion coefficient (D_{lat} = 32.2 ± 18.7 μm^2 s^{-1}). α-hemolysin monomers (blue triangles) with corresponding weighted linear fit (blue solid line) show the fastest lateral diffusion coefficient of the two proteins (D_{lat} = 28.5 ± 6.9 μm^2 s^{-1}). Finally, α-hemolysin heptamers (green diamonds) with corresponding weighted linear fit (green solid line) show the slowest lateral diffusion coefficient of the two proteins (D_{lat} = 16.0 ± 6.5 μm^2 s^{-1}). Error is indicated by the corresponding coloured dashed lines indicating the positive and negative magnitude of the reciprocal of the square of the number of independent MSD pairs for each time-lag ($1/N^{-0.5}$).*

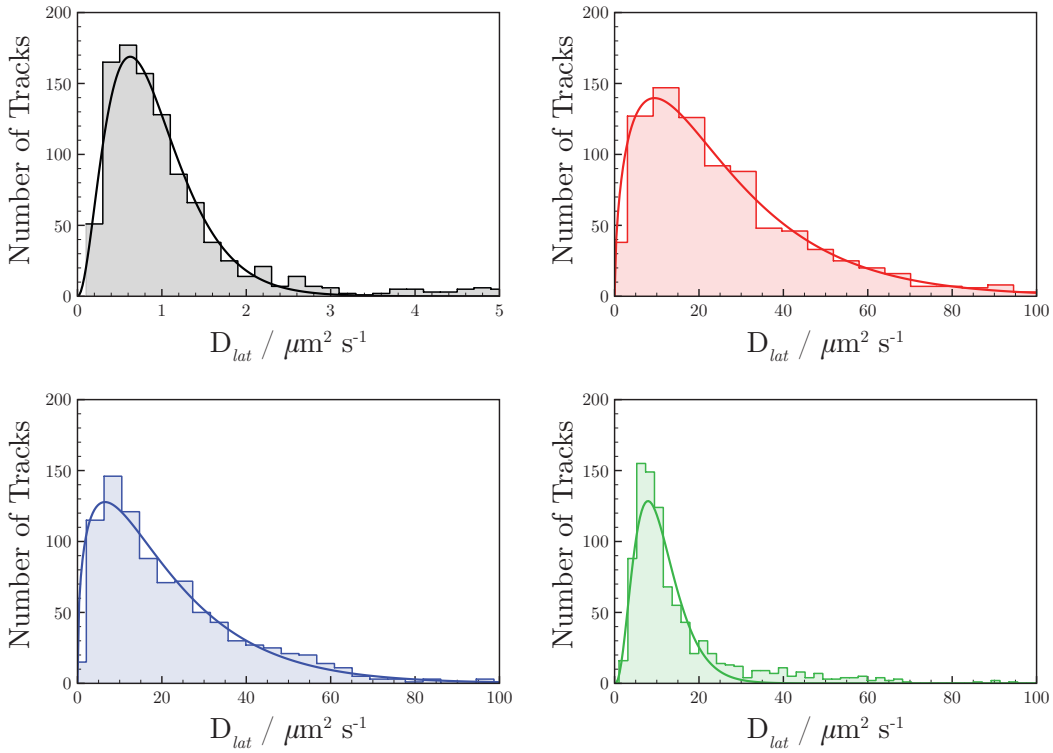

Figure 4.3: *Histograms of individual track lateral diffusion coefficients with fitted probability density functions of the gamma distribution. (Black) SLB lipid* $< D_{lat} > = 0.9\ \mu m^2\ s^{-1}$, $\chi_r^2 = 2.2$. *(Red) DHB lipid* $< D_{lat} > = 26.26\ \mu m^2\ s^{-1}$, $\chi_r^2 = 2.8$. *(Blue) α-hemolysin monomers* $< D_{lat} > = 21.5\ \mu m^2\ s^{-1}$, $\chi_r^2 = 1.49$. *(Green) α-hemolysin heptamers* $< D_{lat} > = 10.8\ \mu m^2\ s^{-1}$, $\chi_r^2 = 4.4$.

Species	Trajectory No.	α_1	$r_1^2/\mu m^2$	$r_2^2/\mu m^2$
SLB Lipid	1050	0.94 ±0.02	0.11 ±0.02	1.78 ±0.65
DHB Lipid	844	0.08 ±0.04	0.94 ±0.65	7.25 ±0.19
αHL_1	894	0.17 ±0.07	1.64 ±1.05	7.15 ±0.3
αHL_7	909	0.78 ±0.16	3.21 ±0.46	8.44 ±2.53

Table 4.1: *Fitting results for probability distributions plotted in Figure 4.4.*

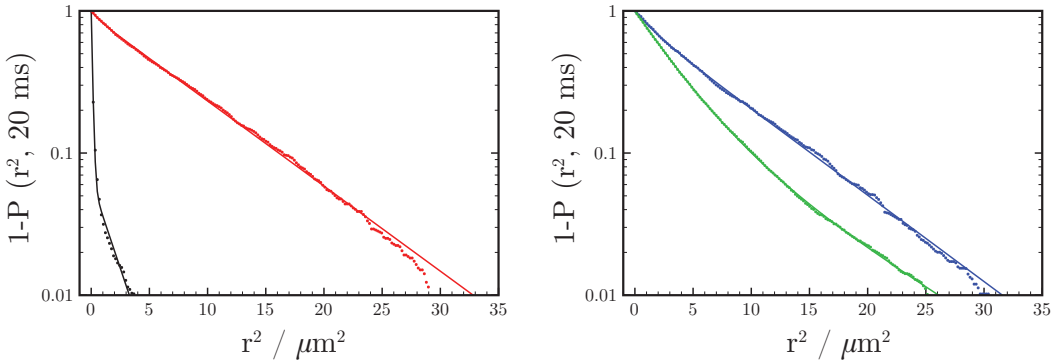

Figure 4.4: *Graphs showing 1 - P vs. r^2, where P is the probability that a particle will be found at a position within an area defined by the radius squared r^2 after 20 ms of diffusion. Only 200 data points over the time course (linear interpolation) are shown for clarity, see Table 4.1 for information on data set sizes. (Black) SLB lipids, (Red) DHB lipids, (Blue) α-hemolysin monomers and (Green) α-hemolysin heptamers.*

4.2.2 α-Hemolysin Analysis

4.3 Discussion

4.4 Conclusions

4.5 Materials and Methods

4.5.1 Materials

4.5.2 Supported Lipid Bilayers

4.5.3 Droplet-on-Hydrogel Bilayers

4.5.4 Protein Preparation

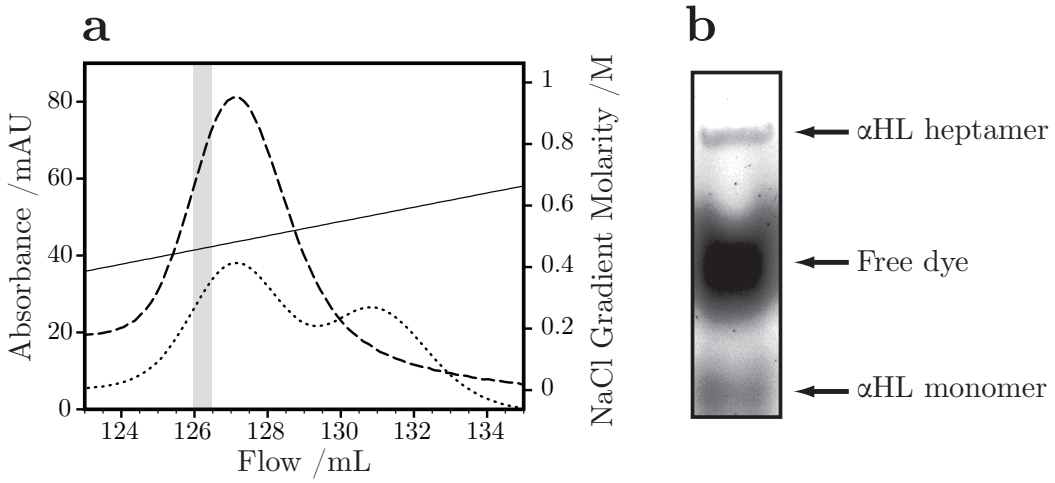

Figure 4.5: *(A) Cation exchange chromatogram showing the elution profile of labelled and unlabelled monomeric α-hemolysin. Absorbance at 280 nm (dotted line), absorbance at 560 nm (dashed line) and the concentration of the eluent NaCl (solid line) are shown on the y axes. The 0.5 mL fraction used in subsequent experiments is shown between as a gray band. (B) Fluorescence image of the SDS-PAGE gel used to separate labelled heptameric α-hemolysin, free dye and non-oligomerized monomeric α-hemolysin.*

4.6 Tracking experiments

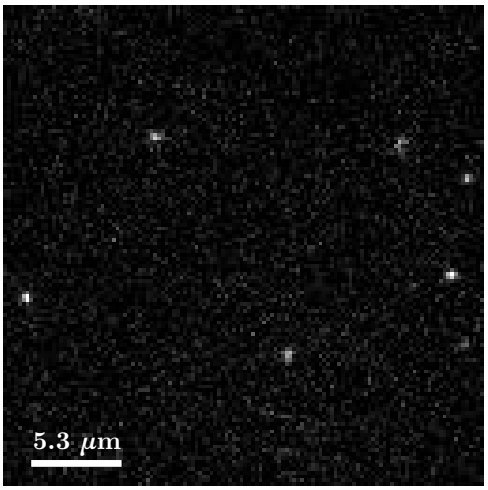

Figure 4.6: *A representative image of fluorescently labelled heptameric α-hemolysin diffusing in a DHB. This raw* 128×128 *pixel image was acquired from a 2.5 ms exposure time and is shown without any filtering or adjustment.*

4.6.1 Fluorophore Tracking Algorithm

4.6.1.1 Initial Image Analysis

4.6.1.2 Spot Detection

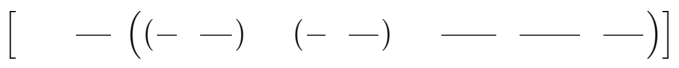

4.6.1.3 Track Reconstruction

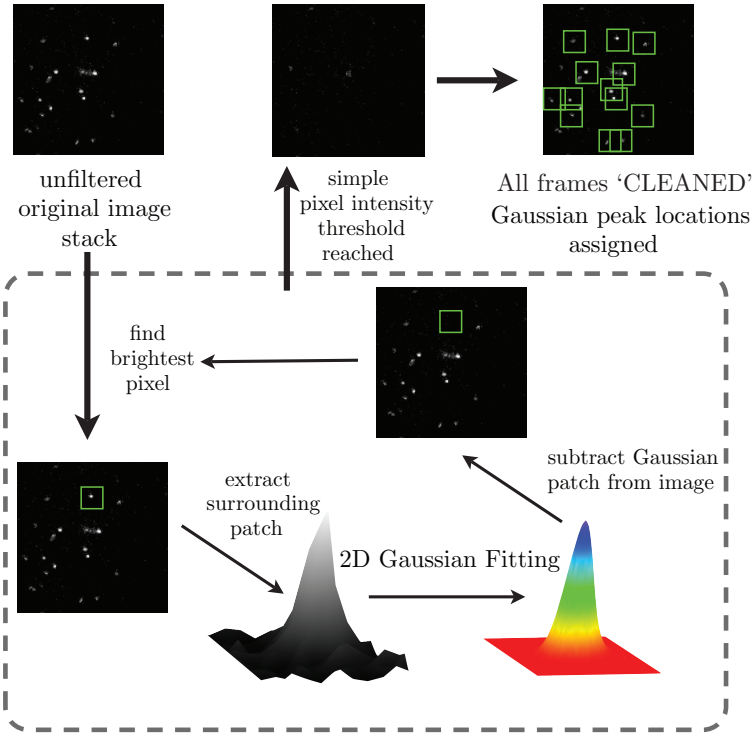

Figure 4.7: *A diagram showing the principles of the CLEAN algorithm.*

4.7 Data Analysis

4.7.1 Lateral Diffusion Coefficient Calculations

4.7.2 Population Multi-Component Analysis

Chapter 5

Simultaneous Fluorescence and Electrical Recording in Droplet-on-Hydrogel Bilayers

Abstract

This chapter describes the imaging of ion current through individual protein pores in DHBs using a calcium-chelating fluorophore. In parallel, simultaneous electrical recording is performed, enabling a simultaneous measurement of ion current through α-hemolysin. The approach is used to deconvolute the electrical measurement of stochastic blocking of multiple α-hemolysin pores in a single lipid bilayer. These experiments demonstrate that DHBs are a suitable platform for simultaneous fluorescence and electrical recording of ion channels *in vitro*.

5.1 Introduction

The text of this chapter cannot currently be made available via ORA. Only the section headings and figures are available in this PDF. The content of the chapter has been published as: Heron, A. J., Thompson, J. R., Cronin, B., Bayley. H. & Wallace, M. I. (2009). 'Simultaneous measurement of ionic current and fluorescence from single protein pores', J. Am. Chem. Soc. 131(5), 1652-1653. [Available at http://dx.doi.org/10.1021/ja808128s].

5.1.1 Optical Patch-Clamping and *In Vitro* Measurements

5.1.2 Experimental Introduction

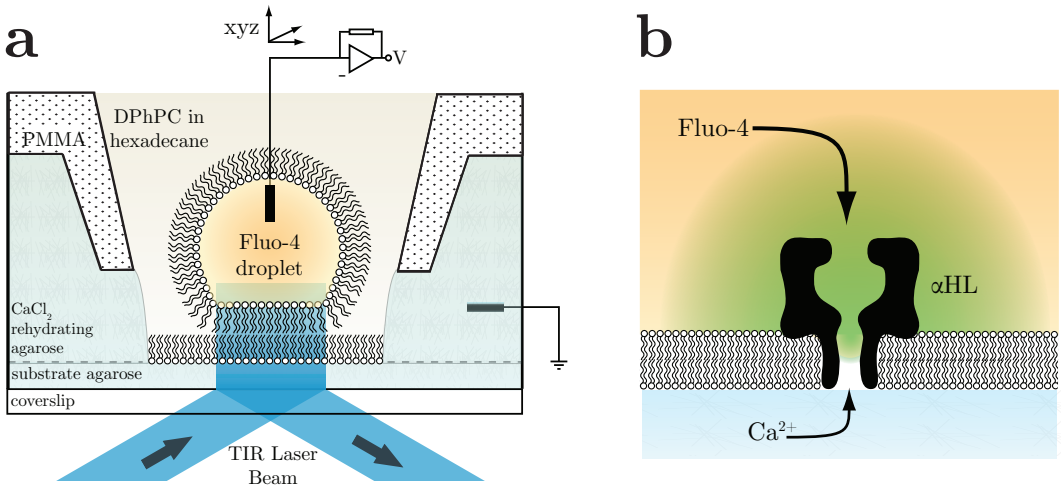

Figure 5.1: *Schematic diagrams of the experiment. (A) A DHB is formed between a 50 nL aqueous droplet and a thin agarose hydrogel containing $CaCl_2$. A totally internally reflected laser beam is used to illuminate the region of bilayer by the evanescent wave propagating through the lower refractive index medium, the hydrogel. (B) Detergent solubilised α-hemolysin inserts spontaneously from the aqueous droplet solution into the lipid bilayer. Ca^{2+} flux through the pore is monitored using the fluorescence from the Ca^{2+} indicator dye Fluo-4 and the current due to the overall ion flux is recorded at the same time under a negative applied potential.*

5.1.3 Calcium Indicator Dyes

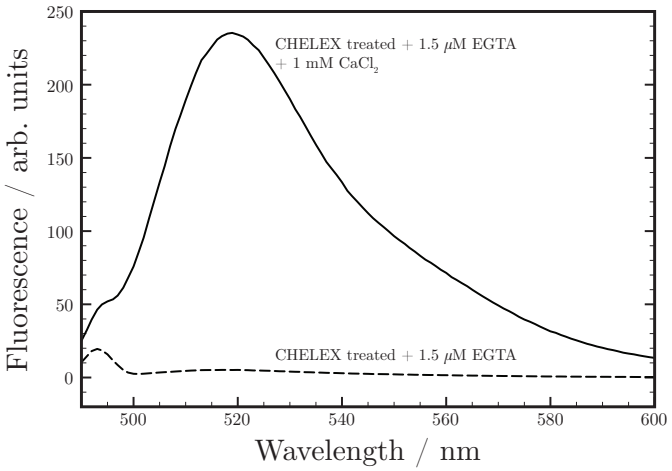

Figure 5.2: *Spectra of Fluo4 after buffer CHELEX (Bio-Rad) treatment. 25 μM Fluo-4 was prepared in 10 mM HEPES buffer, 0.5 M KCl (TraceSelect, Fluka) and 1.5 μM EGTA titrated with KOH to pH 7.0. Spectra were recorded with and without $CaCl_2$ at 1 mM concentration by titration. The fluorescence change upon titration of $CaCl_2$ measured at the fluorescence maximum (517 nm) corresponds to a 45.27-fold increase. Spectra were recorded using an Eclipse Fluorescence Spectrophotometer (Varian), using 10 nm excitation and emission slit widths at a rate of 200 nm scanned per minute at room temperature in a quartz cuvette.*

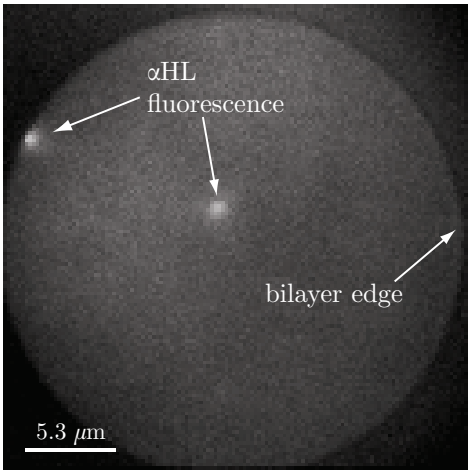

Figure 5.3: *An image of a Fluo-4 and detergent solubilised α-hemolysin-containing DHB. Here two α-hemolysin pores are visualised through the enhanced fluorescence emanating from the vicinity of the pores by Fluo-4 chelation of the Ca^{2+}. Fluo-4 is being electrophoretically driven through the pores under the influence of the applied electric field. The bilayer edge is clearly visible as a ring around the edge of the image, and is optically flat allowing even illumination across its entirety.*

5.2 α-Hemolysin Tracking Experiments

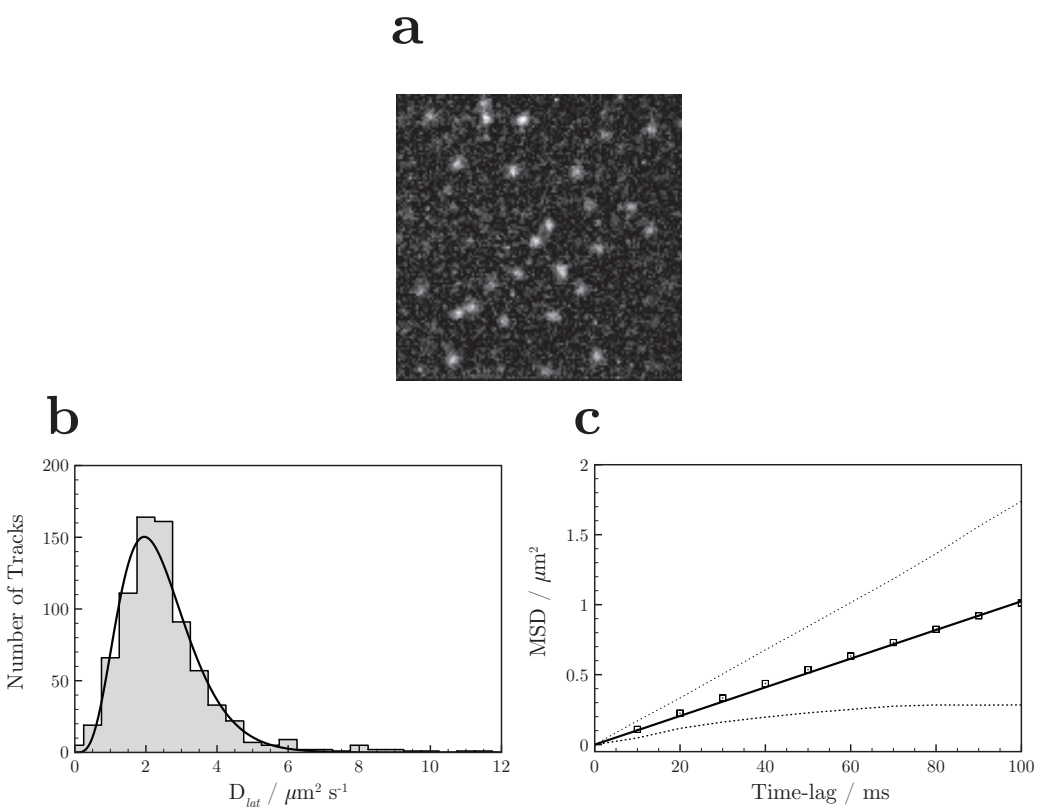

Figure 5.4: *The tracking of α-hemolysin pores in a DHB using Fluo-4 fluorescence. (A) A representative image of Fluo-4 fluorescence emanating from DHB-embedded α-hemolysin pores used in tracking. Pores were tracked using the ETH Single-Particle Tracker, as described in Methods. (B) A histogram showing the individual lateral diffusion coefficients of 766 α-hemolysin heptamer tracks. The mean value of the gamma distribution is 2.4 $\mu m^2\ s^{-1}$ with $\chi_r^2 = 2.1$. (C) The average mean squared displacement versus time of all tracks. The gradient of the linear fit is used to calculate the D_{lat}, yielding a value of 2.6 ± 2.2 $\mu m^2\ s^{-1}$.*

5.3 Parallel Optical Stochastic Detection of Single-Molecules

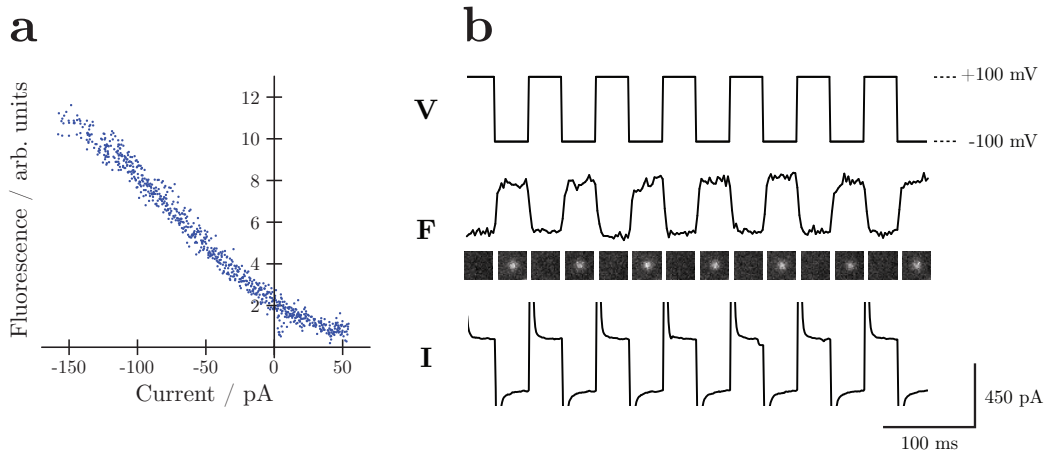

Figure 5.5: *The fluorescence and current response of α-hemolysin to an applied voltage. (A) A voltage sweep response of α-hemolysin pores. The average of five voltage sweeps are shown, between +50 mV and −150 mV (each lasting for 3 seconds) applied to a DHB containing a single α-hemolysin pore. The droplet contained, 10 mM HEPES, 1.5 M KCl, 25 μM Fluo-4, 50 μM EGTA at pH 7.0. The substrate hydrogel contained 10 mM HEPES, 750 mM $CaCl_2$ at pH 7.0. The fluorescence movie was acquired at a rate of 200 Hz. (B) An alternating potential is used to control α-hemolysin pore fluorescence in a DHB. Measured electrical current (I) and fluorescence intensity (F) from α-hemolysin pores in a DHB as a function of an applied voltage (V) across the bilayer is plotted, using the configuration shown in Figure 5.1B. A square-wave alternating voltage (±100 mV, 14 Hz) was applied to a DHB containing 5 pores (10 mM HEPES pH 7.0, 1.5 M KCl, 25 μM Fluo-4, and 50 μM EGTA in droplet; 10 mM HEPES pH 7.0, 750 mM $CaCl_2$ in hydrogel), resulting in a peak to peak current change through all the pores of approximately 450 pA. The fluorescence intensity trace (F) shows the fluorescence of one of the diffusing α-hemolysin pores. Under negative voltage, Ca^{2+} driven through the pore results in an enhanced fluorescence spot. Under positive voltage, Ca^{2+} flux through the pore is reduced, and fluorescence drops to background levels.*

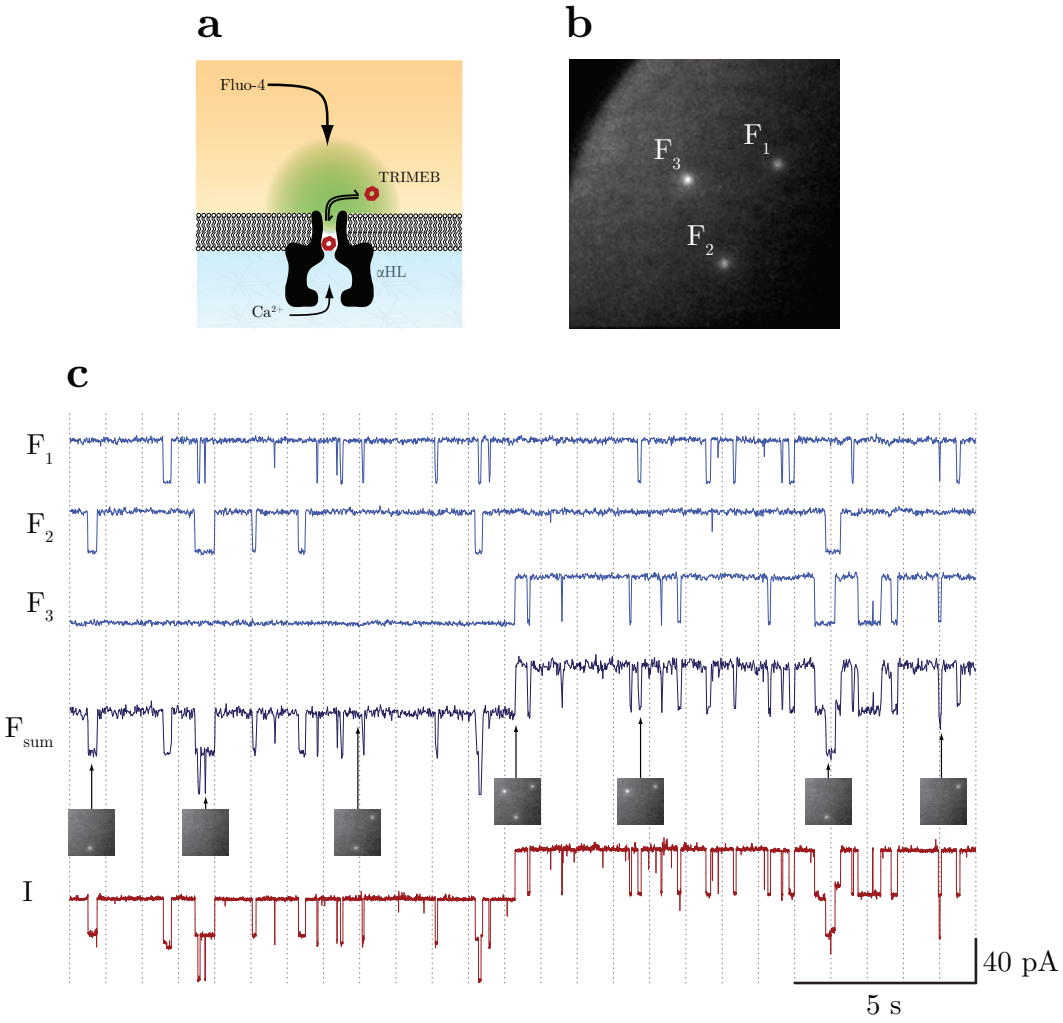

Figure 5.6: *Simultaneous stochastic detection of cyclodextrin blocking α-hemolysin pores (from gel encapsulation). (A) A schematic diagram of the experiment. (B) An image showing Fluo-4 fluorescence from the three α-hemolysin pores in the bilayer (−50 mV; 10 mM HEPES pH 7.0, 1.5 M KCl, 25 μM Fluo-4, 50 μM EGTA and 10 μM hβCD in droplet; 10 mM HEPES pH 7.0, 750 mM $CaCl_2$ in hydrogel). (C) The fluorescence from each pore (F_1, F_2, F_3), the summed fluorescence (F_{SUM}), and the measured ionic current across the bilayer (I) plotted versus time. The individual fluorescence traces show stepwise current changes resulting from hβCD blocks. The summed fluorescence for all three spots (F_{SUM}) correlates with the electrical current (I) through all three α-hemolysin pores, (n.b. the electrical trace is inverted to aid comparison with the fluorescence data).*

5.4 Membrane Protein Concentration in DHBs

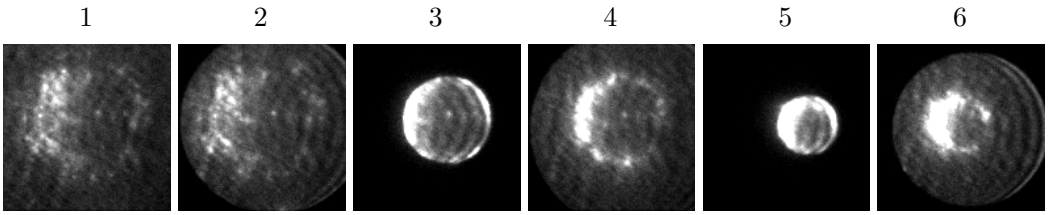

Figure 5.7: *Dynamic manipulation of DHB size affects embedded membrane protein position in the lipid bilayer. A DHB containing many calcium-conducting α-hemolysin pores is manipulated to control the position of the embedded pores. Protein was inserted into the lipid bilayer from the droplet in this experiment. (1) Diffusing α-hemolysin pores are seen roughly centrally in the image. (2) The lipid bilayer size is reduced by raising the height of the embedded electrode. (3) As the lipid bilayer retreats past the position of the embedded pores, they are concentrated along the edge of the lipid bilayer and dragged into the centre. (4) If the lipid bilayer size is expanded again, the protein pores remain conductive in the centre. (5) The process is repeated, however showing a greater degree of concentration. (6) The lipid bilayer is again enlarged, demonstrating concentration of the embedded proteins has ensued. In time the protein pores diffuse away from their concentrated zone.*

5.5 Discussion

5.6 Conclusions

5.7 Materials and Methods

5.7.1 Materials

5.7.2 Protein Preparation

5.7.3 DHB Methods

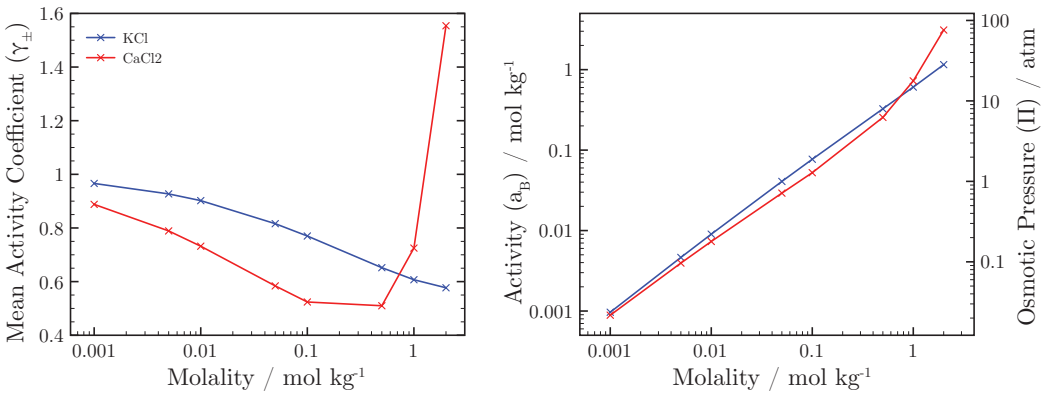

Figure 5.8: *Plots of the experimentally determined mean activity coefficients, reproduced from Atkins and de Paula [9], derived solute activities and solution osmotic pressures of pure KCl and $CaCl_2$ in water at 298 K. The mean activity coefficient ($\gamma\pm$) of solute (B) for given molalities (equivalent to molarity in water) is shown in the left-hand plot [9]. The calculated solute activities (a_B) and osmotic pressures (Π) are shown versus molality in the right-hand plot.*

5.7.4 Electrical Recording

5.7.5 Fluorescence Imaging

Chapter 6

Imaging α-Hemolysin Assembly

Abstract

This chapter describes single-molecule fluorescence measurements of the assembly pathway of the staphylococcal pore-forming toxin α-hemolysin in DHBs. Fluorescently-labelled monomeric α-hemolysin is injected into droplets and tracked during assembly at the lipid bilayer. Also, single-molecule fluorescence and electrical currents are measured simultaneously, allowing for separate measurements of oligomerization and pore insertion. Experiments show that α-hemolysin spontaneously forms long-lived complexes on the lipid bilayer, with intensity many multiples brighter than the monomeric precursor. Through the analysis of the number of photobleaching steps in these complexes it is shown that on average they contain approximately seven subunits. Intermediates are not observed in these experiments, suggesting that the oligomerization of protomers is rapid, and does not proceed by long-lived intermediate encounter complex growth steps.

6.1 Introduction

The heptameric mature state of the staphylococcal pore-forming toxin α-hemolysin was confirmed through a high-resolution X-ray crystal structure in 1996 [249]. This structure was the culmination of a large body of literature published on experiments using purified α-hemolysin reaching back over 30 years [159]. However, the viability of a hexameric state of α-hemolysin in lipid bilayers has been demonstrated and as such its existence cannot be ruled out [55, 57, 70, 76, 177]. In order to study the stoichiometry of the mature pore,

a single-molecule measurement of pores oligomerized in the lipid bilayer is preferable, as opposed to those oligomerized using a detergent. It is feasible that strong detergents, such as SDS or deoxycholate, could catalyse the dispersion of a hexameric complex due to its weaker thermodynamic stability [55, 268]. A single-molecule fluorescence measurement in parallel to lipid bilayer electrical recording may be capable of resolving not only the subunit stoichiometry of functional pores, but also how they assemble. Single-molecule resolution of the assembly pathway is the goal of the experiments described in this chapter. α-Hemolysin monomers bind to natural and artificial lipid bilayers to self-assemble into eventual water-filled trans-membrane β-barrel pores [249]. It is this spontaneous insertion into the lipid bilayer from a water-soluble form that makes α-hemolysin an excellent target for the study of the folding of β-barrels in lipid bilayers. Information garnered from these experiments, and the techniques developed to facilitate them, may enable a greater understanding of multimeric membrane protein assembly and general membrane protein folding.

6.1.1 A Summary of Hypothetical Models of Assembly

Biochemical experiments since the advent of molecular cloning have yielded a wealth of information regarding the apparent redundancy of much of α-hemolysin's primary sequence. It has been shown that the majority of the protein is able to tolerate severe mutations, in addition to significant domain alterations [11, 15, 40, 41, 143, 283, 288]. Fortuitously, this has enabled many powerful reverse genetics experiments to be performed, probing the nature of the interactions between the monomeric protomer subunits during oligomerization. A brief review of the overall process of assembly is now made, prior to an in depth discussion of the published experimental information regarding the separate stages of the assembly pathway.

Currently, the assembly pathway is thought to consist of several sequential stages [16]. The binding of α-hemolysin to lipid bilayers can be considered as being resolutely proven. The relative rates of binding and dissociation of monomeric protomers from lipid bilayers has however not been addressed previously. The eventual spontaneous conversion of the membrane-bound monomeric protomers into ring-shaped multimeric oligomers (number of subunits >6), termed a prepore, which then create a β-barrel pore that traverses the lipid bilayer is also well demonstrated in the literature. However, the intermediate processes of protomer interaction and oligomerization on the lipid bilayer are the worst characterized sections of the pathway. To summarise these processes a diagrammatic representation of the

assembly pathway is shown (Figure 6.1).

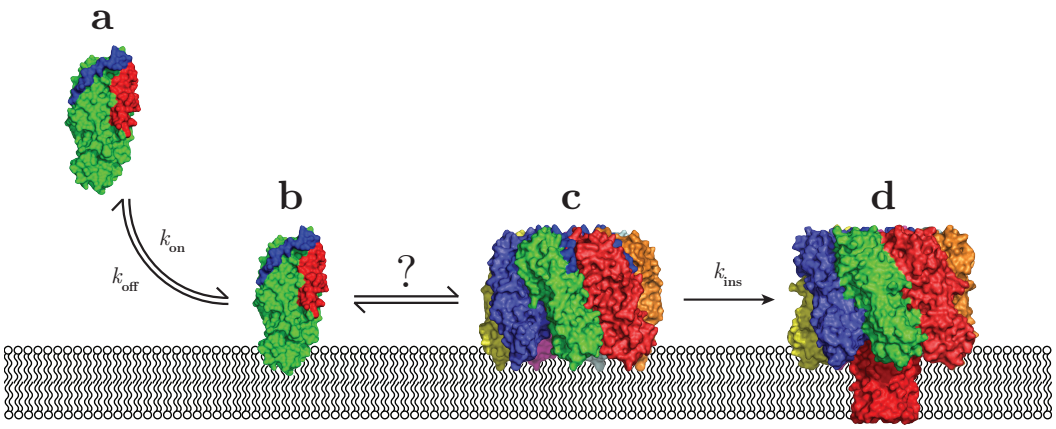

Figure 6.1: *The current interpretation of the assembly pathway of α-hemolysin. Dark blue domain = N-terminus, Red domain = central loop stem-domain. (A) The water-soluble α-hemolysin monomeric protomer (illustrated by the LukF structural analogue (PDB code 1lkf)) binds to phosphocholine-containing lipid bilayers with as yet uncharacterized binding (k_{on}) and dissociation (k_{off}) rate constants. (B) Once the monomer is bound, it diffuses in the plane of the bilayer at roughly the rate of the characteristic lipid lateral diffusion coefficient (in artificial lipid bilayers). Whilst adsorbed to the lipid bilayer the monomers do not penetrate their central loop stem-domain into the lipid bilayer, but are protected from proteolysis. If the solution concentration of monomer is sufficiently high, membrane inter-monomer contacts occur and oligomerization ensues. The nature and kinetics of diffusing inter-monomer contacts is not understood. (C) If seven or greater monomers are in contact an intermediate termed a prepore is thought to exist. The structure of the prepore is unknown, here it is represented by a simulation trajectory derived from the alignment of 7× LukF monomers (PDB code lkf1) with the α-hemolysin heptamer structure (PDB code 7ahl) as a template. (D) Upon establishment of the prepore, the irreversible spontaneous insertion of the β-hairpin glycine-rich central loop stem-domain from each protomeric subunit occurs across the lipid bilayer to form an amphipathic β-barrel. The rate of conversion between prepore and pore (k_{ins}) is not characterized in the wild-type protein.*

Little is known about the concentration dependence of the water-soluble monomeric protomer on oligomerization and actual pore-formation rates. It has proven difficult to assess pore-formation rates *in vitro* by electrical recording due to difficulties in calibrating lipid bilayer sizes. Menestrina and co-workers have attempted to address this problem, and reported a power dependence on the monomer concentration in solution on the maximum pore insertion rate. However, these experiments were unable to deduce the molecularity of the process [17].

The nature of the interactions of the monomers whilst membrane-adsorbed has been considered theoretically previously [16]. Several possible mechanisms for pore formation have been suggested in the literature, some of which are summarised here (Figure 6.2). Potentially, the diffusing monomeric protomers could add together step-wise to form long-lived complexes which persist until 7 or more subunits are appended. Alternatively long-lived

dimer or trimer complexes could interact with one another randomly to form sufficiently large complexes for cyclisation and prepore formation. Also, it is possible that no long-lived complexes form at all. Spontaneous prepore formation may perhaps only occur if there is a sufficient quantity of monomers in contact within a short space in time. This is by no means an exhaustive list of potential mechanisms. Upon formation of the prepore, the insertion of the β-barrel must involve the dispersal of lipids, however this action is entirely uncharacterized.

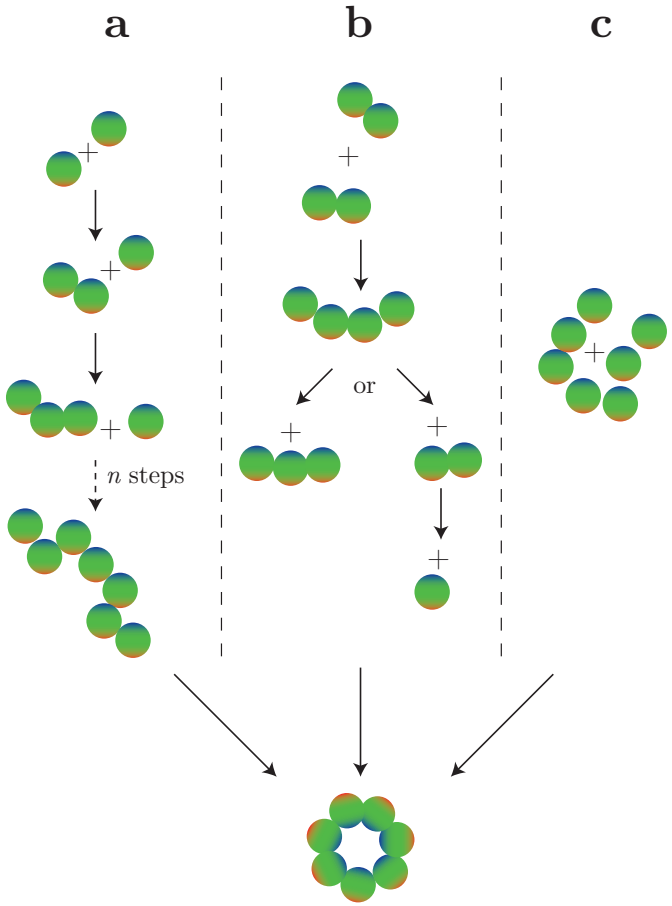

Figure 6.2: *Hypothetical modes of assembly of α-hemolysin. Monomeric α-hemolysin protomers bind to and diffuse upon a lipid bilayer. (A) Upon contact between two membrane-adsorbed monomers, they bind to one another in an unknown fashion. Correspondingly, other monomers bind to the nascent chain, which persists, repeatedly until 7 or more protomers are in contact, resulting in cyclisation to form a prepore. (B) Short chains of monomers could form which could comprise of 2 or 3 monomers, which then interact with other short chains to form complexes large enough to form a prepore. Monomers could also attach to short chains. Critically these short chains would not persist for a great length of time. (C) Hypothetically, it is possible that no long-lived chains of any length form. Seven or more protomers must be present in close proximity for a rapid oligomerization process to ensue, resulting in an encounter complex with enough protomers present to form a prepore.*

The only feasible means to study these interactions is through a single-molecule approach, capable of unequivocal resolution of the stoichiometry of encounter complexes. To date the only studies on a similar process have been performed using the α-hemolysin analogue γ-hemolysin. Higuchi and coworkers used tethered erythrocyte ghosts to attempt to probe the nature of the interprotomer interactions along the γ-hemolysin assembly pathway, using single-molecule fluorescence resonance energy transfer (smFRET) [200]. The bi-component pore forms on human erythrocytes through the oligomerization of the LukF and HS protomers, with an unknown stoichiometry. Separate side-directed mutations to introduce reactive cysteines on the top of the cap domains were made on each protomer gene. Thereafter, selective labelling with a FRET-donor on LukF and a FRET-acceptor on HS was performed, resulting in no measurable alteration in hemolytic activity against human erythrocytes. Dual-colour TIRFm imaging experiments were performed; monitoring both the donor fluorescence and acceptor fluorescence using tethered erythrocyte ghosts. Higuchi and coworkers interpret results as showing punctate spots when both labelled LukF and HS are incubated with the erythrocyte ghosts at picomolar concentrations. However, in my opinion histograms showing a wide range of energy transfer efficiencies in multiple spots are potentially misinterpreted as corresponding to various dimer, trimer, tetramer and mature pore states of the toxin. At higher protein concentrations, a well-sampled roughly log-normal distribution for complex intensities is observed. The authors attribute this as being separated mature pores and clusters of pores. Sample images from this set of data show clearly punctate fluorescence spots well-resolved above the background, however no lower intensity spots are seen as would be expected from dimers, trimers or tetramers. The authors propose an assembly pathway consisting of dimerisation of LukF and HS monomers. These dimers are then interpreted as going on to encounter others, forming tetramers, eventually producing hexameric pores. Whilst the interpretation of the data by Higuchi and coworkers is poorly corroborated, their results do show that interactions occur forming long-lived bi-component γ-hemolysin complexes on human erythrocyte ghosts, paving the way for similar single-molecule experiments to be performed on analogous systems. Direct functional measurements whilst monitoring the assembly of such pores would enable unequivocal designation of complexes as either intermediates or mature pores.

Evidence in the literature for the separate stages of the assembly pathway is now reviewed in detail, preceding introductory details of the experiments performed in this work.

6.1.2 α-Hemolysin Protomers Bind to Phosphocholine Lipid Monolayers and Diffuse Laterally

Biochemical and biophysical evidence for α-hemolysin binding to phosphocholine-containing lipid bilayers dates back to the late 1960s. High-quality electron micrographs clearly demonstrate α-hemolysin oligomers forming on artificial phosphocholine lipid membranes as early as 1968 [73]. Whilst at this time in the literature, it had been shown that it was possible to isolate and purify the α-hemolysin monomer and oligomer, there was little consensus as to the mode of action of the toxin [5, 73]. Further compelling evidence that the protein would oligomerize in the presence of lipid was published in the following years [6, 33, 35, 47, 78, 135–137]. Whilst it was known that lesions would form roughly 10 nm in diameter and with vaguely six-fold symmetry in lipid films from electron microscopic (EM) evidence as early as 1968 [73], evidence that the monomeric protein would oligomerize to form an irreversibly open ion channel was not definitively acquired until 1986 [182]. These early Montal-Müller bilayer electrical recordings paved the way for the modern day understanding of the mode of action of α-hemolysin [17, 182, 261, 268].

Biochemical evidence has shown that at this stage the membrane-diffusing monomer central loop stem-domain becomes proteolytically insensitive prior to oligomerization [288]. Comparisons of the rate of diffusion of monomeric and heptameric α-hemolysin allowed for a crude estimation of the level of penetration of the monomer into the lipid bilayer in Chapter 4. The characteristic diffusional rate was found to be similar to that of the lipids in the bilayer, indicating that the degree of lipid bilayer penetration of the monomer was minimal, reinforcing the idea that the monomer diffuses on top of a lipid leaflet prior to oligomerization. The amphipathic central loop stem-domains of individual monomeric protomers can form hydrogen bonds between backbone amides and water molecules along their edges in solution [16]. Burying the central loop stem-domain into the lipid bilayer interior would not be favourable thermodynamically. This information goes some way to adding to the huge body of evidence dismissing hypotheses where the monomer itself is lytic [23, 24, 67, 106]. Little however, is known of the relative orientation of membrane-bound monomers diffusing on the lipid bilayer. It is possible that the preferred orientation is for the phosphocholine binding pocket to be making a direct contact with the lipid bilayer-solvent interface. This hydrophobic interaction between the exposed aromatic residues and

the hydrophobic lipid environment might be responsible for driving the monomer binding to the lipid bilayer.

In both the α-hemolysin heptamer crystal structure [249] and the leukocidin component LukF monomer structure, the rim domain consists of a number of exposed aromatic residues (Figure 6.3A and Figures 1.1 and 3.2). This preponderance for exposed aromatic residues is characteristic of membrane protein domains found around the interface between lipid head-groups and bulk solvent [272]. A phosphocholine lipid was co-crystallized with the LukF monomer and is clearly resolved in the electron density map residing in a rim-domain crevice [190, 204](Figure 6.3). A similar crevice is observed in the analogous position in the α-hemolysin heptamer, which has also been shown to co-crystallise with phosphocholine bound inside [79][1]. The arginine residue forming part of the binding-crevice has been shown to be critical for rabbit erythrocyte binding, oligomerization and hemolysis in experiments which predate the heptamer crystal structure [283].

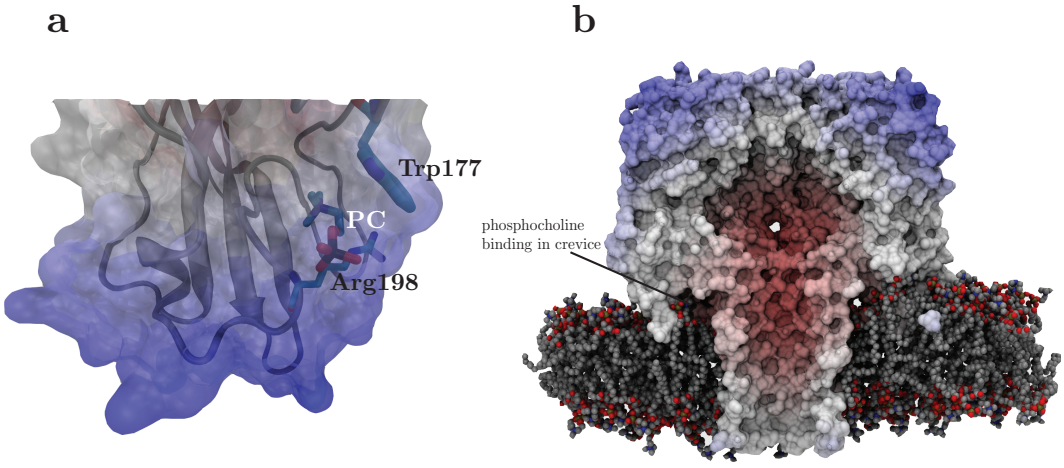

Figure 6.3: *(A) A molecular representation of the phosphocholine moiety of co-crystallized dipropanoyl glycerophosphocholine (DiC_3PC) bound within a cleft in LukF monomer crystal structure (PDB code lkf3). A cleft with edges defined by Trp177 and Arg198 encapsulates phosphocholine in the rim domain of the LukF monomer, analogous with α-hemolysin monomer protomer. The Arg198 interacts through water hydrogen-bonding with the phosphate, whereas the phosphocholine orders the Trp177 residue through cation-π interaction between the indole-ring and quaternary ammonium of choline (by comparison with the absence of lipid (pdb code = lkf1)). (B) Simulated atomistic trajectory of α-hemolysin in a DMPC lipid bilayer (courtesy of Dr. Syma Khalid, University of Southampton). α-hemolysin (pdb code = 7ahl) was placed in a simulated DMPC lipid bilayer and allowed to relax for 10 ns with no restraints on any species inside the established lateral boundary conditions for the lipid bilayer. Figures were rendered using the Tachyon ray tracing engine by John Edward Stone, in VMD [125].*

[1]Structure is not available in the PDB. Resolution is higher than the original oligomer structure (1.75 Å *vs.* 1.9 Å) [249]

6.1.3 The Evidence for a Prepore Intermediate

A model of the conversion between the membrane-bound diffusing monomeric form of α-hemolysin and the oligomer was first described in 1992 [288]. Biochemical evidence based upon truncating the two protein termini and observing the resulting oligomeric states of the protein by gel electrophoresis compared to their hemolytic ability, indicated the presence of a non-lytic oligomer with similar molecular mass to the lytic oligomer [288]. Whilst these data were later found to be in error due to an activity-affecting mutation, which at the time was difficult to detect, the model was put forward for an intermediate oligomeric state existing in the assembly pathway between membrane bound protomer and membrane-penetrating pore. This remains the current interpretation of a range of biochemical evidence. A diagram of the monomeric precursor and mature heptamer is included below to assist the reader in understanding the following experimental evidence 6.4.

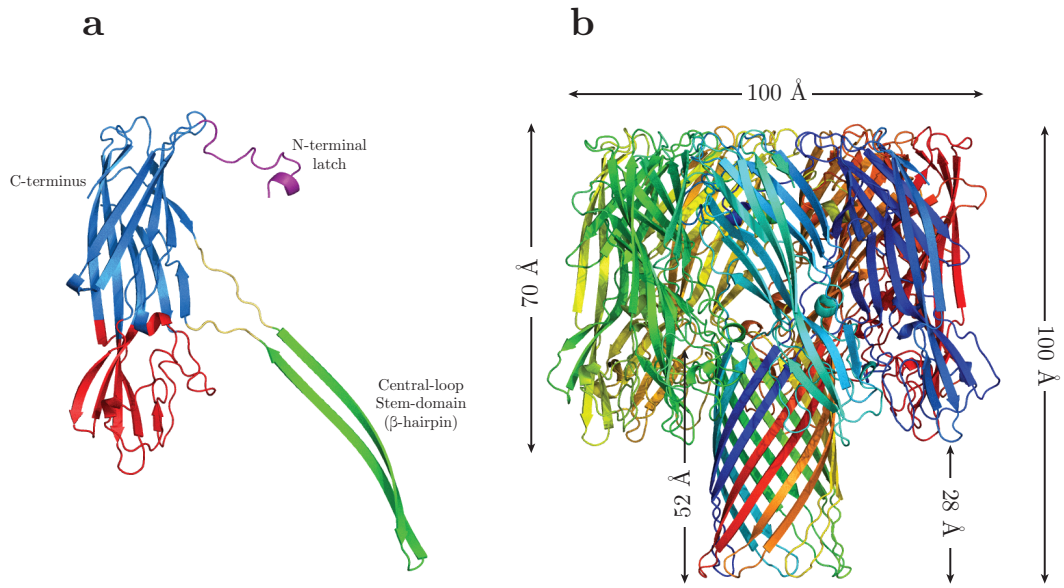

Figure 6.4: *α-Hemolysin representations illustrating the domain architecture and dimensions of the complex (PDB code 7ahl). (A) A protomer subunit from the α-hemolysin heptamer rendered as a cartoon. Here the cap domain is illustrated in blue, the rim-domain in red, the triangle region in yellow, the central loop stem-domain in green and the N-terminal latch in purple. Each protomer subunit in the pore is equivalent. (B) The α-hemolysin heptamer rendered as a cartoon. Here the seven protomer subunits comprising the α-hemolysin pore are illustrated as separate colours. The dimensions of the pore are illustrated by the arrows. The figures were created using PyMol, Delano Scientific, USA.*

The first experiments designed to show the existence of the prepore intermediate used genetic and chemical means to control a conformational rearrangement of the glycine-rich central loop, now known to be the stem-domain [249, 282, 286]. α-Hemolysin mutants

with extra amino acid runs genetically ligated into this central loop were found to have no hemolytic capability, but did form SDS-stable heptamers. When the redundant additional amino acids in the loop were proteolysed, the hemolytic activity is spontaneously regained, in spite of there not being a covalent link between the two halves of the protein [286].

In another class of experiments, chemical control of the central loop stem-domain conformational rearrangement is achieved through targeted protein engineering. A pentahistidine run of amino acids was introduced in place of the wild-type residues at positions 130–134. In the presence of Zn^{2+} in solution, tight oligomers formed exhibiting no hemolytic activity. If EDTA was titrated into the sample to chelate Zn^{2+}, hemolysis ensues after a short lag time, *i.e.* the time required to insert the β-barrel. Further proteolytic evidence from these experiments demonstrated that these oligomers contained occluded central loops, as they were resistant to proteolysis, whereas in solution the monomers are susceptible to proteolysis [268, 288]. These results were confirmed, along with the first biochemical evidence of the heptameric state of the pore in the following year [285]. A crude measurement of the preformed prepore to pore conversion rate was analysed showing a $t_{1/2}$ of $\sim$8 mins upon titration of excess EDTA into Zn^{2+} stalled prepores [285]. A more recent analogous experiment, again pinning back the central loop stem-domain, has been performed through the introduction of an intramolecular disulphide bridge. Upon addition of DTT to reduce the disulphide bridge, oligomers again became hemolytic [151].

More recent experiments have since shown the heptameric state of the prepore through molecular imaging by Atomic Force Microscopy (AFM) [41, 70]. Using both the stalled prepore pentahistidine method [70] and separately using a truncated central loop stem-domain [41].

Other genetic experiments designed to isolate the prepore have been performed without restricting the conformational rearrangement of the central loop stem-domain. For example, mutations including those at His^{35}, located at a critical interprotomer contact in the crystal structure of the heptamer [249] have been shown to be deleterious for pore-forming ability [144, 157, 183, 284]. If this residue is mutated to cysteine, its pore forming ability is severely reduced, whilst not affecting its ability to oligomerize greatly. If the cysteine is subsequently alkylated using an iodoacetamide derivative to yield the unnatural histidine analogue S–carboxamidomethylcysteine (S–CamCys), the non-lytic H35C mutant regains its pore-forming ability. Further fluorescence experiments monitoring oligomerization using

the hydrophobicity-senstive dye acrylodan showed that one such H35 (H35R) [208] mutant undergoes oligomerization but is incapable of causing lysis [276]. Similar experiments using the same acrylodan method have demonstrated oligomer formation without hemolytic ability on resistant cells [275].

At the prepore stage, the N-terminus remains proteolytically-sensitive, whereas the central loop stem-domain is no longer sensitive [285, 288], presumably due to its occlusion from solvent and hence proteases. Pore insertion results in the central loop stem-domain transfer across the lipid bilayer [274] and the subsequent protection of the N-terminus to proteolysis [139, 285]. No prepore→pore intermediates have ever been biochemically isolated, lending to the theory that the process of conversion is a cooperative one [139, 275, 285].

6.1.3.1 Evidence for Prepores in other Pore-Forming Toxins

Hypothetical prepore oligomeric structures have also been observed in other membrane pore proteins [16]. Single-particle EM tomography reconstructions of perfringolysin O, a larger homomeric cholesterol-dependent pore-forming toxin, exhibit two distinct conformations as large ring structures, thought to correspond to prepores and pores [56, 120, 121]. The means to stall the assembly process in this study was similar to that applied for α-hemolysin [151], using a disulphide bridge to pin back the stem domain. In addition, analogous experiments have yielded similar results with βPFT analogues of α-hemolysin such as the staphylococcal leukocidins [181, 199].

In 2005, Tilley *et al.* showed single-particle EM structures of a wild-type CDC (pneumolysin from *Streptococcus pneumoniae*) as a prepore and as a pore [267]. Their images show an intermediate with characteristics similar to that of the stalled prepore mutants of α-hemolysin and leukocidin, such as stable oligomer formation without lytic ability. However their reconstructions show a different number of subunits in the prepore than the reconstructed pore image, leading to questions about their actual identity. It can also therefore be argued that direct observation of a long-lived wild-type pneumolysin prepore is not proven [16].

The only convincing evidence of a kinetically competent wild-type prepore from a βPFT is that of the anthrax protective antigen [161]. The prepore was crystallized and its structure was solved to a resolution of 3.6 Å[161]. Its mode of action differs from that of the leukocidins

in that it is internalized into its target cells whereupon it undergoes a series of concerted events with partner enzymes in order to lyse the cell. Unlike the leukocidins, anthrax protective antigen must bind to receptors on the cellular surface [230]. It is then activated through proteolysis [301]. The protomers can then oligomerize to form a heptameric oligomer which is attributed to be the prepore intermediate [161, 185]. Upon oligomerization, the heptamer can bind to its toxic counterparts, either singly, or both at once [301]. These complexes, containing prepore protective antigen with either lethal factor (protease) or oedema factor (adenylyl cyclase), are then transported to the acidic endosomal compartment. This environment is then responsible for catalysis of pore insertion through the endosomal membrane, whereupon the toxic enzymes are transported through the pore eliciting their toxic activity in the cytosol [301].

This process of acid catalysed pore insertion can be reproduced *in vitro* in model lipid bilayers (painted BLMs) from recovered trypsin-activated protective antigen prepores [150]. In a study by Katayama *et al.*, the chaperonin GroEL was used as a solubility-enhancing molecular scaffold for the protective antigen prepore, circumventing previous handling difficulties with insoluble aggregate formation. This allowed for monitoring of urea catalysed prepore to pore conversion at pH 8.5 through planar lipid bilayer electrical recording. This method of oligomer stabilisation using the chaperonin enabled high-resolution single-particle EM reconstructions of prepores and pores in parallel. This information represents the best evidence for prepore intermediates and their kinetic competence in βPFTs. However, due to the large difference in biological mechanism, its direct comparison with α-hemolysin prepore to pore conversion is restricted.

6.2 Experimental Objectives

Our principal objective is to understand how α-hemolysin monomers interact whilst adsorbed to the lipid bilayer. Through monitoring of the interactions by single-particle tracking, it should be possible to derive the kinetics and pathways of assembly. Specifically, we would like to attempt to identify and characterize any long-lived chains or encounter complexes diffusing on the lipid bilayer. Using DHBs, we are able to make correlated single-molecule fluorescence and single-channel resolution electrical measurements [109]. The subunit stoichiometry of stable complexes can be elucidated through the analysis of fluorophore stoichiometry [57,

165]. If stable complexes are visualised, a simultaneous electrical measurement will enable a temporal comparison of complex formation processes and pore insertion.

Critical to the definite resolution of single-molecules in lipid bilayers both *in vivo* and *in vitro* is the reduction of background noise. Observing homomeric interactions at the single-molecule level at high concentrations with rapidly diffusing fluorescent species is difficult. However, through the application of *in vitro* experimental techniques, signal-to-noise is improved due to lack of an auto-fluorescing background. Planar lipid bilayers can be created in close proximity to a glass coverslip for illumination by a high-intensity evanescent wave. Higher levels of reproducibility of experimental conditions are possible versus *in vivo* experiments. However, at surface concentrations above approximately 1 nM, resolution of single-molecules becomes difficult. Techniques such as photoactivatable localization microscopy (PALM), allow the use of higher concentrations of the molecule under study, alleviating some of the issues surrounding molecular crowding causing difficulties in single-molecule resolution [19, 26]. However, PALM allows for the probing of only a small subset of molecules at any one point in time, and is therefore not suitable for studying processes occuring over an entire lipid bilayer.

As mentioned previously in Chapter 4, monomer lateral diffusion was found to be roughly similar to that of the lipids in DHBs. It is far more difficult to maintain coherent tracks of rapidly diffusing objects at high surface concentrations. However, the main issue is the required illumination intensity being sufficiently high enough, enabling a SNR good enough for single-molecule detection. This in turn increases the photobleaching rate of organic fluorophores employed for imaging. Experimental goals were geared around these considerations.

Droplet injection was used as the principal means of delivering protein to the lipid bilayer; circumventing unwanted oligomerization during the required droplet pre-equilibration time on the lipid monolayer of the droplet, as is known to occur [33]. Typically, a droplet would be pipetted into the TIRFm device, thereafter upon bilayer formation, the required protein stored in a borosilicate capillary would be injected by a piezo-controlled nano-injector (Figure 6.5B and Appendix Figure 8.1), with the injection time recorded. Usually, the volume of injection would be no greater than approximately 10% of that of the droplet. Injection was confirmed by a concurrent swelling of the lipid bilayer area. Upon successful injection, the capillary was carefully removed and replaced by a Ag/AgCl electrode mounted on a micro-

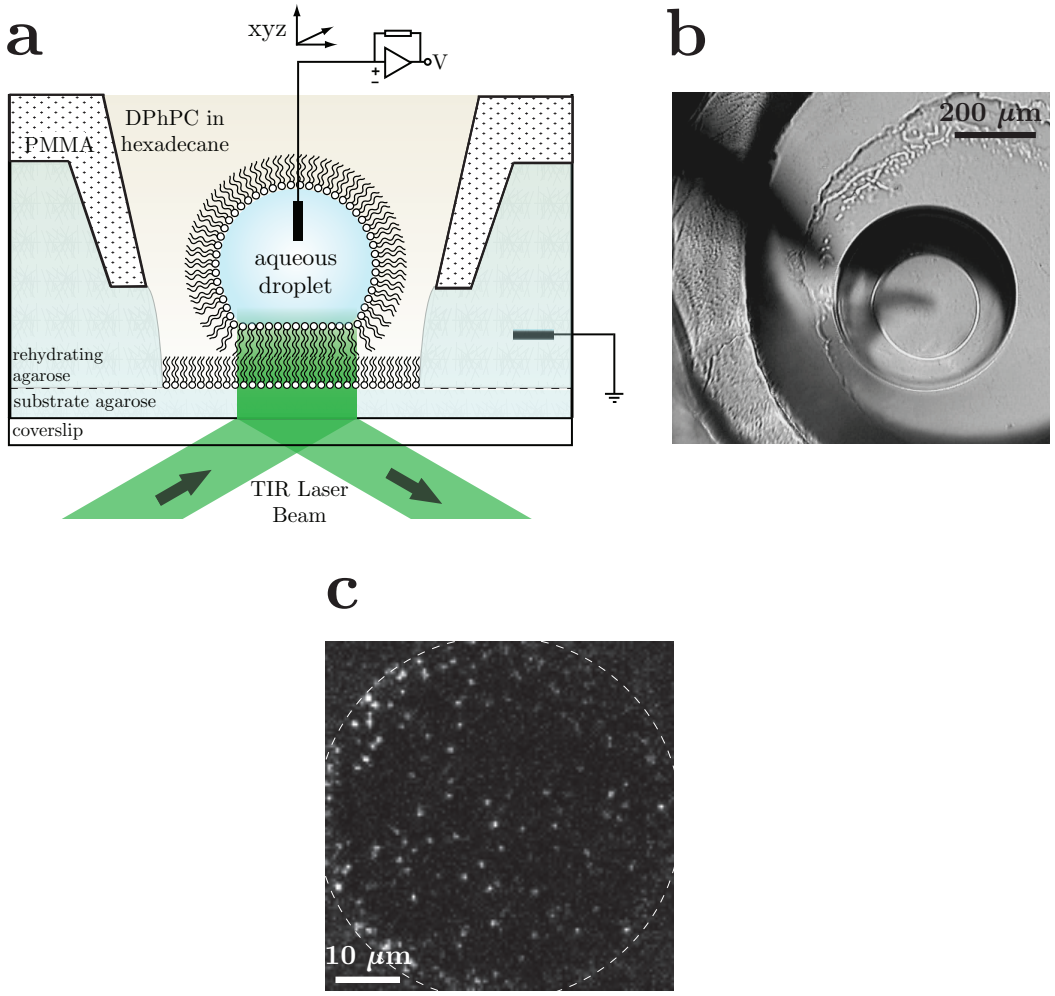

Figure 6.5: *Experimental Introduction. (A) A diagrammatic representation of the simultaneous fluorescence and electrical measurement apparatus around DHBs, as described previously in Chapter 5. (B) A bright-field image of a droplet forming a lipid bilayer (10 × magnification). The shadow from a top-illuminated nano-injection capillary can be seen cast across the droplet, prior to protein injection into the droplet. (C) A typical TIRF image (60 × magnification), showing single Cy3B-labelled α-hemolysin monomers adsorbed to a DHB, frame-rate 10 ms.*

manipulator, as described previously in Chapters 2 and 5. In the monomer binding and dissociation experiments, droplets were created containing the protein at low concentrations and pre-equilibrated for no longer than 15 minutes prior to bilayer formation.

6.3 Results

6.3.1 Initial α-Hemolysin Observations

Low-concentrations of protein were incubated inside the droplets in order to image α-hemolysin binding to the lipid bilayer. The main advantage of using low concentrations is the ability to clearly resolve protomers on the surface of the lipid bilayer, despite their rapid diffusion. However, at concentrations of protein ranging between 50 pM and 1 nM, no oligomerization was observed by single-molecule tracking. In parallel, no concomitant pore formation was observed by electrical recording. At concentrations higher than 1 nM, stable oligomeric α-hemolysin complexes are resolved at the lipid bilayer within a period of a few minutes of injection into a droplet (<20 mins). The EC_{60} (α-hemolysin monomer concentration causing 60% hemolysis) for rabbit erythrocytes at room temperature is 40 pM, a 16,000-fold lower concentration than is required for human erythrocyte lysis [113]. This is postulated to be due to the presence of a specific receptor in rabbit erythrocyte plasma membranes, which is not present in human erythrocytes [278]. With this result in mind, it is reasonable to assume that in a protein-free artificial lipid bilayer the critical concentration for pore formation is likely to be considerably higher than 40 pM.

6.3.1.1 Lipid Bilayer Binding and Dissociation

The process of α-hemolysin binding to the lipid bilayer is treated as a bimolecular process. However, we make the assumption that there are infinite binding sites per unit area of lipid bilayer at low monomer concentrations. The pseudo-first order rate constant for binding (k_b) was calculated through the analysis of the concentration-dependence of the rate of arrival of monomers for a given area of lipid bilayer. Due to the mode of imaging used in these experiments, TIRFm; only fluorescent species at the lipid bilayer will be illuminated, hence monomers out of the bilayer field are not susceptible to photobleaching prior to binding.

Observation of the binding rates was carried out at three different concentrations. The number of binding events per frame throughout the 30 seconds of imaging are shown (Figure 6.6A). The binding rate for the different concentrations is calculated by fitting histograms representing the number of binding events per recorded frame to Gamma-distributions (Figure 6.6B). The mean values of such fits are then plotted versus the concentration of monomeric protomer in solution in the droplet (Figure 6.6C). The binding rate constant

(k_b) is then equal to the gradient of the straight line fit of these rates. This yields a value of 0.36 ± 0.17 nM^{-1} μm^{-2} ms^{-1}. The trend does not go through zero at the axes, probably due to experimental errors, including non-specific adsorption of the protein to the droplet inner interface with the lipid in oil solution, affecting the actual concentration in the droplets. In addition, proteins at such low concentrations are also known to physisorb to microcentrifuge tubes, perhaps altering the concentration present in the droplets after pipetting.

Bound-monomer dissociation kinetics are slightly more complicated to study at the single-molecule level. Because of the use of an organic fluorophore which is susceptible to photobleaching, a direct measurement of the dissociation rate of monomers from the membrane is not possible. Instead, the characteristic rate of disappearance (k_{off}) of a population of tracks on the lipid bilayer is assumed to be the sum of two principal rates: the rate of photobleaching, dependent on illumination intensity (k_{pb}), and the rate of actual monomer dissociation from the lipid bilayer (k_d).

$$k_{off} = k_{pb} + k_d \tag{6.1}$$

If the rate of disappearance of spots in the image is derived for different laser intensities at a fixed concentration of monomers (Figure 6.7A); the first-order rate constant k_d is equal to the extrapolated fit at zero laser intensity, where the rate of photobleaching is nil (Figure 6.7C) [179].

Due to rapid α-hemolysin diffusion in this system and the small imaging area, spots can diffuse out of the field of view without dissociating. However, in single-particle tracking this is manifested as the termination of a track. Therefore in the analysis of this data, a buffer zone was established around the rim of the images (Figure 6.7B). This rim corresponded to 3$\times$ the maximum allowed linkage distance between a tracked position in frame n and $n+1$. Within this buffer zone, if a track appeared or disappeared it was discarded from the analysis population, ensuring that the entire lifetime of the monomers on the lipid bilayer is imaged. The data plotted give a linear fit intercept at the origin yielding the $k_d = 0.053$ ms^{-1}, where the corresponding average lifetime for the monomers on the lipid bilayer is 0.188 ± 0.01 s.

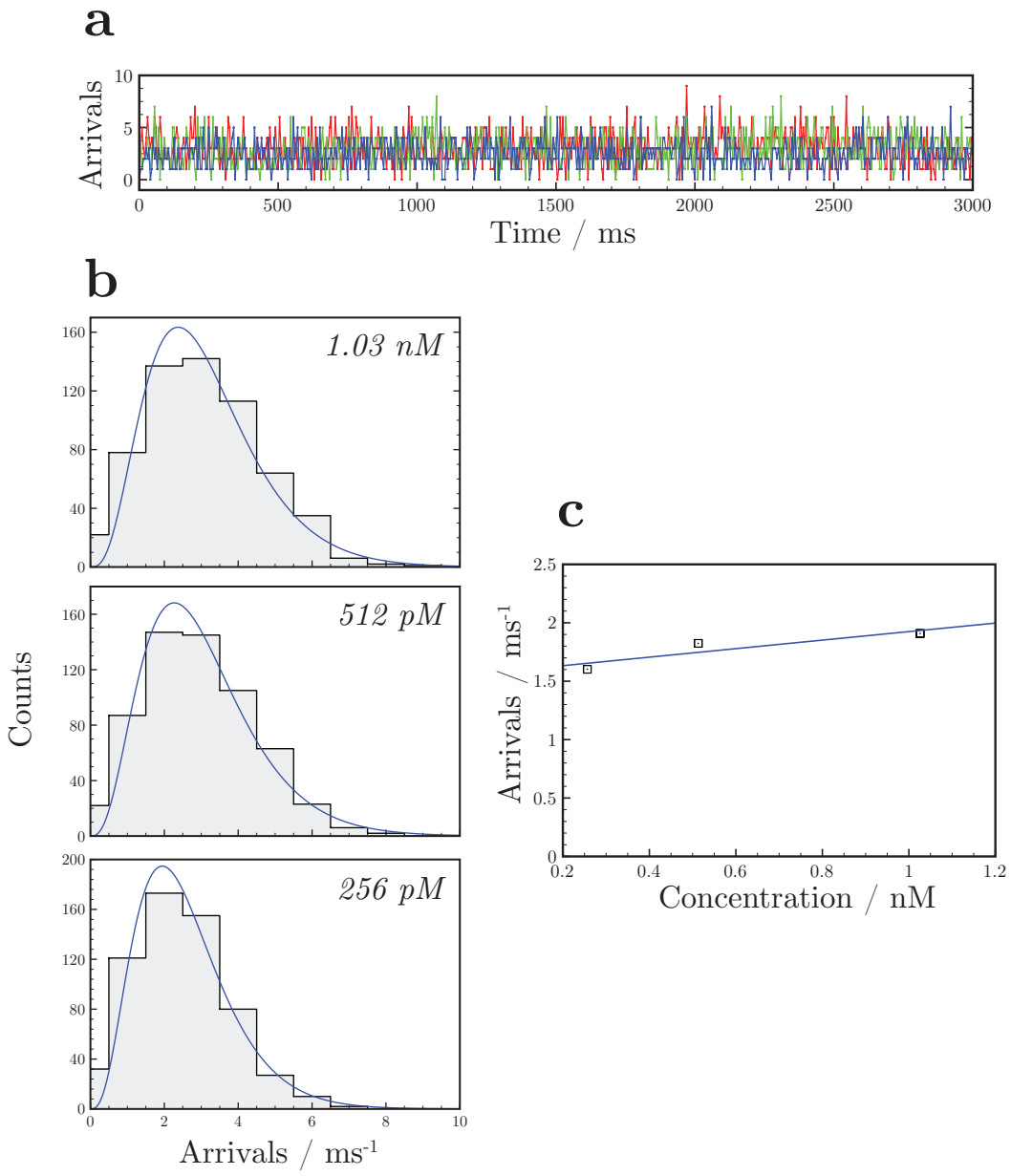

Figure 6.6: *The analysis of monomer binding to the lipid bilayer. (A) A plot showing the number of new fluorescence spots detected for each frame (bin width = 5 ms). The rate of binding is constant for all concentrations throughout the recording due to the excess availability of binding sites for this concentration range of monomer. Red = 1.03 nM, Green = 512 pM, Blue = 256 pM. (B) Histograms of the number of arrivals per frame fitted with gamma distributions. The goodness of fits for the different concentrations are as follows: 1.03 nM* $\chi^2_r = 5.8$*, 512 pM* $\chi^2_r = 4.77$ *and 256 pM* $\chi^2_r = 5.61$*. (C) A plot of the mean values of the gamma distributions as a function of concentration fitted with a linear function. Errors = gamma distribution fitting errors. The gradient of the fit yields a binding rate constant equal to* $0.36 \pm 0.17\ nM^{-1}\ \mu m^{-2}\ ms^{-1}$ *or* $5.39 \pm 2.56 \times 10^{25}\ M^{-1}\ m^{-2}\ s^{-1}$.

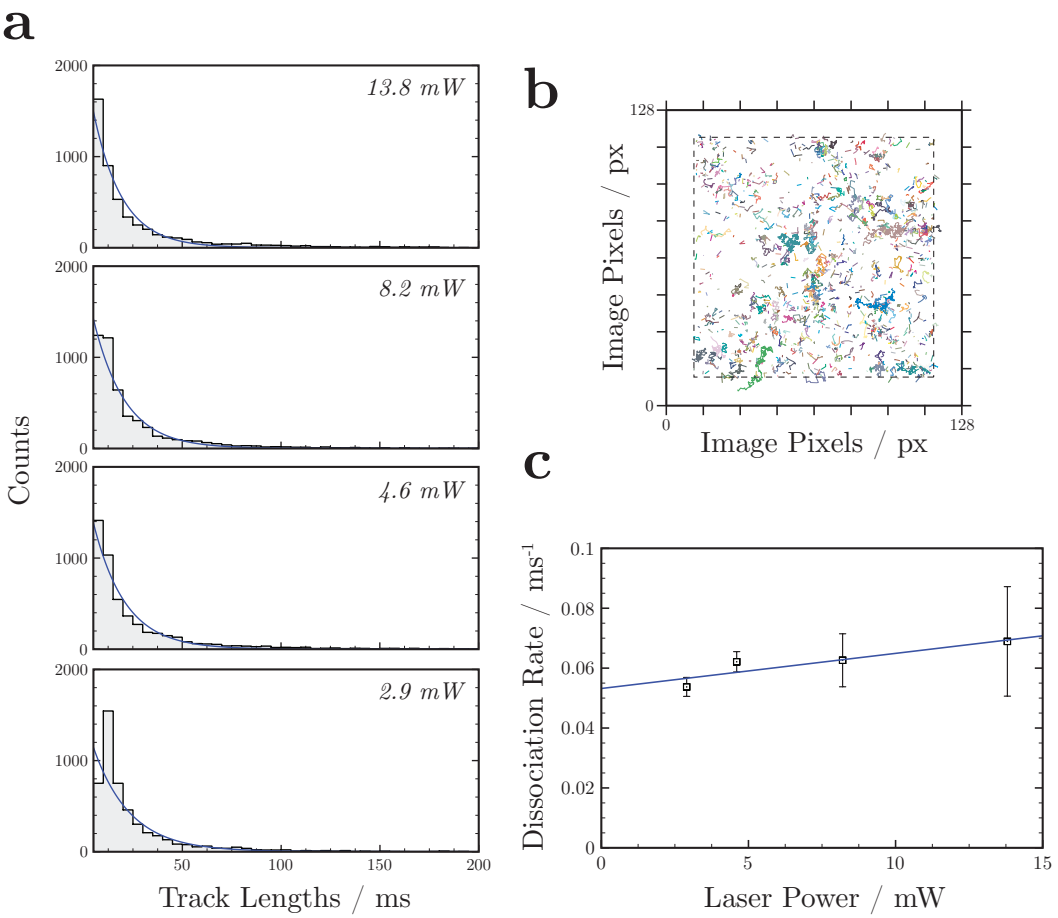

Figure 6.7: *The analysis of monomer dissociation from the lipid bilayer. (A) Histograms showing the acquired track-lengths for the different laser intensities. All samples were fit best with single-exponential functions weighted by the square-root of the data, whose goodness of fits are: 13.8 mW χ_r^2 = 0.25, 8.2 mW χ_r^2 = 0.17, 4.6 mW χ_r^2 = 0.19 and 2.9 mW χ_r^2 = 0.36. (B) A 2D plot of 1000 randomly selected track positions from the 13.8 mW population. The rim buffer is indicated as a dotted line surrounding the tracks in the centre of the plot. (C) The extrapolation of the k_d through plotting the dissociation rate for given laser powers. Errors = exponential fitting errors. A linear fit's intercept at the origin yields the $k_d = 5.3 \pm 0.33\ s^{-1}$.*

6.3.2 Elucidation of Complex Stiochiometry through Photobleaching and Spot-Intensity Analysis

It was found that at higher concentrations, typically where monomers could still be resolved but not tracked for greater than a single-frame (>5 nM in solution), after a short period of imaging, brighter spots spontaneously appeared at the lipid bilayer. These spots were many multiples higher intensity than the diffusing monomers. A plot of the intensity of an example spot with time showing its spontaneous appearance above the background monomer intensity is given (Figure 6.8). It is likely that these brighter spots are resolvable above the

dense monomer coverage of the lipid bilayer due to increased photon ouput per unit time due to effective 'immobilisation' versus the rapidly diffusing monomers. If a point emitter, such as for example a 7 × -labelled α-hemolysin heptamer, were inserted into the lipid bilayer its lateral diffusivity is decreased versus that of the monomer, hence per unit time an enhancement in the brightness of the emitter is detected at that point in the image enabling its clear resolution [298]. Whereas monomeric rapidly diffusing α-hemolysin can't be detected, the brighter more slowly diffusing α-hemolysin species, such as perhaps inserted oligomers, could be resolvable above the background intensity.

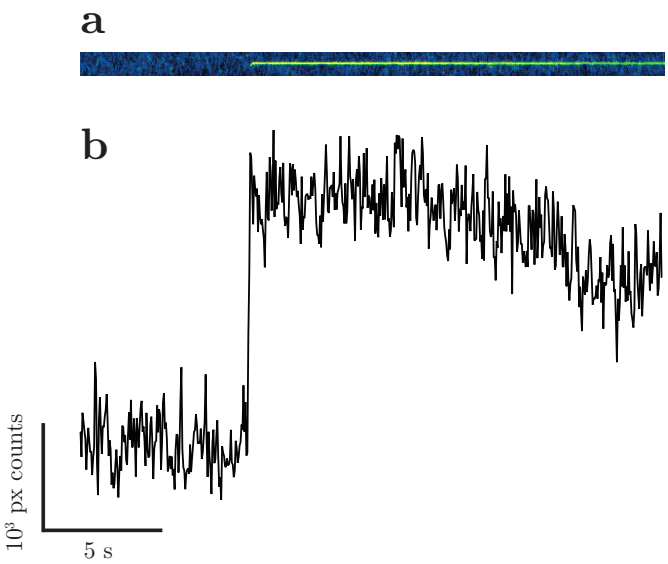

Figure 6.8: *Instantaneous appearance of bright spots in images. (A) A re-sliced projection of the appearance of a spot with time. A 3 pixel ROI over the spot landing zone is projected in time (x-axis). The spot is seen appearing spontaneously, then undergoing subunit-photobleaching. (B) The average intensity of a 3 × 3 pixel ROI over the spot plotted versus time. The time dimension indicated is equivalent for both A and B. Image frame-rate is 50 ms, 1 pixel is equal to 260 nm in size in both x and y dimensions.*

Whilst imaging the appearance of spots in time under constant illumination gives good resolution of the appearance times, photobleaching during constant illumination means that inferences about the fluorophore stoichiometry in the complexes are hard to make. Bright complexes that appear at the membrane could comprise already photobleached subunits. To illustrate the process of spot-appearance, a montage is shown (Figure 6.9). Here, spots are seen appearing over the course of only a few minutes.

An experiment was conceived where the monomer would be incubated with the DHB in darkness prior to illumination. Here, labelled-α-hemolysin could oligomerize without any subunit fluorophores being photobleached. It was apparent that after this incubation, upon

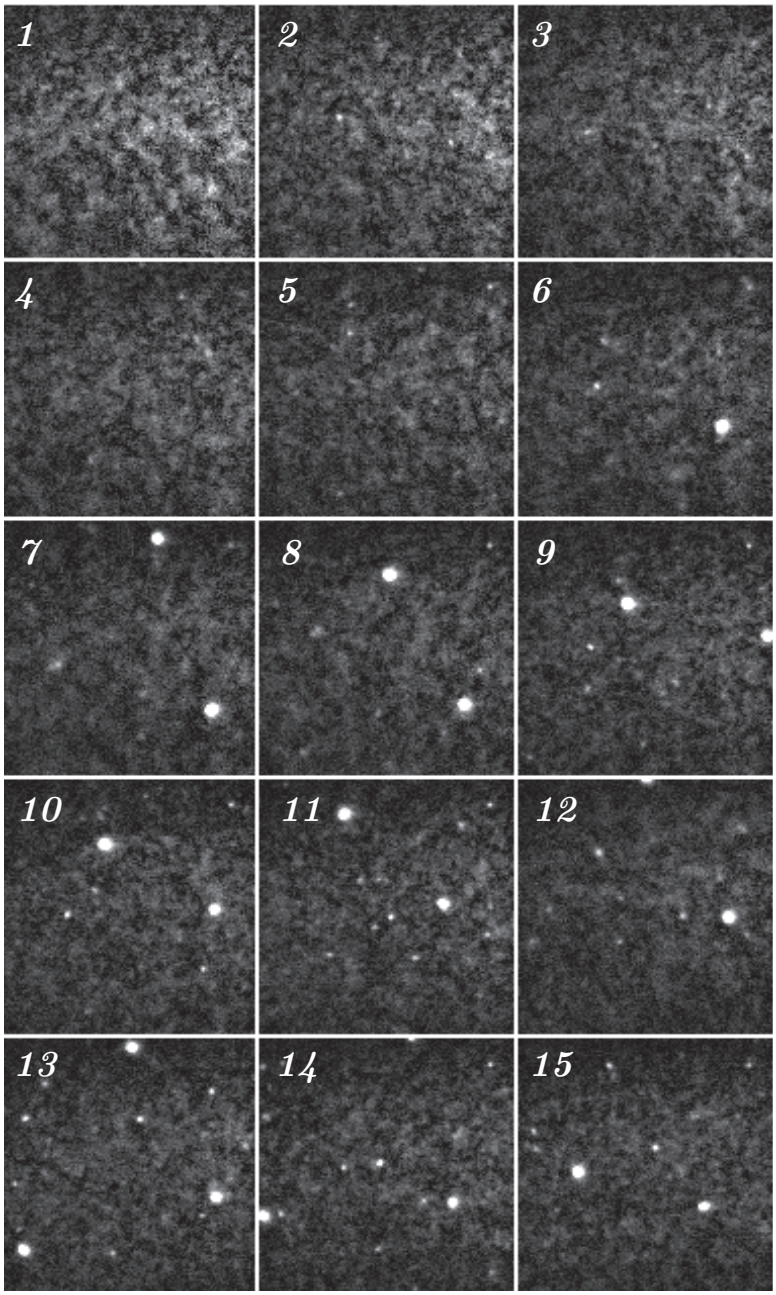

Figure 6.9: *A montage showing the appearance of bright spots with time. A time-lapsed set of images were acquired spread by 15 s. Each frame represents a single 50 ms acquisition.*

illumination there were a number of more slowly diffusing spots, whose intensity was far higher than the monomers. The use of a fast acquisition time in the imaging enabled the resolution of the rapidly-diffusing monomers in the background. A high laser-intensity was required to capture enough photons to resolve the monomers at the fast frame rate. Prior calibration experiments were performed to guage the correct camera gain settings to ensure

a sufficient dynamic range for relative intensity analyses. Using these data, two separate forms of oligomer stoichiometry analysis were performed. The first uses a straightforward fit of the intensity of all resolved PSFs in the image. The second analysis measures individual photobleaching steps in resolved complexes.

The rate of photobleaching in the complexes was rapid, hence only the first 2 frames from 5 separate image stacks was used for the spot intensity analysis (Figure 6.10). The use of multiple images for the intensity analysis was unavoidable, as the number of oligomers in the field of view at this concentration is relatively low. In order to achieve normalisation across the multiple images, a quantile-based normalisation algorithm was employed, originally derived for use when comparing oligonucleotide microarray data [28]. Essentially, this transformation finds the maximum and minimum values across all of the images and assigns all pixels into 256 linearly-distributed bins ranging from the minimum to the maximum intensity. The images are then reconstructed with each pixel taking the mean value of the bin it was assigned to. Each PSF is detected in the image using CLEAN and is fitted with a 2D-Gaussian function as described previously in Chapter 4 [54]. The peak intensities are plotted as a histogram with a bin width equal to $3.49 * \sigma * N^{1/3}$, where σ is the standard deviation, and N is the number of PSFs fitted [239].

Through this analysis, two well separated distributions of intensities are clearly resolved. These were fitted with a log-normal function to describe the lower-intensity distribution, and a Gaussian function to describe the higher-intensity distribution. The presumption is made that the low intensity fluorophores correspond to freely diffusing membrane-adsorbed α-hemolysin monomers. This is based upon the fact that in these images, acquired for a total of 30 s, if all monomer tracks are analysed, no multistep photobleaching is observed outside of the bright complexes. The ratio between the mean values of these two distributions gives an indication of the stoichiometric arrangement in the imaged complexes, $254.55/44.85 = 5.68$. The deconvolution of single-molecule intensity distributions for complex stoichiometry analysis has been addressed previously [196]. Numerical simulations by Mutch *et al.* have demonstrated that if the ratio of the standard deviation to the mean of a fit of calibrating single fluorophores (assumed to be the lowest intensity peak) is larger than that for the multimer, a straightforward Gaussian approximation of the multimeric spot intensities is valid [196]. The reduced χ^2 value ($\chi^2_r = 1.21$) is close to one, indicating a good fit as is theoretically expected.

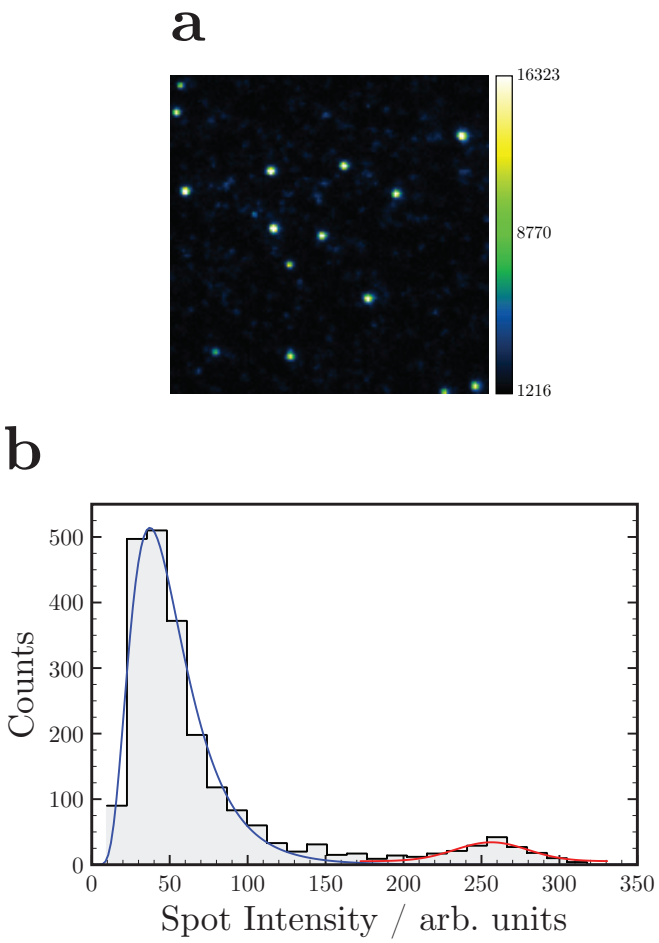

Figure 6.10: *The analysis of spot intensities following monomer incubation with DHBs in darkness. (A) A representative image of the bright spots detected after incubation of monomer with a DHB. (B) A histogram showing the relative distribution of spot intensities corresponding to all detected PSFs in the images analysed. Two peaks are clearly visible, the lowest intensity peak is fitted with a log-normal distribution (blue)* $< x > = 44.85 \pm 1.01$, $\chi_r^2 = 4.23$, *whereas the higher intensity peak is fitted with a Gaussian distribution (red)* $< x > = 254.55 \pm 2.76$, $\chi_r^2 = 1.21$.

A superior method to calculate complex stoichiometry is through the counting of photobleaching steps [43, 57, 165]. Difficulties do still exist however in its implementation here. Because of the rapid lateral diffusion of α-hemolysin monomers on the DHB, a great deal more noise is manifested in the tracks of complexes we image, versus for example, if they were dried onto a coverslip and stationary. All the bright spots present at the start of imaging were tracked throughout the course of photobleaching. An example photobleaching trace from Das *et al.* [57] is shown for comparison with these data (Figure 6.11A). Through the use of a non-linear edge-preserving filter (Chung-Kennedy) [44, 57, 165], the bulk of the noise due to monomers diffusing across the photobleaching complex can be removed from

the signals. A rudimentary step-detection algorithm [57] is employed to find steps, assigned as jumps greater than a multiple of the noise in the signal (described in methods). The number of steps in each trace is presented as a histogram (Figure 6.11C). The peak of the photobleaching step distribution is fitted to a Gaussian distribution with a peak centered at 7.77 ± 0.02.

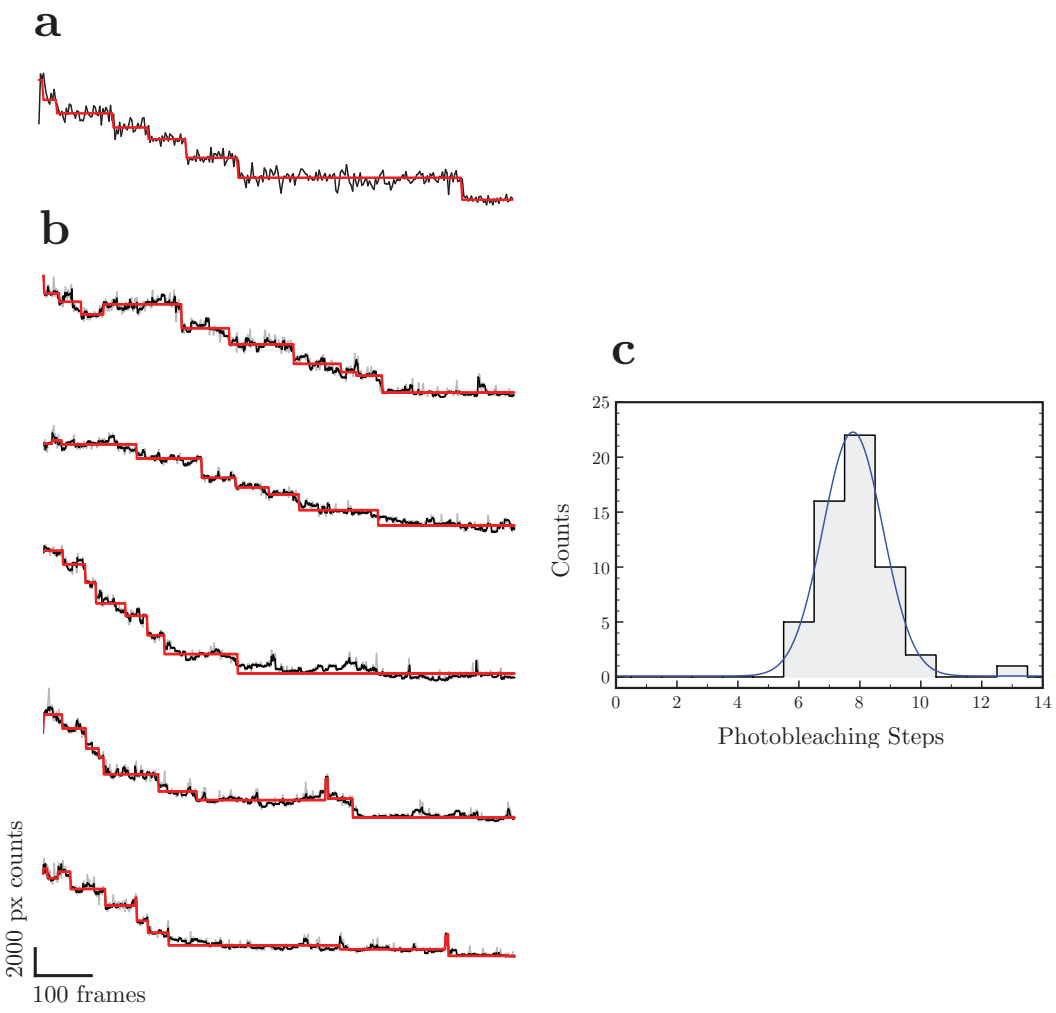

Figure 6.11: *Stoichiometric analysis of complexes through the counting of subunit photobleaching steps. (A) A reproduction of a figure from Das et al. [57], with kind permission of the author. A characteristic 7-step photobleaching from a purified labelled α-hemolysin heptamer dried onto a coverslip. (B) Five representative photobleaching traces from DHB oligomerization experiments. Raw intensity data = grey, Chung-Kennedy filtered data = black, assigned photobleaching steps = red. (C) A histogram showing the numbers of photobleaching steps in all traces analysed (n = 56). Fit indicates a Gaussian distribution centered at* 7.77 ± 0.02 *with a FWHM* $= 1.39 \pm 0.03$, $\chi^2_r = 0.915$.

6.3.3 Direct Observation of Insertion of α-Hemolysin Channels into DHBs

In order to compare the temporal relationship between complex formation in the DHB and actual pore insertion, a simultaneous fluorescence and electrical measurement was made in an attempt to delineate the two processes. By counting the number of pores inserted into the DHB electrically and imaging a region of DHB simultaneously to count the bright complexes forming with time, it is possible to directly compare the rates of the two processes (Figure 6.12).

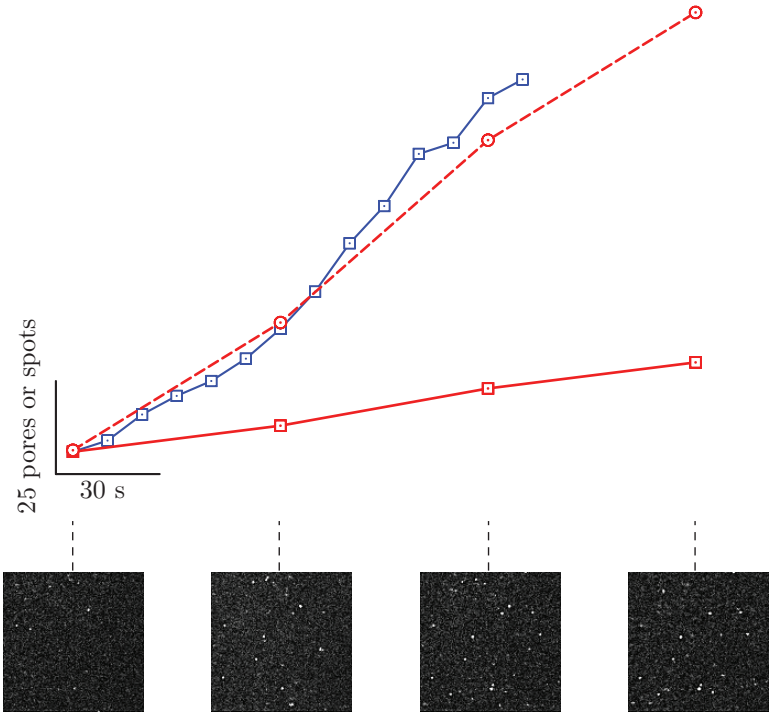

Figure 6.12: *Simultaneous single-molecule fluorescence imaging of complex formation and electrical measurement of pore insertion in a DHB. Synchronised 1 minute after injection, electrically measured pore insertion (blue line) is compared with a simultaneous time-lapsed fluorescence acquisition (solid red line). The rate of appearance of spots in the images is from a visualised area approximately 4.9× smaller than the bilayer area (from calibration). Multiplication of the number of spots in the image areas actually recorded by this scale factor of 4.9 yields an estimate of the number of spots which might be present in the entire bilayer (dotted red line, circular points). The region of electrical trace is shorter than the fluorescence due to inadequate resolution of the electrical signal at high currents (i.e. too much signal noise for pore insertion resolution). Both traces are plotted from time = 0, showing a correlated starting number of channels, with the y-axis scale normalised thereafter.*

This experiment was technically very difficult. Simultaneously injecting protein at high concentration, a requirement for complex formation on a time-scale that we can measure

fluorescently (*i.e.* before significant photobleaching ensues), and measuring electrically is technically cumbersome using the available equipment in our laboratory at this time. The time-lag prior to data capture, approximately 1 min after injection, is enough time for significant pore formation prior to imaging. However, this time-lag was unavoidable as the nano-injector had to be removed from the micro-manipulation apparatus and replaced with the Ag/AgCl electrode for electrical measurements. Whilst it is impossible to say if all the bright complexes are in fact embedded pores, as the entire bilayer is not being imaged in this example, the simultaneous data trends correlate very well.

In order to assess the functional status of the imaged fluorescent complexes directly, an experiment was conceived to fluorescently image the insertion of β-barrels into the lipid bilayer, using a similar approach to that described in the previous chapter.

6.3.3.1 Calcium-Flux Imaging with Single-Molecule Fluorescence Localization - Probing Prepore→Pore Conversion

Building on previous work, where it was shown that it is possible to make efficient simultaneous fluorescence and electrical recordings in DHBs, described in Chapter 5, a two-colour fluorescence experiment was designed around the calcium indicator dye Fluo-8 (analogous to Fluo-4) and Cy3B-labelled α-hemolysin monomers.

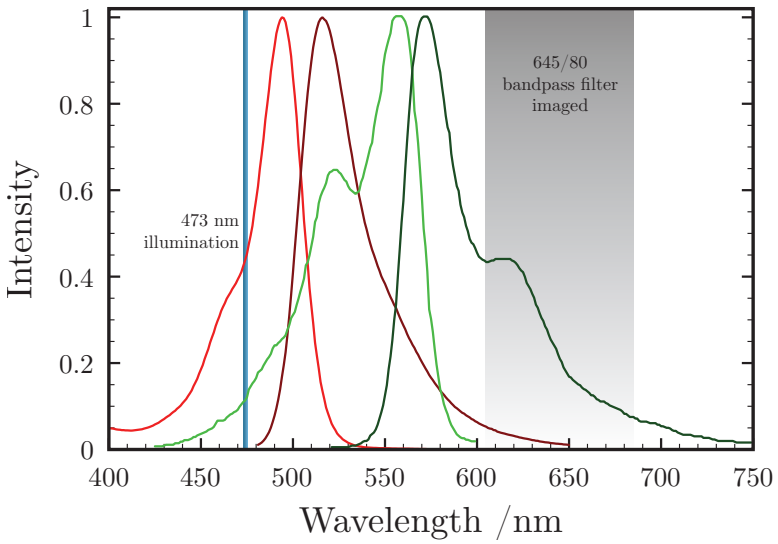

Figure 6.13: *The absorbance and emission spectra of Fluo-8 and Cy3B in water. Fluo-8: absorbance = light red, emission = dark red, Cy3B: absorbance = light green, emission = dark green. Fluo-8 and Cy3B are illuminated with 473 nm laser light. Emitted fluorescence is imaged in one 80 nm band centered at 645 nm.*

It was reasoned that α-hemolysin complex formation could be observed using the fluorescent signal from Cy3B-labelled α-hemolysin monomers, whilst also imaging for pore insertion by using Fluo-8 calcium flux imaging. The spectral profiles of Cy3B and Fluo-8 are illustrated showing the fundamental principles of the experimental hypothesis (Figure 6.13). Fluo-8's absorption cross-section is wide at 473 nm, whereas Cy3B excitation is less efficient at this wavelength. The degree of overlap between the emission spectrum of Fluo-8 and absorbance spectrum of Cy3B is high. Therefore, upon pore formation, the Fluo-8 fluorescence should become locally enhanced around the pores due to calcium flux from the gel into the droplet. The fluorescence of Cy3B can be used to track oligomerization events and complex formation, thereafter it would be possible to probe the temporal relationship between complex formation and the insertion of a pore. It might also serve to prove that the complexes that are imaged in the Cy3B experiments described prior are in fact α-hemolysin prepores or pores, and not other aggregates.

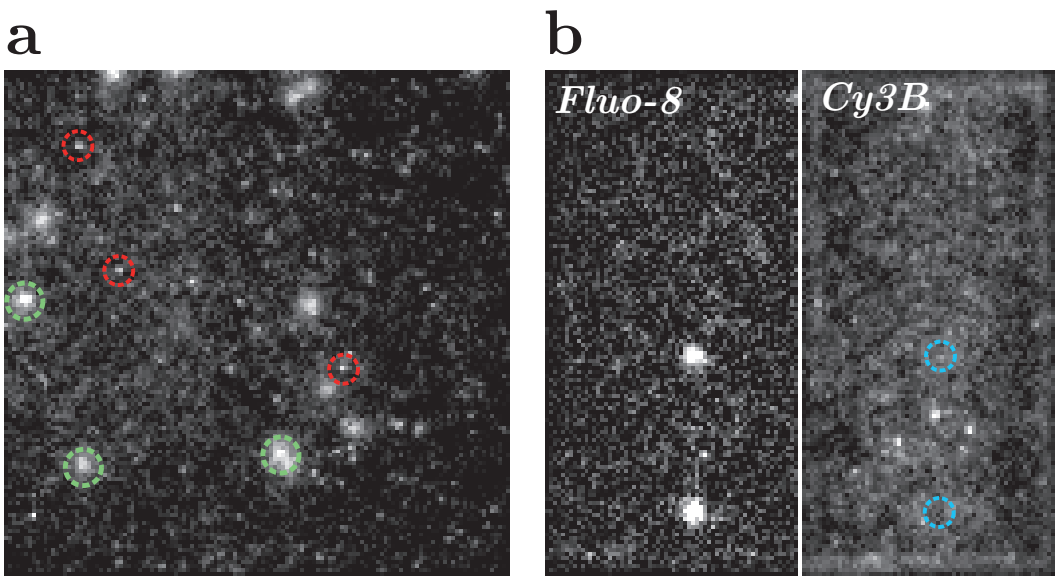

Figure 6.14: *Simultaneous Cy3B and Fluo-8 experiments. (A) A representative image from a Fluo-8 / Cy3B experiment monitoring the channel as indicated in Figure 6.13. Fluo-8 fluorescence can be observed emanating from inserted pores in the DHB, (3× green circles indicate examples) along with bright spots also diffusing in the background (3× red circles indicate examples), however the smaller bright spots photobleach rapidly and generally without multiple steps. (B) A representative dual-colour image showing 128×64 pixels on the left corresponding to the Fluo-8 channel, and 128×64 pixels on the right corresponding to the Cy3B channel. Bright spots are observed in both channels, however corresponding bright spots are not observed in the Cy3B channel where pores are known to be due to Fluo-8 fluorescence.*

A droplet loaded with Fluo-8 was used to preform a lipid bilayer, as in the previous experiments protein was then injected into the droplets. After a lag period, channels could

be observed by punctate Fluo-8 fluorescence enhancement as described previously in Chapter 5. Much dimmer spots could be seen diffusing on the DHB prior to channels appearing, which could be attributed to Cy3B fluorescence, or aggregated Fluo-8 particles (Figure 6.14A). No obvious conversion from a bright complex to a Fluo-8-resolved pore was observed in multiple images.

A separate experiment was also conceived which could potentially decouple the two fluorescence processes by imaging two separate emission channels. In one channel, Fluo-8 fluorescence could be imaged predominantly, whereas the other channel utilised a band-pass emission filter to image Cy3B predominantly. The same process of protein injection and oligomerization monitoring was performed. No clear localization of Cy3B fluorescence in Fluo-8 spot localities was observed (Figure 6.14B). This result is likely due to the large degree of spectral overlap of Fluo-8 and Cy3B emission. The high concentration of Fluo-8 probably inhibits the resolution of single and multiple ($\sim$7) Cy3B molecules.

6.4 Discussion

The rate of binding of α-hemolysin monomers to a DHB lipid bilayer shows a linear dependence on concentration. This demonstrates that there is no cooperativity in the binding process at these low concentrations. The rate of dissociation is calculated from analysing the dependence of the rate of spot disappearance on illuminating laser power. The calculated average lifetime of a bound-monomer on the lipid bilayer is 0.188 s. If this time is multiplied by the average diffusion rate of the monomers ($D_{lat} = 23.4 \pm 6.4\ \mu m^2 s^{-1}$), a value is yielded for the average distance a monomer will diffuse whilst membrane-adsorbed, $4.46 \pm 0.06\ \mu m^2$. The range of diffusion coefficients is much wider than the single mean value stipulated here. However, this gives a crude idea of the area covered by a single α-hemolysin monomer diffusing on a protein-free artificial lipid bilayer at low concentrations.

At picomolar concentrations used for the tracking of monomers binding and dissociating from DHBs, the apparent rate of bright complex formation at the lipid bilayer was extremely low. If the concentration is raised above 1 nM, the spontaneous appearance of bright complexes is observed at the lipid bilayer within a few minutes. By counting the number of monomers on the surface for a given concentration in solution, it was possible to evaluate the steady-state surface concentration of the monomers. This taken with the knowledge

of the rate of diffusion of α-hemolysin monomers allows for a calculation of the expected rate of collision between two monomers whilst adsorbed to the lipid bilayer [98, 99, 102]. According to Hardt [102], the rate of collision ϕ between two particles A and B can be calculated in two-dimensional structured media, where they both have defined steady-state surface concentrations C_A and C_B and lateral diffusion coefficients D_A and D_B, using the relationship

$$\phi = 2\pi N C_A C_B \{D_A / \ln[(\pi N C_B)^{-1/2}/a] + D_B / \ln[(\pi N C_A)^{-1/2}/a]\} \tag{6.2}$$

where N is Avogadro's constant. For homomeric interactions, such as those of α-hemolysin monomers, A and B and equivalent and the equation simplifies to

$$\phi = 4\pi N C^2 \{D / \ln[(\pi N C)^{-1/2}/a]\} \tag{6.3}$$

Using this approach it was possible to approximate the rate of monomer-monomer contacts in DHBs for a range of concentrations. The results of this calculation over a range of concentrations between 1 pM and 1 μM is illustrated (Figure 6.15).

This analysis corroborates the observed lack of complex formation at concentrations lower than 1 nM. At concentrations higher than 10 nM the collisional rate is expected to increase dramatically, in keeping with the observations made at these concentrations. The rate of seven monomers colliding within a 1 nm space of one another at any point in time must be considerably lower than this straightforward monomer-monomer collision rate. Presumably, the rate of step-wise addition to a growing complex would be faster than 7 monomers having to collide simultaneously. However, a detailed kinetic model of assembly is beyond the scope of this thesis.

Whilst this diffusion analysis gives only a theoretical calculation of the rate of collision between monomers, the underlying trend shows that it is much less probable to observe monomer-monomer interactions at concentrations low enough to track α-hemolysin monomers unequivocally binding, diffusing and dissociating from the lipid bilayer. At concentrations higher than are possible to track at the single-molecule level (>10 nM), the stochastic appearance of bright complexes at the lipid bilayer was observed within short periods of time (1-2 mins). The fluorophore stoichiometry in these complexes is shown through photobleaching and spot intensity analysis to range between ~6 and 8 subunits.

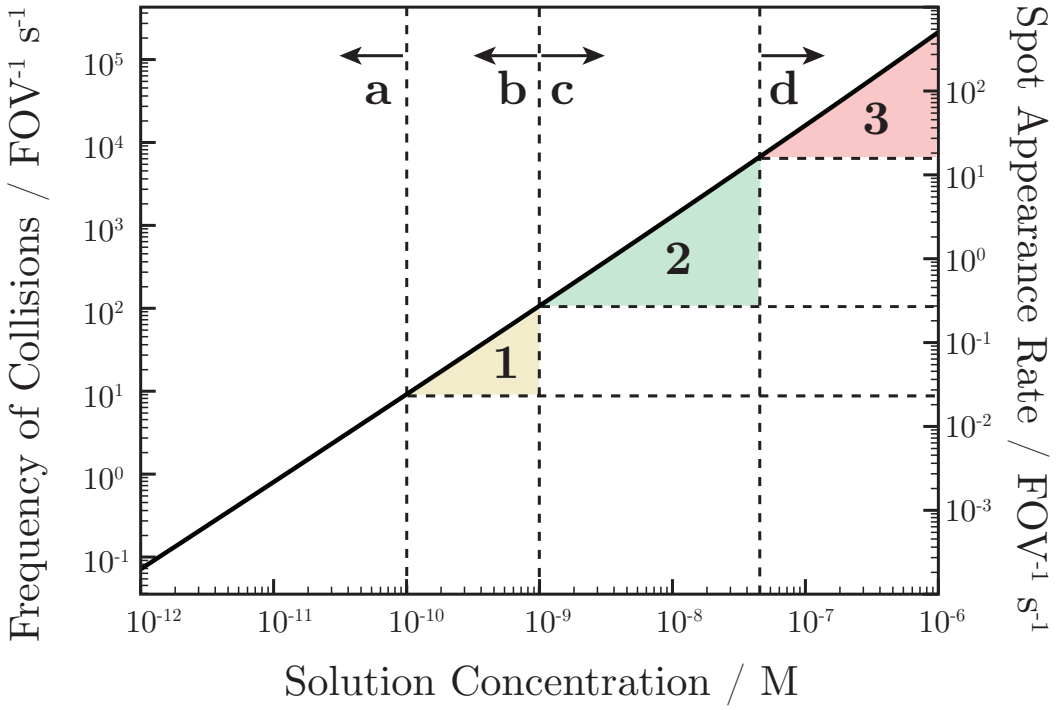

Figure 6.15: *A graph showing the calculated collision frequency for α-hemolysin monomers over a range of concentrations between 1 pM and 1 μM according to Equation 6.3. The boldline demonstrates the calculated frequency of a collisions per imaging field of view using a 60 × objective lens (∼ 2.5×10^{-9} m^2). The right hand axis shows the estimated appearance rate of bright spots at the bilayer for the given concentrations, from experimental estimates. The zone of the graph indicated by (a) is the concentration range at which bright spots are never resolved during reasonable illumination timescales (∼ 2-5 mins), however monomeric α-hemolysin is clearly resolved and can be tracked. Zone (b) indicates the concentration range over which monomers can still be tracked, and very infrequent bright spot appearance is observed. Zone (c) indicates the concentration range where electrical measurements indicate pore insertions on the order of ∼1-10 s^{-1}. In this range fluorescent measurements can be made where bright spots are seen appearing at a comparable rate, and electrical noise is low enough to permit resolution of pore insertions. Zone (d) is the concentration at which electrical noise becomes too great to resolve pores inserting, and bright spots are no longer resolvable above the background signal. The amber zone indicated by (1) is the concentration range at which monomers can be resolved and occasional pores can be resolved inserting electrically with bright spot appearance also clearly resolvable over the course of ∼ 2-5 mins. The green zone indicated by (2) is the concentration range at which the appearance of multiple bright spots can be resolved electrically and fluorescently within a typical 1 min acquisition. The red zone indicated by (3) is the concentration at which pores can be resolved inserting initially, however after a short period of time the total current across the bilayer is too great, resulting in too much signal noise to be able to resolve further pore insertions. At these concentrations fluorescently, bright spot resolution is practically impossible.*

It may be possible to deduce the stoichiometry of the complexes through the kinetic analysis of complex appearance rates versus concentration. The analysis of such data over a wide range of concentrations may facilitate a deduction of the complex stoichiometry through the evaluation of the Hill coefficient. At low concentrations complexes can be observed appearing and these kinetics can be accurately measured. However, at high concentrations

(such as is indicated by the red zone in Figure 6.15) the appearance rate will be difficult to deduce. If the high-concentrations are supplemented by replacing fractions with unlabelled protein, the range of concentrations is greatly enhanced.

These results might be interpreted as showing that prepore formation proceeds extremely rapidly (*i.e.* faster than the frame rate <50 ms), as we are unable to detect intermediate states. However, at higher concentrations of α-hemolysin, necessary to promote pore formation, imaging lower intensity intermediates might be hindered by the dense surface coverage of fluorophores leading to a high background signal. The high rates of photobleaching and of diffusion on the lipid bilayer both compound the difficulty in resolving single-complexes. Although we do not observe any clear evidence for intermediate assembly states, as yet it is impossible to say from these results whether intermediates definitely do not exist.

Experiments designed to delineate the process of oligomer appearance and pore insertion using Fluo-8 fluorescence were less convincing. No clear correlation was observed between punctate bright complexes and the positions of pores in the lipid bilayer. Further conclusions and future experiments are discussed in the following brief chapter.

6.5 Materials and Methods

6.5.1 Materials

All chemicals were from Sigma unless otherwise stated. 1,2–Diphytanoyl–*sn*–glycero–3–phosphocholine (DPhPC) (Avanti Polar Lipids) and Fluo–8H sodium salt (ABD Bioquest) were used without further purification. Potassium chloride (TraceSelect, Fluka) buffered with HEPES was first filtered (0.2 μm cellulose acetate, Nalgene) and then treated with Chelex according to the manufacturer's instructions (BioRad Chelex 100 Resin, Biotechnology Grade, 100–200 mesh) to reduce the concentration of divalent metal cations in solution.

6.5.2 Protein handling

Protein was prepared as described in Chapter 3. Protein from +4°C storage in MES buffer at pH 5.5 was diluted with sodium phosphate buffered 150 mM or 500 mM KCl at pH 7.4 prior to reconcentration using a size-exclusion spin-column (Microcon - 10 kDa

cutoff). Protein was diluted to the desired concentration (as stated in text) using the phosphate buffer. Protein was loaded into a hexadecane-backfilled borosilicate capillary modulated by a micromanipulated piezo-electric nano-injector (Nanoliter 2000, World Precision Instruments) for injection into droplets. Injection was performed under bright-field illumination, where injection was confirmed by swelling of the lipid bilayer area and fluorescence increase at the lipid bilayer.

6.5.3 DHB Methods

DHBs were created on agarose-coated glass coverslips integrated into polymethylmethacrylate (PMMA) devices suitable for TIRF illumination and electrical recording as described in Chapters 4 and 5.

6.5.4 Imaging and Microscopy

For Cy3B imaging, a fibre-coupled 532 nm circularly polarised, continuous-wave laser beam (Compass 215M, Coherent Inc, Santa Clara, CA) was focussed at the back aperture of an oil immersion objective lens (60× Plan Apo N.A. 1.4, Nikon Instruments, UK) mounted on an inverted microscope (Ti-Eclipse, Nikon Instruments UK), illuminating the DHB through TIR at the device coverslip surface. The emitted fluorescence was collected through the same objective and transmitted through dichroic (Q565LP) and band-pass (HQ580/60m) filters (Chroma Technology Corp, Rockingham, VT).

For Fluo-8 and Cy3B imaging, a fibre-coupled 473 nm circularly polarised, continuous-wave laser beam (SDL-473-100SFL, Shanghai Dream Lasers Co., China) was focussed at the back aperture of an oil immersion objective lens (60× Plan Apo N.A. 1.4, Nikon Instruments, UK) mounted on an inverted microscope (Ti-Eclipse, Nikon Instruments UK), illuminating the DHB through TIR at the device coverslip surface. The emitted fluorescence was collected through the same objective and transmitted through dichroic (Q488LP) and band-pass (HQ645/60m) filters (Chroma Technology Corp, Rockingham, VT).

For simultaneous dual-channel Fluo-8 and Cy3B imaging, a fibre-coupled 473 nm circularly polarised, continuous-wave laser beam (SDL-473-100SFL, Shanghai Dream Lasers Co., China) was focussed at the back aperture of an oil immersion objective lens (60× Plan Apo N.A. 1.4, Nikon Instruments, UK) mounted on an inverted microscope (Ti-Eclipse, Nikon Instruments UK), illuminating the DHB through TIR at the device coverslip surface.

The emitted fluorescence was collected through the same objective and directed to the camera by a dichroic (Q488LP). Using an using an OptoSplit II Image Splitter (Cairn Research Ltd., UK) the light was separated using onto two-halves of the camera using a using a dichroic (Q560LP) and two emission filters: for the first channel a HQ525/50m bandpass filter (for Fluo-8 imaging) (Chroma Technology Corp, Rockingham, VT), and for the second channel a HQ580/60m bandpass filter (for Cy3B imaging) (Chroma Technology Corp, Rockingham, VT). This effectively split the emitted light onto two halves $\sim$128 $\times$ 64 pixels in size, for simultaneous imaging.

Images were all acquired using a 128 $\times$ 128 pixel frame-transfer emCCD detector (iXon DU-860, Andor Technology PLC, Belfast, UK). Image sequences were converted to stacked 16-bit Tagged Image File Format (TIFF) bitmaps prior to analysis.

6.5.5 Electrical Recording

Electrical recording was performed exactly as described in Chapter 5.

6.5.6 Single-Particle Tracking

Single-particle tracking for spot detection in binding, dissociation and intensity analysis experiments was performed using the particle tracker plugin developed by the Computational Biophysics Lab at ETH Zurich [234] for ImageJ [1]. Tracks were analysed using Igor Pro (Wavemetrics).

6.5.7 Spot Intensity Analysis

For spot intensity analysis, the first pair of frames of five images were selected and normalised using a quantile-based normalisation plugin for ImageJ [1], written by Mark Longair at the University of Edinburgh, based upon work by Bolstad *et al.* [28]. Briefly, the algorithm undertakes to normalise across multiple images by binning pixels based upon the maximum and minimum values recorded across the images. Thereafter the mean of the quantile bins is substituted for the original pixel value to create a normalised image.

Each PSF was then detected in the images using CLEAN as described previously [54, 263], however using an Igor Pro implementation of the algorithm. Each PSF was fitted with a 2D-Gaussian using the CLEAN algorithm, as described in Chapter 4. The resulting

Gaussian peak intensities of all detected PSFs are then used to create the histogram of spot intensities. The distributions were fitted with log-normal and Gaussian distributions, the log-normal distribution suiting the lower-intensity peak best, and the Gaussian for the higher-intensity peak as judged by relative χ_r^2.

The log-normal distribution was of the form,

$$f(x) \;=\; A * \frac{1}{x\sigma\sqrt{2\pi}} \exp(-\ln x - \mu^2/2\sigma^2) \tag{6.4}$$

where A is the normalisation factor, σ is the standard deviation of the variable logarithm and μ is the mean of the variable logarithm. The mean of the distribution is defined as:

$$< x > \;=\; \exp(\mu + \sigma^2/2) \tag{6.5}$$

6.5.8 Photobleaching Analysis

Photobleaching analysis was performed exactly as reported by Das *et al.* [57]. Briefly, photobleaching tracks were processed by a simplified forward-backward non-linear edge-preserving algorithm Chung-Kennedy [44], however using a single edge-preservation predictor, given by the standard deviation of our 2×2 analysis window. The algorithm computes a mean and standard deviation in two adjacent windows centered between two segments of 2 data points each. The algorithm then reconstitutes the signal using the mean value of the filter segment with the lowest standard deviation. The reconstituted running average maintains sharp changes in signal amplitude, preserving the underlying properties of the signal [57, 101, 165, 166].

Using this filtered signal, photobleaching steps were defined as the point at which the data exceeded a calibrated step size value ($\gtrsim 3\times$ the signal noise) using a χ^2-based analysis of photobleaching step size. Briefly, a range of possible photobleaching step sizes in the intensity dimension were fitted, ranging between 1 and approximately 10 × the signal noise, with the relative χ^2 in the fitted signal being recorded every iteration. The premier value at which the χ^2 was minimised after the first principal jump, according to a real step (by visual inspection), was selected for fitting. No statistical measure of the accuracy was used for the goodness-of-fit of the assigned photobleaching steps. It is important to point out that potentially where few data points are sampled before an apparent step, the median

may be a superior measure of the average value prior and post jump. Photobleaching steps were counted automatically and subsequently verified manually, with the number of steps plotted as a histogram (Figure 6.11C) and fitted to a normal distribution.

Chapter 7

Conclusions

Experiments described in this thesis detail the development of a stable and straightforward to implement *in vitro* lipid bilayer, the Droplet-on-Hydrogel Bilayer. DHBs are shown to be suitable for simultaneous single-molecule fluorescence and single-channel electrical recording studies of embedded or adsorbed proteins. Characterization of membrane proteins is performed in DHBs without the need to purify and reconstitute into detergents and vesicles for *in vitro* study. SDS-PAGE extracts of cell membranes were used to detect detergent-stable ion channels by scanning DHBs across the surface of gels post-electrophoresis. Both α-helical bundle and β-barrel classes of membrane proteins are shown to insert into DHBs.

DHBs are also shown to be a suitable means to image the lipid bilayer at the single-molecule level reproducibly. Imaging the lipid bilayer with the wide-field imaging technique TIRF microscopy is straightforward. The fluidity of DHBs was analysed using single-particle tracking, demonstrating that the lipid bilayers interact with the substrate to a far lesser extent than traditional supported lipid bilayers. This renders DHBs a suitable platform for diffusional measurements and observations of protein interaction at the lipid bilayer.

Simultaneous electrical and fluorescence measurements of ion current emanating from individual α-hemolysin pores in the lipid bilayer has been demonstrated. This shows that highly-correlated simultaneous measurements of fluorescence and electrical current in DHBs is possible.

α-hemolysin monomers were labelled stoichiometrically with the rigidified cyanine dye Cy3B. These proteins were used to image the assembly of the pore-forming toxin α-hemolysin in DHBs. Results showed that assembly occurs on a rapid time-scale with the observation

that oligomeric complexes of subunit stoichiometries of ∼6 to 8 suddenly appear at the lipid bilayer, with no detection of any long-lived lower-intensity intermediate states. Simultaneous electrical recording of pore insertion and fluorescence observation of complex appearance showed similar trends. Work to probe the two processes independently using fluorescence was less successful. No correlation was observed between Cy3B-resolved oligomer formation and pore-formation by calcium-flux imaging.

7.1 Current Experiments

At present, work is continuing to address the issue of spontaneous formation of complexes through high-speed imaging, whilst working to deduce whether these complexes are prepore states or functional inserted pores. Due to the difficulty of injecting protein into the droplets whilst simultaneously recording the electrical signal and maintaining a small enough bilayer to image with a high-magnification objective lens, these experiments are cumbersome. A redesign of apparatus to facilitate more straightforward simultaneous recording is currently in progress.

7.2 Future Prospects

In the future, experiments using the calcium-indicator ion current method may be able to prove if there is a correlation between the appearance of oligomers at the lipid bilayer, and instantaneous pore insertion. If a more red-shifted fluorophore was used instead of Cy3B it might be possible to separate the two fluorescence emission channels to a greater extent. This could yield a direct measurement of prepore to pore conversion rate at the single-molecule level without the need to image the entire bilayer.

Separately, an α-hemolysin monomer system might be generated with an environmentally-sensitive dye modification, similar to experiments by Nguyen *et al.* with γ-hemolysin [198]. This could enable another two-colour experiment where monomers are observed forming oligomers, and in a separate fluorescence channel central loop stem-domain insertion across the lipid bilayer could be directly imaged.

It might also be possible to raise the temperature of the system to closer to physiological temperatures. This might change the lipid phase dynamics, and increase the rate of assembly

at low concentrations. If this is achieved it may enable the tracking of monomers in order to deduce if there are any intermediate states. The experiments might also be performed on rabbit erythrocyte ghosts, or through the incorporation of their membrane components into DHBs. Both procedures hold potential for increasing the rate of oligomerization at lower protein concentrations, potentially allowing for direct tracking of all monomer interactions on the lipid bilayer.

An alternative means to circumvent the requirement for high α-hemolysin concentrations in experiments is to titrate unlabelled protein into the experiments. In doing so, the overall concentration of α-hemolysin on the lipid bilayer can be kept high, whilst enabling a reduction of the labelled-protein requirement. Again, this may facilitate single-particle tracking of the assembly process.

In order to assess the viability of the prepore-state. It may be possible to reproduce some of the earlier work on the prepore of α-hemolysin using stalled mutants with pinned back stem-domains. For example, Zn^{2+}-stalled histidine mutants could be triggered through injection of EDTA into a droplet containing prepores.

With the present information, and these experimental ideas, it is foreseeable that in the near future, the questions surrounding the mode of assembly of the staphylococcal pore-forming toxin α-hemolysin will be answered. Analogous experiments might be performed using close relatives of α-hemolysin such as other bi-component leukocidins. Larger pore-forming toxins such as the cholesterol-dependent cytolysins might be analysed in a similar manner. Such CDCs consist of many more subunits than the leukocidins [16]. It may be the case that large complex intermediate states will be resolved above the background signal of the diffusing monomeric protein.

In addition, DHBs are an ideal platform for the high-throughput screening of membrane protein processes, such as for example, the binding of pharmaceutical targets to key membrane proteins. Similar technologies are presently in use in the pharmaceutical industry making use of frog oocytes and patch-clamping, which is a cumbersome process. Heterogeneous levels of protein expression in oocytes in high-throughput multiplexed patch-clamping systems greatly affects the quality of data recovered from assays. The reagent control afforded in DHB experiments may represent a possible means to overcome this hindrance. Whilst to date no eukaryotic complexes have been incorporated into DHBs, their properties do suggest that this may be possible. For example, it might be possible to

build an array of DHBs with key eukaryotic membrane proteins embedded, then assay the proteins response to a massive library of drug targets in parallel.

Bibliography

[1] Abramoff, M. D., Magelhaes, P. J., and Ram, S. J. Image processing with ImageJ. *Biophotonics Int. 11*, 7 (2004), 36–42.

[2] Ahn, K., Kerbage, C., Hunt, T. P., Westervelt, R. M., Link, D. R., and Weitz, D. A. Dielectrophoretic manipulation of drops for high-speed microfluidic sorting devices. *App. Phys. Lett. 88*, 2 (2006), 024104.

[3] Aksimentiev, A., and Schulten, K. Imaging α-hemolysin with molecular dynamics: ionic conductance, osmotic permeability, and the electrostatic potential map. *Biophys. J. 88*, 6 (2005), 3745–3761.

[4] Alvarez, O., and Latorre, R. Voltage-dependent capacitance in lipid bilayers made from monolayers. *Biophys J 21*, 1 (1978), 1–17.

[5] Arbuthnott, J. P., Freer, J. H., and Bernheimer, A. W. Physical states of staphylococcal α-toxin. *J. Bacteriol. 94*, 4 (1967), 1170–1177.

[6] Arbuthnott, J. P., Freer, J. H., and Billcliffe, B. Lipid-induced polymerization of staphylococcal α-toxin. *J. Gen. Microbiol. 75*, 2 (1973), 309–319.

[7] Ashcroft, F. M. *Ion Channels and Disease*. Academic Press: San Diego, 2000.

[8] Ashley, R. H. *Ion channels: practical approach*. IRL: Oxford, 1995.

[9] Atkins, P., and de Paula, J. *Physical Chemistry*, 8 ed. Oxford University Press, 2007.

[10] Axelrod, D., Burghardt, T., and Thompson, N. Total internal reflection fluorescence. *Annu. Rev. Biophys. Bioeng. 13* (1984), 247–268.

[11] Bayley, H. Designed membrane channels and pores. *Curr. Opin. Biotechnol. 10*, 1 (1999), 94–103.

[12] Bayley, H. Understanding and manipulating channels and pores. *Mol. Biosystems 3*, 10 (2007), 645–647.

[13] Bayley, H., and Cremer, P. S. Stochastic sensors inspired by biology. *Nature 413*, 6852 (2001), 226–230.

[14] Bayley, H., Cronin, B., Heron, A., Holden, M., Hwang, W., Syeda, R., Thompson, J., and Wallace, M. Droplet interface bilayers. *Mol. Biosystems 4*, 12 (2008), 1191–1208.

[15] Bayley, H., and Jayasinghe, L. Functional engineered channels and pores (review). *Mol. Membr. Biol. 21*, 4 (2004), 209–220.

[16] Bayley, H., Jayasinghe, L., and Wallace, M. Prepore for a breakthrough. *Nat. Struct. Mol. Biol. 12*, 5 (2005), 385–386.

[17] Belmonte, G., Cescatti, L., Ferrari, B., Nicolussi, T., Ropele, M., and Menestrina, G. Pore formation by *Staphylococcus aureus* α-toxin in lipid bilayers. dependence upon temperature and toxin concentration. *Eur. Biophys. J. 14*, 6 (1987), 349–358.

[18] Berry, R. M. ATP synthesis: the world's smallest wind-up toy. *Curr. Biol. 15*, 10 (2005), 385–387.

[19] Betzig, E., Patterson, G. H., Sougrat, R., Lindwasser, O. W., Olenych, S., Bonifacino, J. S., Davidson, M. W., Lippincott-Schwartz, J., and Hess, H. F. Imaging intracellular fluorescent proteins at nanometer resolution. *Science 313*, 5793 (2006), 1642–1645.

[20] Bezanilla, F. How membrane proteins sense voltage. *Nat. Rev. Mol. Cell Biol. 9*, 4 (2008), 323–332.

[21] Bhakdi, S., Fussle, R., and Tranum-Jensen, J. Staphylococcal α-toxin: oligomerization of hydrophilic monomers to form amphiphilic hexamers induced through contact with deoxycholate detergent micelles. *Proc. Natl. Acad. Sci. U.S.A. 78*, 9 (1981), 5475–5479.

[22] Bhakdi, S., Muhly, M., and Fussle, R. Correlation between toxin binding and hemolytic activity in membrane damage by staphylococcal α-toxin. *Infect. Immun. 46*, 2 (1984), 318–323.

[23] Bhakdi, S., and Tranum-Jensen, J. α-Toxin of *Staphylococcus aureus*. *Microbiol. Rev. 55*, 4 (1991), 733–751.

[24] Bhakdi, S., and Tranum-Jensen, J. Complement lysis: a hole is a hole. *Immunol Today 12*, 9 (1991), 318–320.

[25] Biskup, C., Kusch, J., Schulz, E., Nache, V., Schwede, F., Lehmann, F., Hagen, V., and Benndorf, K. Relating ligand binding to activation gating in CNGA2 channels. *Nature 446*, 7134 (2007), 440–443.

[26] Biteen, J. S., Thompson, M. A., Tselentis, N. K., Bowman, G. R., Shapiro, L., and Moerner, W. E. Super-resolution imaging in live *Caulobacter crescentus* cells using photoswitchable eYFP. *Nat. Methods 5*, 11 (2008), 947–949.

[27] Blunck, R., McGuire, H., Hyde, H. C., and Bezanilla, F. Fluorescence detection of the movement of single KcsA subunits reveals cooperativity. *Proc. Natl. Acad. Sci. U.S.A. 105*, 51 (2008), 20263–20268.

[28] Bolstad, B. M., Irizarry, R. A., Astrand, M., and Speed, T. P. A comparison of normalization methods for high density oligonucleotide array data based on variance and bias. *Bioinformatics 19*, 2 (2003), 185–193.

[29] Borisenko, V., Lougheed, T., Hesse, J., Füreder-Kitzmüller, E., Fertig, N., Behrends, J. C., Woolley, G. A., and Schütz, G. J. Simultaneous optical and electrical recording of single gramicidin channels. *Biophys. J. 84*, 1 (2003), 612–622.

[30] Bradford, M. M. A rapid and sensitive method for the quantitation of microgram quantities of protein utilizing the principle of protein-dye binding. *Anal. Biochem. 72* (1976), 248–254.

[31] Braha, O., Webb, J., Gu, L.-Q., Kim, K., and Bayley, H. Carriers versus adapters in stochastic sensing. *Chemphyschem 6*, 5 (2005), 889–892.

[32] Breyton, C., Chabaud, E., Chaudier, Y., Pucci, B., and Popot, J.-L. Hemifluorinated surfactants: a non-dissociating environment for handling membrane proteins in aqueous solutions? *FEBS Lett. 564*, 3 (2004), 312–318.

[33] Buckelew, A. R. J., and Colacicco, G. Lipid monolayers. interactions with staphylococcal α-toxin. *Biochim. Biophys. Acta 233*, 1 (1971), 7–16.

[34] Burghardt, T. P., and Thompson, N. L. Effect of planar dielectric interfaces on fluorescence emission and detection. Evanescent excitation with high-aperture collection. *Biophys. J. 46*, 6 (1984), 729–737.

[35] Cassidy, P., Six, H., and Harshman, S. Biological effects of staphylococcal α-toxin. *Biochim. Biophys. Acta 332*, 3 (1974), 413–423.

[36] Cevc, G. *Phospholipid Handbook*. Marcel Dekker: New York, 1993.

[37] Chalfie, M., Tu, Y., Euskirchen, G., Ward, W. W., and Prasher, D. C. Green fluorescent protein as a marker for gene expression. *Science 263*, 5148 (1994), 802–805.

[38] Chan, Y.-H. M., and Boxer, S. G. Model membrane systems and their applications. *Curr. Opin. Chem. Biol. 11*, 6 (2007), 581–587.

[39] Cheezum, M. K., Walker, W. F., and Guilford, W. H. Quantitative comparison of algorithms for tracking single fluorescent particles. *Biophys. J. 81*, 4 (2001), 2378–2388.

[40] Cheley, S., Braha, O., Lu, X., Conlan, S., and Bayley, H. A functional protein pore with a 'retro' transmembrane domain. *Protein Sci. 8*, 6 (1999), 1257–1267.

[41] Cheley, S., Malghani, M. S., Song, L., Hobaugh, M., Gouaux, J. E., Yang, J., and Bayley, H. Spontaneous oligomerization of a staphylococcal α-hemolysin conformationally constrained by removal of residues that form the transmembrane β-barrel. *Protein Eng. 10*, 12 (1997), 1433–1443.

[42] Chen, I., Howarth, M., Lin, W., and Ting, A. Y. Site-specific labeling of cell surface proteins with biophysical probes using biotin ligase. *Nat. Methods 2*, 2 (2005), 99–104.

[43] Chu, S. Biology and polymer physics at the single-molecule level. *Philos. Trans. R. Soc. London A 361*, 1805 (2003), 689–698.

[44] Chung, S. H., and Kennedy, R. A. Forward-backward non-linear filtering technique for extracting small biological signals from noise. *J. Neurosci. Methods 40*, 1 (1991), 71–86.

[45] Clark, B. An efficient implementation of the algorithm 'CLEAN'. *Astronomy and Astrophysics 89*, 3 (1980), 377–378.

[46] Cleland, W. Dithiothreitol, a new protective reagent for SH groups. *Biochemistry 3* (1964), 480–482.

[47] Colacicco, G., and Buckelew, A. R. Lipid monolayers: influence of lipid film and urea on the surface activity of staphylococcal α-toxin. *Lipids 6*, 8 (1971), 546–553.

[48] Cooney, J., Kienle, Z., Foster, T. J., and O'Toole, P. W. The γ-hemolysin locus of *Staphylococcus aureus* comprises three linked genes, two of which are identical to the genes for the F and S components of leukocidin. *Infect. Immun. 61*, 2 (1993), 768–771.

[49] Cooper, M., Ebner, A., Briggs, M., Burrows, M., Gardner, N., Richardson, R., and West, R. Cy3B: improving the performance of cyanine dyes. *J. Fluorescence 14*, 2 (2004), 145–150.

[50] Cozmuta, I., O'Keeffe, J., Deepak, B., and Stolc, V. Hybrid MD-Nernst-Planck model of the α-hemolysin conductance properties. *Mol. Simul. 311*, 2 (2005), 79–83.

[51] Crane, J. M., Kiessling, V., and Tamm, L. K. Measuring lipid asymmetry in planar supported bilayers by fluorescence interference contrast microscopy. *Langmuir 21*, 4 (2005), 1377–1388.

[52] Cremer, P. S., and Boxer, S. G. Formation and spreading of lipid bilayers on formation and spreading of lipid bilayers on planar glass supports. *J. Phys. Chem. B 103* (1999), 2554–2559.

[53] Crocker, J., and Grier, D. Methods of digital video microscopy for colloidal studies. *J. Coll. Interface Sci. 179* (1996), 298–310.

[54] Cronin, B., de Wet, B., and Wallace, M. I. Lucky imaging: Improved localization accuracy for single molecule imaging. *Biophys. J.* (2009), in press.

[55] Czajkowsky, D. M., Sheng, S., and Shao, Z. Staphylococcal α-hemolysin can form hexamers in phospholipid bilayers. *J. Mol. Biol. 276*, 2 (1998), 325–330.

[56] Dang, T. X., Hotze, E. M., Rouiller, I., Tweten, R. K., and Wilson-Kubalek, E. M. Prepore to pore transition of a cholesterol-dependent cytolysin visualized by electron microscopy. *J. Struct. Biol. 150*, 1 (2005), 100–108.

[57] Das, S. K., Darshi, M., Cheley, S., Wallace, M. I., and Bayley, H. Membrane protein stoichiometry determined from the step-wise photobleaching of dye-labelled subunits. *Chembiochem 8*, 9 (2007), 994–999.

[58] Davanloo, P., Rosenberg, A. H., Dunn, J. J., and Studier, F. W. Cloning and expression of the gene for bacteriophage T7 RNA polymerase. *Proc. Natl. Acad. Sci. U.S.A. 81*, 7 (1984), 2035–2039.

[59] Delcour, A. H. Function and modulation of bacterial porins: insights from electrophysiology. *FEMS Microbiol. Lett. 151*, 2 (1997), 115–123.

[60] Demuro, A., and Parker, I. Imaging the activity and localization of single voltage-gated ca^{2+} channels by total internal reflection fluorescence microscopy. *Biophys. J. 86*, 5 (2004), 3250–3259.

[61] Demuro, A., and Parker, I. "Optical patch-clamping": single-channel recording by imaging ca^{2+} flux through individual muscle acetylcholine receptor channels. *J. Gen. Physiol. 126*, 3 (2005), 179–192.

[62] Dillingham, M. S., and Wallace, M. I. Protein modification for single molecule fluorescence microscopy. *Org. Biomol. Chem. 6*, 17 (2008), 3031–3037.

[63] Dobson, C. M. Protein folding and misfolding. *Nature 426*, 6968 (2003), 884–890.

[64] Eggeling, C., Ringemann, C., Medda, R., Schwarzmann, G., Sandhoff, K., Polyakova, S., Belov, V., Hein, B., von Middendorff, C., Schonle, A., and Hell, S. Direct observation of the nanoscale dynamics of membrane lipids in a living cell. *Nature* (2008), in press.

[65] Ernst, L. A., Gupta, R. K., Mujumdar, R. B., and Waggoner, A. S. Cyanine dye labeling reagents for sulfhydryl groups. *Cytometry 10*, 1 (1989), 3–10.

[66] Ervin, E. N., White, R. J., Owens, T. G., Tang, J. M., and White, H. S. AC conductance of transmembrane protein channels. The number of ionized residue mobile counterions at infinite dilution. *J. Phys. Chem. B 111*, 30 (2007), 9165–9171.

[67] Esser, A. F. Big MAC attack: complement proteins cause leaky patches. *Immunol. Today 12*, 9 (1991), 316–318.

[68] Essmann, F., Bantel, H., Totzke, G., Engels, I. H., Sinha, B., Schulze-Osthoff, K., and Janicke, R. U. *Staphylococcus aureus* α-toxin-induced cell death: predominant necrosis despite apoptotic caspase activation. *Cell Death Differ. 10*, 11 (2003), 1260–1272.

[69] Evans, E., and Sackmann, E. Translational and rotational drag coefficients for a disk moving in a liquid membrane associated with a rigid substrate. *J. Fluid Mech. 194* (1988), 553–561.

[70] Fang, Y., Cheley, S., Bayley, H., and Yang, J. The heptameric prepore of a staphylococcal α-hemolysin mutant in lipid bilayers imaged by atomic force microscopy. *Biochemistry 36*, 31 (1997), 9518–9522.

[71] Feller, S. E., Yin, D., Pastor, R. W., and MacKerell, A. D. J. Molecular dynamics simulation of unsaturated lipid bilayers at low hydration: parameterization and comparison with diffraction studies. *Biophys. J. 73*, 5 (1997), 2269–2279.

[72] Foster, T. J., and Hook, M. Surface protein adhesins of *Staphylococcus aureus*. *Trends Microbiol. 6*, 12 (1998), 484–488.

[73] Freer, J. H., Arbuthnott, J. P., and Bernheimer, A. W. Interaction of staphylococcal α-toxin with artificial and natural membranes. *J. Bacteriol. 95*, 3 (1968), 1153–1168.

[74] Fujiwara, H., Fujihara, M., and Ishiwata, T. Dynamics of the spontaneous formation of a planar phospholipid bilayer: A new approach by simultaneous electrical and optical measurements. *J. Chem. Phys. 119*, 13 (2003), 6768–6775.

[75] Funakoshi, K., Suzuki, H., and Takeuchi, S. Lipid bilayer formation by contacting monolayers in a microfluidic device for membrane protein analysis. *Anal. Chem. 78*, 24 (2006), 8169–8174.

[76] Furini, S., Domene, C., Rossi, M., Tartagni, M., and Cavalcanti, S. Model-based prediction of the α-hemolysin structure in the hexameric state. *Biophys. J.* (2008), in press.

[77] Fussle, R., Bhakdi, S., Sziegoleit, A., Tranum-Jensen, J., Kranz, T., and Wellensiek, H. J. On the mechanism of membrane damage by *Staphylococcus aureus* α-toxin. *J. Cell Biol. 91*, 1 (1981), 83–94.

[78] Fussle, R., Tranum-Jensen, J., Sziegoleit, A., and Bhakdi, S. Incorporation of toxin pores into liposomes. *Methods Enzymol. 165* (1988), 285–293.

[79] Galdiero, S., and Gouaux, E. High resolution crystallographic studies of α-hemolysin-phospholipid complexes define heptamer-lipid head group interactions: implication for understanding protein-lipid interactions. *Protein Sci. 13*, 6 (2004), 1503–1511.

[80] Gambin, Y., Lopez-Esparza, R., Reffay, M., Sierecki, E., Gov, N. S., Genest, M., Hodges, R. S., and Urbach, W. Lateral mobility of proteins in liquid membranes revisited. *Proc. Natl. Acad. Sci. U.S.A. 103*, 7 (2006), 2098–2102.

[81] Gazzarrini, S., Severino, M., Lombardi, M., Morandi, M., DiFrancesco, D., Van Etten, J. L., Thiel, G., and Moroni, A. The viral potassium channel Kcv: structural and functional features. *FEBS Lett. 552*, 1 (2003), 12–16.

[82] Gee, K. R., Brown, K. A., Chen, W. N., Bishop-Stewart, J., Gray, D., and Johnson, I. Chemical and physiological characterization of Fluo-4 Ca^{2+}-indicator dyes. *Cell Calcium 27*, 2 (2000), 97–106.

[83] Geertsma, E. R., Groeneveld, M., Slotboom, D.-J., and Poolman, B. Quality control of overexpressed membrane proteins. *Proc. Natl. Acad. Sci. U.S.A. 105*, 15 (2008), 5722–5727.

[84] Gelles, J., Schnapp, B. J., and Sheetz, M. P. Tracking kinesin-driven movements with nanometre-scale precision. *Nature 331*, 450-453 (1988).

[85] Getz, E. B., Xiao, M., Chakrabarty, T., Cooke, R., and Selvin, P. R. A comparison between the sulfhydryl reductants tris(2-carboxyethyl)phosphine and dithiothreitol for use in protein biochemistry. *Anal. Biochem. 273*, 1 (1999), 73–80.

[86] Ghosh, R. N., and Webb, W. W. Automated detection and tracking of individual and clustered cell surface low density lipoprotein receptor molecules. *Biophys. J. 66*, 5 (1994), 1301–1318.

[87] Glazier, S., Vanderah, D., Plant, A., Bayley, H., Valincius, G., and Kasianowicz, J. Reconstitution of the pore-forming toxin α-hemolysin in phospholipid/18-octadecyl-1-thiahexa(ethylene oxide) and phospholipid/n-octadecanethiol supported bilayer membranes. *Langmuir 16*, 26 (2000), 10428–10435.

[88] Goennenwein, S., Tanaka, M., Hu, B., Moroder, L., and Sackmann, E. Functional incorporation of integrins into solid supported membranes on ultrathin films of cellulose: impact on adhesion. *Biophys. J. 85*, 1 (2003), 646–655.

[89] Gold, V. A. M., Duong, F., and Collinson, I. Structure and function of the bacterial Sec translocon. *Mol. Membr. Biol. 24*, 5-6 (2007), 387–394.

[90] Gouaux, J. E., Braha, O., Hobaugh, M. R., Song, L., Cheley, S., Shustak, C., and Bayley, H. Subunit stoichiometry of staphylococcal α-hemolysin in crystals and on membranes: a heptameric transmembrane pore. *Proc. Natl. Acad. Sci. U.S.A. 91*, 26 (1994), 12828–12831.

[91] Gregory, J. The stability of n-ethylmaleimide and its reactivity with sulfhydryl groups. *J. Am. Chem. Soc. 77* (1955), 3922–3923.

[92] Gu, L., Cheley, S., and Bayley, H. Prolonged residence time of a noncovalent molecular adapter, β-cyclodextrin, within the lumen of mutant α-hemolysin pores. *J. Gen. Physiol. 118*, 5 (2001), 481–494.

[93] Gu, L. Q., and Bayley, H. Interaction of the noncovalent molecular adapter, β-cyclodextrin, with the staphylococcal α-hemolysin pore. *Biophys. J. 79*, 4 (2000), 1967–1975.

[94] Gu, L. Q., and Bayley, H. Interaction of the noncovalent molecular adapter, β-cyclodextrin, with the staphylococcal α-hemolysin pore. *Biophys. J. 79*, 4 (2000), 1967–1975.

[95] Gu, L. Q., Braha, O., Conlan, S., Cheley, S., and Bayley, H. Stochastic sensing of organic analytes by a pore-forming protein containing a molecular adapter. *Nature 398*, 6729 (1999), 686–690.

[96] Gu, L.-Q., Cheley, S., and Bayley, H. Electroosmotic enhancement of the binding of a neutral molecule to a transmembrane pore. *Proc. Natl. Acad. Sci. U.S.A. 100*, 26 (2003), 15498–15503.

[97] Guillet, V., Roblin, P., Werner, S., Coraiola, M., Menestrina, G., Monteil, H., Prevost, G., and Mourey, L. Crystal structure of leucotoxin S component: new insight into the staphylococcal β-barrel pore-forming toxins. *J. Biol. Chem. 279*, 39 (2004), 41028–41037.

[98] Gupte, S., Wu, E. S., Hoechli, L., Hoechli, M., Jacobson, K., Sowers, A. E., and Hackenbrock, C. R. Relationship between lateral diffusion, collision frequency, and electron transfer of mitochondrial inner membrane oxidation-reduction components. *Proc. Natl. Acad. Sci. U.S.A. 81*, 9 (1984), 2606–2610.

[99] Gupte, S. S., Chazotte, B., Leesnitzer, M. A., and Hackenbrock, C. R. Two-dimensional diffusion of F1F0-ATP synthase and ADP/ATP translocator. Testing a hypothesis for ATP synthesis in the mitochondrial inner membrane. *Biochim. Biophys. Acta 1069*, 2 (1991), 131–138.

[100] Hamill, O. P., Marty, A., Neher, E., Sakmann, B., and Sigworth, F. J. Improved patch-clamp techniques for high-resolution current recording from cells and cell-free membrane patches. *Pflugers Arch. 391*, 2 (1981), 85–100.

[101] Haran, G. Noise reduction in single-molecule fluorescence trajectories of folding proteins. *Chem. Phys. 307*, 2-3 (2004), 137–145.

[102] Hardt, S. L. Rates of diffusion controlled reactions in one, two and three dimensions. *Biophys. Chem. 10*, 3-4 (1979), 239–243.

[103] Harms, G., Orr, G., and Lu, P. Probing ion channel conformational dynamics using simultaneous single-molecule ultrafast spectroscopy and patch-clamp electric recording. *App. Phys. Lett. 84*, 10 (2004), 1792–1794.

[104] Harms, G. S., Cognet, L., Lommerse, P. H., Blab, G. A., Kahr, H., Gamsjager, R., Spaink, H. P., Soldatov, N. M., Romanin, C., and Schmidt, T. Single-molecule imaging of l-type Ca^{2+} channels in live cells. *Biophys. J. 81*, 5 (2001), 2639–2646.

[105] Harms, G. S., Orr, G., Montal, M., Thrall, B. D., Colson, S. D., and Lu, H. P. Probing conformational changes of gramicidin ion channels by single-molecule patch-clamp fluorescence microscopy. *Biophys. J. 85*, 3 (2003), 1826–1838.

[106] Harshman, S., Boquet, P., Duflot, E., Alouf, J. E., Montecucco, C., and Papini, E. Staphylococcal α-toxin: a study of membrane penetration and pore formation. *J. Biol. Chem. 264*, 25 (1989), 14978–14984.

[107] Hecht, E. *Optics*, 4 ed. Addison Wesley, 2000.

[108] Heginbotham, L., LeMasurier, M., Kolmakova-Partensky, L., and Miller, C. Single streptomyces lividans K^+ channels: functional asymmetries and sidedness of proton activation. *J. Gen. Physiol. 114*, 4 (1999), 551–560.

[109] Heron, A. J., Thompson, J. R., Cronin, B., and Wallace, M. I. Simultaneous measurement of ionic current and fluorescence from single protein pores. *J. Am. Chem. Soc.* (2009), Accepted for publication.

[110] Heron, A. J., Thompson, J. R., Mason, A. E., and Wallace, M. I. Direct detection of membrane channels from gels using water-in-oil droplet bilayers. *J. Am. Chem. Soc. 129*, 51 (2007), 16042–16047.

[111] Heuck, A. P., Savva, C. G., Holzenburg, A., and Johnson, A. E. Conformational changes that effect oligomerization and initiate pore formation are triggered throughout perfringolysin O upon binding to cholesterol. *J. Biol. Chem. 282*, 31 (2007), 22629–22637.

[112] Heuck, A. P., Tweten, R. K., and Johnson, A. E. Assembly and topography of the prepore complex in cholesterol-dependent cytolysins. *J. Biol. Chem. 278*, 33 (2003), 31218–31225.

[113] Hildebrand, A., Pohl, M., and Bhakdi, S. *Staphylococcus aureus* α-toxin. dual mechanism of binding to target cells. *J. Biol. Chem. 266*, 26 (1991), 17195–17200.

[114] Hille, B. *Ion Channels of Excitable Membranes*, 3 ed. Sinauer Associates, 2001.

[115] Högbom, J. A. Aperture synthesis with a non regular distribution of interferometer baselines. *Astronomy and Astrophysics Supp 15* (1974), 417.

[116] Holden, M. A., and Bayley, H. Direct introduction of single protein channels and pores into lipid bilayers. *J. Am. Chem. Soc. 127*, 18 (2005), 6502–6503.

[117] Holden, M. A., Jayasinghe, L., Daltrop, O., Mason, A., and Bayley, H. Direct transfer of membrane proteins from bacteria to planar bilayers for rapid screening by single-channel recording. *Nat. Chem. Biol. 2*, 6 (2006), 314–318.

[118] Holden, M. A., Needham, D., and Bayley, H. Functional bionetworks from nanoliter water droplets. *J. Am. Chem. Soc. 129* (2007), 8650–8655.

[119] Hoppe, W., Lohmann, W., Markl, H., and Ziegler, H. *Biophysics*. Springer-Verlag, 1983.

[120] Hotze, E. M., Heuck, A. P., Czajkowsky, D. M., Shao, Z., Johnson, A. E., and Tweten, R. K. Monomer-monomer interactions drive the prepore to pore conversion of a β-barrel-forming cholesterol-dependent cytolysin. *J. Biol. Chem. 277*, 13 (2002), 11597–11605.

[121] Hotze, E. M., Wilson-Kubalek, E. M., Rossjohn, J., Parker, M. W., Johnson, A. E., and Tweten, R. K. Arresting pore formation of a cholesterol-dependent cytolysin by disulfide trapping synchronizes the insertion of the transmembrane β-sheet from a prepore intermediate. *J. Biol. Chem. 276*, 11 (2001), 8261–8268.

[122] Howarth, M., Chinnapen, D. J.-F., Gerrow, K., Dorrestein, P. C., Grandy, M. R., Kelleher, N. L., El-Husseini, A., and Ting, A. Y. A monovalent

streptavidin with a single femtomolar biotin binding site. *Nat. Methods 3*, 4 (2006), 267–273.

[123] Howarth, M., Liu, W., Puthenveetil, S., Zheng, Y., Marshall, L. F., Schmidt, M. M., Wittrup, K. D., Bawendi, M. G., and Ting, A. Y. Monovalent, reduced-size quantum dots for imaging receptors on living cells. *Nat. Methods 5*, 5 (2008), 397–399.

[124] Howarth, M., Takao, K., Hayashi, Y., and Ting, A. Y. Targeting quantum dots to surface proteins in living cells with biotin ligase. *Proc. Natl. Acad. Sci. U.S.A. 102*, 21 (2005), 7583–7588.

[125] Humphrey, W., Dalke, A., and Schulten, K. VMD - Visual molecular dynamics. *J. Molec. Graphics 14* (1996), 33–38.

[126] Hung, L., K.M., C., Tseng, W., Tan, Y., Shea, K., and Lee, A. Alternating droplet generation and controlled dynamic droplet fusion in microfluidic device for CdS nanoparticle synthesis. *Lab Chip 6* (2006), 174–178.

[127] Husmann, M., Beckmann, E., Boller, K., Kloft, N., Tenzer, S., Bobkiewicz, W., Neukirch, C., Bayley, H., and Bhakdi, S. Elimination of a bacterial pore-forming toxin by sequential endocytosis and exocytosis. *FEBS Lett.* (2008), in press.

[128] Hwang, W. L., Chen, M., Cronin, B., Holden, M. A., and Bayley, H. Asymmetric droplet interface bilayers. *J. Am. Chem. Soc. 130*, 18 (2008), 5878–5879.

[129] Hwang, W. L., Holden, M. A., White, S., and Bayley, H. Electrical behavior of droplet interface bilayer networks: experimental analysis and modeling. *J. Am. Chem. Soc. 129*, 38 (2007), 11854–11864.

[130] Ichikawa, T., Aoki, T., Takeuchi, Y., Yanagida, T., and Ide, T. Immobilizing single lipid and channel molecules in artificial lipid bilayers with annexin A5. *Langmuir 22*, 14 (2006), 6302–6307.

[131] Ide, T., and Ichikawa, T. A novel method for artificial lipid-bilayer formation. *Biosens. Bioelectron. 21*, 4 (2005), 672–677.

[132] Ide, T., Takeuchi, Y., Aoki, T., and Yanagida, T. Simultaneous optical and electrical recording of a single ion-channel. *Jpn. J. Physiol. 52*, 5 (2002), 429–434.

[133] Ide, T., Takeuchi, Y., and Yanagida, T. Development of an experimental apparatus for simultaneous observation of optical and electrical signals from single ion channels. *Single Mol. 3* (2002), 33–42.

[134] Ide, T., and Yanagida, T. An artificial lipid bilayer formed on an agarose-coated glass for simultaneous electrical and optical measurement of single ion channels. *Biochemical and Biophysical Research Communications 265* (1999), 595–599.

[135] Ikigai, H., and Nakae, T. Conformational alteration in α-toxin from *Staphylococcus aureus* concomitant with the transformation of the water-soluble monomer to the membrane oligomer. *Biochem. Biophys. Res. Commun. 130*, 1 (1985), 175–181.

[136] Ikigai, H., and Nakae, T. Assembly of the α-toxin-hexamer of *Staphylococcus aureus* in the liposome membrane. *J. Biol Chem. 262*, 5 (1987), 2156–2160.

[137] Ikigai, H., and Nakae, T. Interaction of the α-toxin of *Staphylococcus aureus* with the liposome membrane. *J. Biol. Chem. 262*, 5 (1987), 2150–2155.

[138] Jayasinghe, L., and Bayley, H. The leukocidin pore: evidence for an octamer with four LukF subunits and four LukS subunits alternating around a central axis. *Protein Sci. 14*, 10 (2005), 2550–2561.

[139] Jayasinghe, L., Miles, G., and Bayley, H. Role of the amino latch of staphylococcal α-hemolysin in pore formation: a co-operative interaction between the N terminus and position 217. *J. Biol. Chem. 281*, 4 (2006), 2195–2204.

[140] Jiang, Y., Lee, A., Chen, J., Ruta, V., Cadene, M., Chait, B. T., and MacKinnon, R. X-ray structure of a voltage-dependent K^+ channel. *Nature 423*, 6935 (2003), 33–41.

[141] Joanicot, M., and Ajdari, A. Applied physics. Droplet control for microfluidics. *Science 309*, 5736 (2005), 887–888.

[142] Joo, C., Balci, H., Ishitsuka, Y., Buranachai, C., and Ha, T. Advances in single-molecule fluorescence methods for molecular biology. *Annu. Rev. Biochem. 77* (2008), 51–76.

[143] Jung, Y., Cheley, S., Braha, O., and Bayley, H. The internal cavity of the staphylococcal α-hemolysin pore accommodates approximately 175 exogenous amino acid residues. *Biochemistry 44*, 25 (2005), 8919–8929.

[144] Jursch, R., Hildebrand, A., Hobom, G., Tranum-Jensen, J., Ward, R., Kehoe, M., and Bhakdi, S. Histidine residues near the N terminus of staphylococcal α-toxin as reporters of regions that are critical for oligomerization and pore formation. *Infect. Immun. 62*, 6 (1994), 2249–2256.

[145] Kalia, J., and Raines, R. T. Catalysis of imido group hydrolysis in a maleimide conjugate. *Bioorg. Med. Chem. Lett. 17*, 22 (2007), 6286–6289.

[146] Kang, X.-F., Gu, L.-Q., Cheley, S., and Bayley, H. Single protein pores containing molecular adapters at high temperatures. *Angew. Chem. Int. Ed. Engl. 44*, 10 (2005), 1495–1499.

[147] Kapanidis, A. N., and Weiss, S. Fluorescent probes and bioconjugation chemistries for single-molecule fluorescence analysis of biomolecules. *J. Chem. Phys. 117*, 24 (2002), 10953–10964.

[148] Karginov, V. A., Nestorovich, E. M., Schmidtmann, F., Robinson, T. M., Yohannes, A., Fahmi, N. E., Bezrukov, S. M., and Hecht, S. M. Inhibition of *S. aureus* α-hemolysin and *B. anthracis* lethal toxin by β-cyclodextrin derivatives. *Bioorg. Med. Chem. 15*, 16 (2007), 5424–5431.

[149] Kasson, P. M., and Pande, V. S. Molecular dynamics simulation of lipid reorientation at bilayer edges. *Biophys. J. 86*, 6 (2004), 3744–3749.

[150] Katayama, H., Janowiak, B. E., Brzozowski, M., Juryck, J., Falke, S., Gogol, E. P., Collier, R. J., and Fisher, M. T. GroEL as a molecular scaffold for structural analysis of the anthrax toxin pore. *Nat. Struct. Mol. Biol. 15*, 7 (2008), 754–760.

[151] Kawate, T., and Gouaux, E. Arresting and releasing staphylococcal α-hemolysin at intermediate stages of pore formation by engineered disulfide bonds. *Protein Sci. 12*, 5 (2003), 997–1006.

[152] Keizer, H. M., Dorvel, B. R., Andersson, M., Fine, D., Price, R. B., Long, J. R., Dodabalapur, A., Koper, I., Knoll, W., Anderson, P. A. V., and Duran, R. S. Functional ion channels in tethered bilayer membranes–implications for biosensors. *Chembiochem 8*, 11 (2007), 1246–1250.

[153] Khan, M., and Khan, A. Kinetics and mechanism of hydrolysis of succinimide under highly alkaline medium. *J. Org. Chem. 40*, 12 (1975), 1793–1974.

[154] Kiessling, V., Crane, J. M., and Tamm, L. K. Transbilayer effects of raft-like lipid domains in asymmetric planar bilayers measured by single molecule tracking. *Biophys. J. 91*, 9 (2006), 3313–3326.

[155] Kim, Y., Ho, S. O., Gassman, N. R., Korlann, Y., Landorf, E. V., Collart, F. R., and Weiss, S. Efficient site-specific labeling of proteins via cysteines. *Bioconjug. Chem. 19*, 3 (2008), 786–791.

[156] Krasilnikov, O. V., Merzlyak, P. G., Yuldasheva, L. N., Rodrigues, C. G., Bhakdi, S., and Valeva, A. Electrophysiological evidence for heptameric stoichiometry of ion channels formed by *Staphylococcus aureus* α-toxin in planar lipid bilayers. *Mol. Microbiol. 37*, 6 (2000), 1372–1378.

[157] Krishnasastry, M., Walker, B., Braha, O., and Bayley, H. Surface labeling of key residues during assembly of the transmembrane pore formed by staphylococcal α-hemolysin. *FEBS Lett. 356*, 1 (1994), 66–71.

[158] Kühner, M., Tampé, R., and Sackmann, E. Lipid mono- and bilayer supported on polymer films: composite polymer-lipid films on solid substrates. *Biophys. J. 67*, 1 (1994), 217–226.

[159] Kumar, S., Locken, K., Kenyon, Y., and Lindorfer, R. Purification and properties of stphylococcal α-toxin. *J. Exptl. Med. 115* (1962), 1107–1115.

[160] Kusumi, A., Sako, Y., and Yamamoto, M. Confined lateral diffusion of membrane receptors as studied by single particle tracking (nanovid microscopy). effects of calcium-induced differentiation in cultured epithelial cells. *Biophys. J. 65*, 5 (1993), 2021–2040.

[161] Lacy, D. B., Wigelsworth, D. J., Melnyk, R. A., Harrison, S. C., and Collier, R. J. Structure of heptameric protective antigen bound to an anthrax toxin receptor: a role for receptor in ph-dependent pore formation. *Proc. Natl. Acad. Sci. U.S.A. 101*, 36 (2004), 13147–13151.

[162] Laemmli, U. Cleavage of structural proteins during the assembly of the head of bacteriophage T4. *Nature 227*, 5259 (1970), 680–685.

[163] Lakowicz, J. *Principles of Fluorescence Spectroscopy*, vol. 3. Springer Science+Business Media, LLC, 2006.

[164] Lampton, M. Damping-undamping strategies for the Levenberg-Marquardt nonlinear least-squares method. *Computers in Physics 11* (1997), 110–115.

[165] Leake, M. C., Chandler, J. H., Wadhams, G. H., Bai, F., Berry, R. M., and Armitage, J. P. Stoichiometry and turnover in single, functioning membrane protein complexes. *Nature 443*, 7109 (2006), 355–358.

[166] Leake, M. C., Wilson, D., Gautel, M., and Simmons, R. M. The elasticity of single titin molecules using a two-bead optical tweezers assay. *Biophys. J. 87*, 2 (2004), 1112–1135.

[167] Lenz, P., Ajo-Franklin, C., and Boxer, S. G. Patterned supported lipid bilayers and monolayers on poly(dimethylsiloxane). *Langmuir 20*, 25 (2004), 11092–11099.

[168] Link, D. R., Grasland-Mongrain, E., Duri, A., Sarrazin, F., Cheng, Z., Cristobal, G., Marquez, M., and Weitz, D. A. Electric control of droplets in microfluidic devices. *Angew. Chem. Int. Ed. Engl. 45*, 16 (2006), 2556–2560.

[169] Lommerse, P. H. M., Vastenhoud, K., Pirinen, N. J., Magee, A. I., Spaink, H. P., and Schmidt, T. Single-molecule diffusion reveals similar mobility for the Lck, H-ras, and K-ras membrane anchors. K-ras membrane anchors. *Biophys. J. 91*, 3 (2006), 1090–1097.

[170] Loots, E., and Isacoff, E. Y. Protein rearrangements underlying slow inactivation of the Shaker K^+ channel. *J. Gen. Physiol. 112*, 4 (1998 Oct), 377–389.

[171] Loudwig, S., and Bayley, H. Photoisomerization of an individual azobenzene molecule in water: an on-off switch triggered by light at a fixed wavelength. *J. Am. Chem. Soc. 128*, 38 (2006), 12404–12405.

[172] Luchian, T., Shin, S.-H., and Bayley, H. Single-molecule covalent chemistry with spatially separated reactants. *Angew. Chem. Int. Ed. Engl. 42*, 32 (2003), 3766–3771.

[173] Luirink, J., von Heijne, G., Houben, E., and de Gier, J.-W. Biogenesis of inner membrane proteins in *Escherichia coli*. *Annu. Rev. Microbiol. 59* (2005), 329–355.

[174] Lynch, A. S., and Robertson, G. T. Bacterial and fungal biofilm infections. *Annu. Rev. Med. 59* (2008), 415–428.

[175] Macdonald, A., and Wraight, P. Combined spectroscopic and electrical recording techniques in membrane research: prospects for single channel studies. *Prog. Biophys. Mol. Bio. 63* (1995), 1–29.

[176] Mahler, B., Spinicelli, P., Buil, S., Quelin, X., Hermier, J.-P., and Dubertret, B. Towards non-blinking colloidal quantum dots. *Nat. Mater. 7*, 8 (2008), 659–664.

[177] Malghani, M., Fang, Y., Cheley, S., Bayley, H., and Yang, J. Heptameric structures of two α-hemolysin mutants imaged with in situ atomic force microscopy. *Microscopy Res. Tech. 44*, 5 (1999), 353–356.

[178] Malmstadt, N., Nash, M. A., Purnell, R. F., and Schmidt, J. J. Automated formation of lipid-bilayer membranes in a microfluidic device. *Nano Lett. 6*, 9 (2006), 1961–1965.

[179] Mashanov, G. I., Tacon, D., Peckham, M., and Molloy, J. E. The spatial and temporal dynamics of pleckstrin homology domain binding at the plasma membrane measured by imaging single molecules in live mouse myoblasts. *J. Biol. Chem. 279*, 15 (2004), 15274–15280.

[180] McNiven, A. C., Owen, P., and Arbuthnott, J. P. Multiple forms of staphylococcal α-toxin. *J. Med. Microbiol. 5*, 1 (1972), 113–122.

[181] Melton, J. A., Parker, M. W., Rossjohn, J., Buckley, J. T., and Tweten, R. K. The identification and structure of the membrane-spanning domain of the clostridium septicum α toxin. *J. Biol. Chem. 279*, 14 (2004), 14315–14322.

[182] Menestrina, G. Ionic channels formed by *Staphylococcus aureus* α-toxin: voltage-dependent inhibition by divalent and trivalent cations. *J. Membr. Biol. 90*, 2 (1986), 177–190.

[183] Menzies, B. E., and Kernodle, D. S. Site-directed mutagenesis of the α-toxin gene of *Staphylococcus aureus*: role of histidines in toxin activity *in vitro* and in a murine model. *Infect. Immun. 62*, 5 (1994), 1843–1847.

[184] Miller, C. *Ion channel reconstitution*. Plenum Press: New York, 1986.

[185] Miller, C. J., Elliott, J. L., and Collier, R. J. Anthrax protective antigen: prepore-to-pore conversion. *Biochemistry 38*, 32 (1999), 10432–10441.

[186] Minta, A., Kao, J. P., and Tsien, R. Y. Fluorescent indicators for cytosolic calcium based on rhodamine and fluorescein chromophores. *J. Biol. Chem. 264*, 14 (1989), 8171–8178.

[187] Mohamed, N., Visai, L., Speziale, P., and Ross, J. M. Quantification of *Staphylococcus aureus* cell surface adhesins using flow cytometry. *Microb. Pathog. 29*, 6 (2000), 357–361.

[188] Mohanty, J., and Nau, W. M. Ultrastable rhodamine with cucurbituril. *Angew. Chem. Int. Ed. Engl. 44*, 24 (2005), 3750–3754.

[189] Molecular Devices. *The Axon Guide: A Guide to Electrophysiology and Biophysics Laboratory Techniques*, c ed. MDS Analytical Technologies, 2007.

[190] Monma, N., Nguyen, V. T., Kaneko, J., Higuchi, H., and Kamio, Y. Essential residues, W177 and R198, of LukF for phosphatidylcholine-binding and pore-formation by staphylococcal γ-hemolysin on human erythrocyte membranes. *J. Biochem. 136*, 4 (2004), 427–431.

[191] Montal, M., and Mueller, P. Formation of bimolecular membranes from lipid monolayers and a study of their electrical properties. *Proc. Natl. Acad. Sci. U.S.A. 69* (1972), 3561–3566.

[192] Montoya, M., and Gouaux, E. β-barrel membrane protein folding and structure viewed through the lens of α-hemolysin. *Biochim. Biophys. Acta 1609*, 1 (2003), 19–27.

[193] Mueller, P., Rudin, P., Tien, H., and Wescott, W. Reconstitution of cell membrane structure *in vitro* and its transformation into an excitable system. *Nature 194* (1962), 979–980.

[194] Murphy, S., and Schuster, G. Electronic relaxation in a series of cyanine dyes: Evidence for electronic and steric control of the rotational rate. *J. Phys. Chem. 99* (1995), 8516–8518.

[195] Murphy, S., Yang, X., and Schuster, G. Cyanine borate salts that form penetrated ion pairs in benzene solution: Synthesis, properties, and structure. *J. Org. Chem. 60*, 8 (1995), 2411–2422.

[196] Mutch, S., Fujimoto, B., Kuyper, C., Kuo, J., Bajjalieh, S., and Chiu, D. Deconvolving single-molecule intensity distributions for quantitative microscopy measurements. *Biophys. J. 92* (2007), 2926–2943.

[197] Neher, E., Sakmann, B., and Steinbach, J. H. The extracellular patch clamp: a method for resolving currents through individual open channels in biological membranes. *Pflugers Arch. 375*, 2 (1978), 219–228.

[198] Nguyen, A. H., Nguyen, V. T., Kamio, Y., and Higuchi, H. Single-molecule visualization of environment-sensitive fluorophores inserted into cell membranes by staphylococcal γ-hemolysin. *Biochemistry 45*, 8 (2006), 2570–2576.

[199] Nguyen, V. T., Higuchi, H., and Kamio, Y. Controlling pore assembly of staphylococcal γ-haemolysin by low temperature and by disulphide bond formation in double-cysteine LukF mutants. *Mol. Microbiol. 45*, 6 (2002), 1485–1498.

[200] Nguyen, V. T., Kamio, Y., and Higuchi, H. Single-molecule imaging of cooperative assembly of γ-hemolysin on erythrocyte membranes. *EMBO J. 22*, 19 (2003), 4968–4979.

[201] Noskov, S. Y., Im, W., and Roux, B. Ion permeation through the α-hemolysin channel: theoretical studies based on Brownian dynamics and Poisson-Nernst-Planck electrodiffusion theory. *Biophys. J. 87*, 4 (2004), 2299–2309.

[202] Ober, R. J., Ram, S., and Ward, E. S. Localization accuracy in single-molecule microscopy. *Biophys. J. 86*, 2 (2004), 1185–1200.

[203] Ohndorf, U.-M., and MacKinnon, R. Construction of a cyclic nucleotide-gated KcsA K^+ channel. *J. Mol. Biol. 350*, 5 (2005), 857–865.

[204] Olson, R., Nariya, H., Yokota, K., Kamio, Y., and Gouaux, E. Crystal structure of staphylococcal LukF delineates conformational changes accompanying formation of a transmembrane channel. *Nat. Struct. Biol. 6*, 2 (1999), 134–140.

[205] Overington, J. P., Al-Lazikani, B., and Hopkins, A. L. How many drug targets are there? *Nat. Rev. Drug Discovery 5*, 12 (2006), 993–996.

[206] Palchevskyy, S. S., Posokhov, Y. O., Olivier, B., Popot, J.-L., Pucci, B., and Ladokhin, A. S. Chaperoning of insertion of membrane proteins into lipid bilayers by hemifluorinated surfactants: application to diphtheria toxin. *Biochemistry 45*, 8 (2006), 2629–2635.

[207] Palzkill, T. *Proteomics*. Kluwer Academic Publishers: Boston/London, 2002.

[208] Panchal, R. G., and Bayley, H. Interactions between residues in staphylococcal α-hemolysin revealed by reversion mutagenesis. *J. Biol. Chem. 270*, 39 (1995), 23072–23076.

[209] Park, K.-H., Berrier, C., Lebaupain, F., Pucci, B., Popot, J.-L., Ghazi, A., and Zito, F. Fluorinated and hemifluorinated surfactants as alternatives to detergents for membrane protein cell-free synthesis. *Biochem. J. 403*, 1 (2007), 183–187.

[210] Pattee, P. A. Chromosomal map location of the α-hemolysin structural gene in *Staphylococcus aureus* NCTC 8325. *Infect. Immun. 54*, 2 (1986), 593–596.

[211] Pautot, S., Frisken, B. J., and Weitz, D. A. Engineering asymmetric vesicles. *Proc. Natl. Acad. Sci. U.S.A. 100*, 19 (2003), 10718–10721.

[212] Pedelacq, J. D., Maveyraud, L., Prevost, G., Baba-Moussa, L., Gonzalez, A., Courcelle, E., Shepard, W., Monteil, H., Samama, J. P., and Mourey, L. The structure of a *Staphylococcus aureus* leucocidin component (LukF-PV) reveals

the fold of the water-soluble species of a family of transmembrane pore-forming toxins. *Structure 7*, 3 (1999), 277–287.

[213] Pedelacq, J. D., Prevost, G., Monteil, H., Mourey, L., and Samama, J. P. Crystal structure of the F component of the Panton-Valentine leucocidin. Panton-Valentine leucocidin. *Int. J. Med. Microbiol. 290*, 4-5 (2000), 395–401.

[214] Perez, J.-B., Segura, J.-M., Abankwa, D., Piguet, J., Martinez, K. L., and Vogel, H. Monitoring the diffusion of single heterotrimeric G proteins in supported cell-membrane sheets reveals their partitioning into microdomains. *J. Mol. Biol. 363*, 5 (2006), 918–930.

[215] Plugge, B., Gazzarrini, S., Nelson, M., Cerana, R., Van Etten, J. L., Derst, C., DiFrancesco, D., Moroni, A., and Thiel, G. A potassium channel protein encoded by chlorella virus PBCV-1. *Science 287*, 5458 (2000), 1641–1644.

[216] Pohle, W., Selle, C., Gauger, D. R., and Brandenburg, K. Lyotropic phase transitions in phospholipids as evidenced by small-angle synchrotron X-ray scattering. *J. Biomol. Struct. Dyn. 19*, 2 (2001), 351–364.

[217] Porath, J., Carlsson, J., Olsson, I., and Belfrage, G. Metal chelate affinity chromatography, a new approach to protein fractionation. *Nature 258*, 5536 (1975), 598–599.

[218] Poulos, J., Jeon, T., Damoiseaux, R., Gillespie, E., Bradley, K., and Schmidt, J. Ion channel and toxin measurement using a high throughput lipid membrane platform. *Biosens. Bioelectron.* (2008), in press.

[219] Qian, H., Sheetz, M. P., and Elson, E. L. Single particle tracking. Analysis of diffusion and flow in two-dimensional systems. *Biophys. J. 60*, 4 (1991), 910–921.

[220] Raedler, J., Strey, H., and Sackmann, E. Phenomenology and kinetics of lipid bilayer spreading on hydrophilic surfaces. *Langmuir 11*, 11 (1995), 4539–4548.

[221] Rasmussen, S. G. F., Choi, H.-J., Rosenbaum, D. M., Kobilka, T. S., Thian, F. S., Edwards, P. C., Burghammer, M., Ratnala, V. R. P., Sanishvili, R., Fischetti, R. F., Schertler, G. F. X., Weis, W. I., and Kobilka, B. K.

Crystal structure of the human β2 adrenergic G-protein-coupled receptor. *Nature 450*, 7168 (2007), 383–387.

[222] Rasnik, I., McKinney, S. A., and Ha, T. Nonblinking and long-lasting single-molecule fluorescence imaging. *Nat. Methods 3*, 11 (2006), 891–893.

[223] RCSB. PDB statistics, January 2009.

[224] Reviakine, I., and Brisson, A. Formation of supported phospholipid bilayers from unilamellar vesicles investigated by atomic force microscopy. *Langmuir 16*, 4 (2000), 1806–1815.

[225] Richter, R., Bérat, R., and Brisson, A. Formation of solid-supported lipid bilayers: An integrated view. *Langmuir 22* (2006), 3497–3505.

[226] Richter, R., Mukhopadhyay, A., and Brisson, A. Pathways of lipid vesicle deposition on solid surfaces: a combined QCM-D and AFM study. *Biophys. J. 85*, 5 (2003), 3035–3047.

[227] Rodnin, M., Posokhov, Y., Contino-Pepin, C., Brettman, J., Kyrychenko, A., Palchevskyy, S., Pucci, B., and Ladokhin, A. Interactions of fluorinated surfactants with diphtheria A toxin T-domain: Testing new media for studies of membrane proteins. *Biophys. J.* (2008).

[228] Sakmann, B., and Neher, E. *Single-channel recording.* Plenum Press: New York/London, 1995.

[229] Sandison, M. E., Zagnoni, M., and Morgan, H. Air-exposure technique for the formation of artificial lipid bilayers in microsystems. *Langmuir 23*, 15 (2007), 8277–8284.

[230] Santelli, E., Bankston, L. A., Leppla, S. H., and Liddington, R. C. Crystal structure of a complex between anthrax toxin and its host cell receptor. *Nature 430*, 7002 (2004), 905–908.

[231] Sauerwein, B., Murphy, S., and Schuster, G. Dynamics of solute motion: photoisomerization shows a linear dependence on solvent mass. *J. Am. Chem. Soc. 114*, 20 (1992), 7920–7922.

[232] Saxton, M. J. Single-particle tracking: the distribution of diffusion coefficients. *Biophys. J. 72*, 4 (1997), 1744–1753.

[233] Saxton, M. J., and Jacobson, K. Single-particle tracking: applications to membrane dynamics. *Annu. Rev. Biophys. Biomol. Struct. 26* (1997), 373–399.

[234] Sbalzarini, I. F., and Koumoutsakos, P. Feature point tracking and trajectory analysis for video imaging in cell biology. *J. Struct. Biol. 151*, 2 (2005), 182–195.

[235] Schmidt, T., Schütz, G. J., Baumgartner, W., Gruber, H. J., and Schindler, H. Imaging of single molecule diffusion. *Proc. Natl. Acad. Sci. U.S.A. 93*, 7 (1996), 2926–2929.

[236] Schoch, P., Sargent, D. F., and Schwyzer, R. Capacitance and conductance as tools for the measurement of asymmetric surface potentials and energy barriers of lipid bilayer membranes. *J. Membr. Biol. 46*, 1 (1979), 71–89.

[237] Schuster, B., Pum, D., Braha, O., Bayley, H., and Sleytr, U. B. Self-assembled α-hemolysin pores in an S-layer-supported lipid bilayer. *Biochim. Biophys. Acta 1370*, 2 (1998), 280–288.

[238] Schütz, G. J., Schindler, H., and Schmidt, T. Single-molecule microscopy on model membranes reveals anomalous diffusion. *Biophys. J. 73* (1997), 1073–1080.

[239] Scott, D. On optimal and data-based histrograms. *Biometrika 66* (1979), 605–610.

[240] Shafer, D. E., Inman, J. K., and Lees, A. Reaction of tris(2-carboxyethyl)phosphine (TCEP) with maleimide and α-haloacyl groups: anomalous elution of TCEP by gel filtration. *Anal. Biochem. 282*, 1 (2000), 161–164.

[241] Shchipunov, Y., and Schmiedel, P. Phase behavior of lecithin at the oil/water interface. *Langmuir 12*, 26 (1996), 6443–6445.

[242] Shimomura, O., Johnson, F. H., and Saiga, Y. Extraction, purification and properties of aequorin, a bioluminescent protein from the luminous hydromedusan, Aequorea. *J. Cell. Comp. Physiol. 59* (1962), 223–239.

[243] Shin, S.-H., and Bayley, H. Stepwise growth of a single polymer chain. *J. Am. Chem. Soc. 127*, 30 (2005), 10462–10463.

[244] Simpson, R. J. *Proteins and Proteomics: a laboratory manual*. Cold Spring Harbor Laboratory Press: Cold Spring Harbor, NY, 2003.

[245] Smal, I., Niessen, W., and Meijering, E. Bayesian tracking for fluorescence microscopic imaging. *IEEE Conference Proceeding: 3rd IEEE International Symposium on Biomedical Imaging: Macro to Nano* (2006), 550–553.

[246] Smal, I., Niessen, W., and Meijering, E. Particle filtering for multiple object tracking in molecular cell biology. *Nonlinear Statistical Signal Processing Workshop* (2006), 44.1–44.4.

[247] Smal, I., Niessen, W., and Meijering, E. Advanced particle filtering for multiple object tracking in dynamic fluorescence microscopy images. *IEEE Conference Proceeding: 4th IEEE International Symposium on Biomedical Imaging: Nano to Macro* (2007), 1048–1051.

[248] Smedley, J. G., Sharp, J. S., Kuhn, J. F., and Tomer, K. B. Probing the pH-dependent prepore to pore transition of *Bacillus anthracis* protective antigen with differential oxidative protein footprinting. *Biochemistry 47*, 40 (2008), 10694–10704.

[249] Song, L., Hobaugh, M. R., Shustak, C., Cheley, S., Bayley, H., and Gouaux, J. E. Structure of staphylococcal α-hemolysin, a heptameric transmembrane pore. *Science 274*, 5294 (1996), 1859–1866.

[250] Sonnleitner, A., Schutz, G., and Schmidt, T. Free brownian motion of individual lipid molecules in biomembranes. *Biophys. J. 77*, 5 (1999), 2638–2642.

[251] Sowa, Y., and Berry, R. M. Bacterial flagellar motor. *Q. Rev. Biophys. 41*, 2 (2008), 103–132.

[252] Studier, F. W., and Moffatt, B. A. Use of bacteriophage T7 RNA polymerase to direct selective high-level expression of cloned genes. *J. Mol. Biol. 189*, 1 (1986), 113–130.

[253] Sugawara, N., Tomita, T., Sato, T., and Kamio, Y. Assembly of *Staphylococcus aureus* leukocidin into a pore-forming ring-shaped oligomer on human polymorphonuclear leukocytes and rabbit erythrocytes. *Biosci. Biotechnol. Biochem. 63* (1999), 884–891.

[254] Suzuki, H., Tabata, K., Noji, H., and Takeuchi, S. Highly reproducible method of planar lipid bilayer reconstitution in polymethyl methacrylate microfluidic chip. *Langmuir 22*, 4 (2006), 1937–1942.

[255] Suzuki, H., Tabata, K., Noji, H., and Takeuchi, S. Electrophysiological recordings of single ion channels in planar lipid bilayers using a polymethyl methacrylate microfluidic chip. *Biosens. Bioelectron. 22*, 6 (2007), 1111–1115.

[256] Syeda, R., Holden, M. A., Hwang, W. L., and Bayley, H. Screening blockers against a potassium channel with a droplet interface bilayer array. *J. Am. Chem. Soc. 130*, 46 (2008), 15543–15548.

[257] Tamm, L. Membrane insertion and lateral mobility of synthetic amphiphilic signal peptides in lipid model membranes. *Biochim. Biophys. Acta 1071* (1991), 123–148.

[258] Tamm, L. K., and McConnell, H. M. Supported phospholipid bilayers. *Biophys. J. 47*, 1 (1985), 105–113.

[259] Tanaka, M., and Sackmann, E. Polymer-supported membranes as models of the cell surface. *Nature 437*, 7059 (2005), 656–663.

[260] Tanford, C. *The Hydrophobic Effect: Formation of Micelles and Biological Membranes*. John Wiley Sons Inc, 1983.

[261] Thelestam, M., and Blomqvist, L. Staphylococcal α-toxin - recent advances. *Toxicon 26*, 1 (1988), 55–65.

[262] Thompson, A. R., Moran, J. M., and Swenson, G. W. *Interferometry and synthesis in radio astronomy*. Wiley-Interscience, New York, 2001.

[263] Thompson, J. R., Heron, A. J., Santoso, Y., and Wallace, M. I. Enhanced stability and fluidity in droplet on hydrogel bilayers for measuring membrane protein diffusion. *Nano Lett. 7*, 12 (2007), 3875–3878.

[264] Thompson, N. L., Pearce, K. H., and Hsieh, H. V. Total internal reflection fluorescence microscopy: application to substrate-supported planar membranes. *Eur. Biophys. J. 22*, 5 (1993), 367–378.

[265] Thompson, R. E., Larson, D. R., and Webb, W. W. Precise nanometer localization analysis for individual fluorescent probes. *Biophys. J. 82* (2002), 2775–2783.

[266] Thorsen, T., Roberts, R. W., Arnold, F. H., and Quake, S. R. Dynamic pattern formation in a vesicle-generating microfluidic device. *Phys. Rev. Lett. 86*, 18 (2001), 4163–4166.

[267] Tilley, S. J., Orlova, E. V., Gilbert, R. J. C., Andrew, P. W., and Saibil, H. R. Structural basis of pore formation by the bacterial toxin pneumolysin. *Cell 121*, 2 (2005), 247–256.

[268] Tobkes, N., Wallace, B. A., and Bayley, H. Secondary structure and assembly mechanism of an oligomeric channel protein. *Biochemistry 24*, 8 (1985), 1915–1920.

[269] Toyama, S., Nakamura, A., and Toda, F. Measurement of voltage dependence of capacitance of planar bilayer lipid membrane with a patch clamp amplifier. *Biophys J. 59*, 4 (1991), 939–944.

[270] Tsofina, L. M., Liberman, E. A., and Babakov, A. V. Production of bimolecular protein-lipid membranes in aqueous solution. *Nature 212*, 681-683 (1966).

[271] Tsukazaki, T., Mori, H., Fukai, S., Ishitani, R., Mori, T., Dohmae, N., Perederina, A., Sugita, Y., Vassylyev, D. G., Ito, K., and Nureki, O. Conformational transition of Sec machinery inferred from bacterial SecYE structures. *Nature 455*, 7215 (2008), 988–991.

[272] Ulmschneider, M. B., Sansom, M. S. P., and Di Nola, A. Properties of integral membrane protein structures: derivation of an implicit membrane potential. *Proteins 59*, 2 (2005), 252–265.

[273] Valeur, B. *Molecular Fluorescence: Principles and Applications.* Wiley-VCH Verlag GmbH, 2002.

[274] Valeva, A., Palmer, M., Hilgert, K., Kehoe, M., and Bhakdi, S. Correct oligomerization is a prerequisite for insertion of the central molecular domain of staphylococcal α-toxin into the lipid bilayer. *Biochim. Biophys. Acta 1236*, 2 (1995), 213–218.

[275] Valeva, A., Walev, I., Pinkernell, M., Walker, B., Bayley, H., Palmer, M., and Bhakdi, S. Transmembrane β-barrel of staphylococcal α-toxin forms in sensitive but not in resistant cells. *Proc. Natl. Acad. Sci. U.S.A. 94*, 21 (1997), 11607–11611.

[276] Valeva, A., Weisser, A., Walker, B., Kehoe, M., Bayley, H., Bhakdi, S., and Palmer, M. Molecular architecture of a toxin pore: a 15-residue sequence lines the transmembrane channel of staphylococcal α-toxin. *EMBO J. 15*, 8 (1996), 1857–1864.

[277] Vaz, W. L., and Almeida, P. F. Microscopic versus macroscopic diffusion in one-component fluid phase lipid bilayer membranes. *Biophys. J. 60* (1991), 1553–1554.

[278] Vijayvargia, R., Kaur, S., Sangha, N., Sahasrabuddhe, A. A., Surolia, I., Shouche, Y., and Krishnasastry, M. V. Assembly of α-hemolysin on A431 cells leads to clustering of Caveolin-1. *Biochem. Biophys. Res. Commun. 324*, 3 (2004), 1124–1129.

[279] Vockenroth, I. K., Atanasova, P. P., Jenkins, A. T. A., and Koper, I. Incorporation of α-hemolysin in different tethered bilayer lipid membrane architectures. *Langmuir 24*, 2 (2008), 496–502.

[280] Vockenroth, I. K., Atanasova, P. P., Long, J. R., Jenkins, A. T. A., Knoll, W., and Koper, I. Functional incorporation of the pore forming segment of AChR M2 into tethered bilayer lipid membranes. *Biochim. Biophys. Acta 1768*, 5 (2007), 1114–1120.

[281] Wagner, M. L., and Tamm, L. K. Reconstituted Syntaxin1A/SNAP25 interacts with negatively charged lipids as measured by lateral diffusion in planar supported bilayers. *Biophys. J. 81* (2001), 226–275.

[282] Walker, B., and Bayley, H. A pore-forming protein with a protease-activated trigger. *Protein Eng. 7*, 1 (1994), 91–97.

[283] Walker, B., and Bayley, H. Key residues for membrane binding, oligomerization, and pore forming activity of staphylococcal α-hemolysin identified by cysteine scanning

mutagenesis and targeted chemical modification. *J. Biol. Chem. 270*, 39 (1995), 23065–23071.

[284] Walker, B., and Bayley, H. Restoration of pore-forming activity in staphylococcal α-hemolysin by targeted covalent modification. *Protein Eng. 8*, 5 (1995), 491–495.

[285] Walker, B., Braha, O., Cheley, S., and Bayley, H. An intermediate in the assembly of a pore-forming protein trapped with a genetically-engineered switch. *Chem. Biol. 2*, 2 (1995), 99–105.

[286] Walker, B., Kasianowicz, J., Krishnasastry, M., and Bayley, H. A pore-forming protein with a metal-actuated switch. *Protein Eng. 7*, 5 (1994), 655–662.

[287] Walker, B., Krishnasastry, M., and Bayley, H. Functional complementation of staphylococcal α-hemolysin fragments. overlaps, nicks, and gaps in the glycine-rich loop. *J. Biol. Chem. 268*, 7 (1993), 5285–5292.

[288] Walker, B., Krishnasastry, M., Zorn, L., and Bayley, H. Assembly of the oligomeric membrane pore formed by staphylococcal α-hemolysin examined by truncation mutagenesis. *J. Biol. Chem. 267*, 30 (1992), 21782–21786.

[289] Walker, B., Krishnasastry, M., Zorn, L., Kasianowicz, J., and Bayley, H. Functional expression of the α-hemolysin of *Staphylococcus aureus* in intact *Escherichia coli* and in cell lysates. Deletion of five C-terminal amino acids selectively impairs hemolytic activity. *J. Biol. Chem. 267*, 15 (1992), 10902–10909.

[290] Wang, S. Q., Song, L. S., Lakatta, E. G., and Cheng, H. Ca^{2+} signalling between single L-type Ca^{2+} channels and ryanodine receptors in heart cells. *Nature 410*, 6828 (2001), 592–596.

[291] Watanabe, M., Tomita, T., and Yasuda, T. Membrane-damaging action of staphylococcal α-toxin on phopholipid-cholesterol liposomes. *Biochim. Biophys. Acta 898* (1987), 256–265.

[292] Wessendorf, M. W., and Brelje, T. C. Which fluorophore is brightest? A comparison of the staining obtained using fluorescein, tetramethylrhodamine, lissamine rhodamine, Texas red, and cyanine 3.18. *Histochemistry 98*, 2 (1992), 81–85.

[293] White, S. Membrane proteins of known 3D structure, January 2009. http://blanco.biomol.uci.edu/Membrane_Proteins_xtal.html.

[294] White, S. H. *Ion channel reconstitution*. Plenum Press: New York/London, 1986.

[295] Wong, J. Y., Majewski, J., Seitz, M., Park, C. K., Israelachvili, J. N., and Smith, G. S. Polymer-cushioned bilayers. I. A structural study of various preparation methods using neutron reflectometry. *Biophys. J. 77*, 3 (1999), 1445–1457.

[296] Wooley, G. Channel-forming activity of alamethicin: Effects of covalent tethering. *Chem. Biodiv. 4* (2007), 1323–1337.

[297] Xie, X. S., and Trautman, J. K. Optical studies of single molecules at room temperature. *Annu. Rev. Phys. Chem. 49* (2004), 441–480.

[298] Xie, X. S., Yu, J., and Yang, W. Y. Living cells as test tubes. *Science 312*, 5771 (2006), 228–230.

[299] Yau, C. M. S., Pascu, S. I., Odom, S. A., Warren, J. E., Klotz, E. J. F., Frampton, M. J., Williams, C. C., Coropceanu, V., Kuimova, M. K., Phillips, D., Barlow, S., Bredas, J.-L., Marder, S. R., Millar, V., and Anderson, H. L. Stabilisation of a heptamethine cyanine dye by rotaxane encapsulation. *Chem. Commun.*, 25 (2008), 2897–2899.

[300] Yildiz, A., Forkey, J. N., McKinney, S. A., Ha, T., Goldman, Y. E., and Selvin, P. R. Myosin V walks hand-over-hand: Single fluorophore imaging with 1.5-nm localization. *Science 300*, 5628 (2003), 2061–2065.

[301] Young, J. A. T., and Collier, R. J. Anthrax toxin: receptor binding, internalization, pore formation, and translocation. *Annu. Rev. Biochem. 76* (2007), 243–265.

[302] Zheng, J., and Zagotta, W. N. Patch-clamp fluorometry recording of conformational rearrangements of ion channels. *Sci STKE 2003*, 176 (2003), PL7.

[303] Zou, H., Lifshitz, L. M., Tuft, R. A., Fogarty, K. E., and Singer, J. J. Visualization of Ca^{2+} entry through single stretch-activated cation channels. *Proc. Natl. Acad. Sci. U.S.A. 99*, 9 (2002), 6404–6409.

Chapter 8

Appendix

8.1 Gene Sequences

The sequences of the genes used in this work:

α-Hemolysin Wild-Type

A D S D I N I K T G T T D I G S N T T V K T G D L V T Y D K E N G M H
K K V F Y S F I D D K N H N K K L L V I R T K G T I A G Q Y R V Y S E E G A N
K S G L A W P S A F K V Q L Q L P D N E V A Q I S D Y Y P R N S I D T K E Y M
S T L T Y G F N G N V T G D D T G K I G G L I G A N V S I G H T L K Y V Q P D
F K T I L E S P T D K K V G W K V I F N N M V N Q N W G P Y D R D S W N P V
Y G N Q L F M K T R N G S M K A A D N F L D P N K A S S L L S S G F S P D F A
T V I T M D R K A S K Q Q T N I D V I Y E R V R D D Y Q L H W T S T N W K G
T N T K D K W T D R S S E R Y K I D W E K E E M T N

α-Hemolysin T292C-Long Linker-H_6

A D S D I N I K T G T T D I G S N T T V K T G D L V T Y D K E N G M H
K K V F Y S F I D D K N H N K K L L V I R T K G T I A G Q Y R V Y S E E G A N
K S G L A W P S A F K V Q L Q L P D N E V A Q I S D Y Y P R N S I D T K E Y M
S T L T Y G F N G N V T G D D T G K I G G L I G A N V S I G H T L K Y V Q P D

F K T I L E S P T D K K V G W K V I F N N M V N Q N W G P Y D R D S W N P V Y G N Q L F M K T R N G S M K A A D N F L D P N K A S S L L S S G F S P D F A T V I T M D R K A S K Q Q T N I D V I Y E R V R D D Y Q L H W T S T N W K G T N T K D K W T D R S S E R Y K I D W E K E E M C N R G S G S S S G G S S H H H H H H

α-Hemolysin 294C-Short Linker-H_6

A D S D I N I K T G T T D I G S N T T V K T G D L V T Y D K E N G M H K K V F Y S F I D D K N H N K K L L V I R T K G T I A G Q Y R V Y S E E G A N K S G L A W P S A F K V Q L Q L P D N E V A Q I S D Y Y P R N S I D T K E Y M S T L T Y G F N G N V T G D D T G K I G G L I G A N V S I G H T L K Y V Q P D F K T I L E S P T D K K V G W K V I F N N M V N Q N W G P Y D R D S W N P V Y G N Q L F M K T R N G S M K A A D N F L D P N K A S S L L S S G F S P D F A T V I T M D R K A S K Q Q T N I D V I Y E R V R D D Y Q L H W T S T N W K G T N T K D K W T D R S S E R Y K I D W E K E E M T N C S S H H H H H H

8.2 Apparatus Details

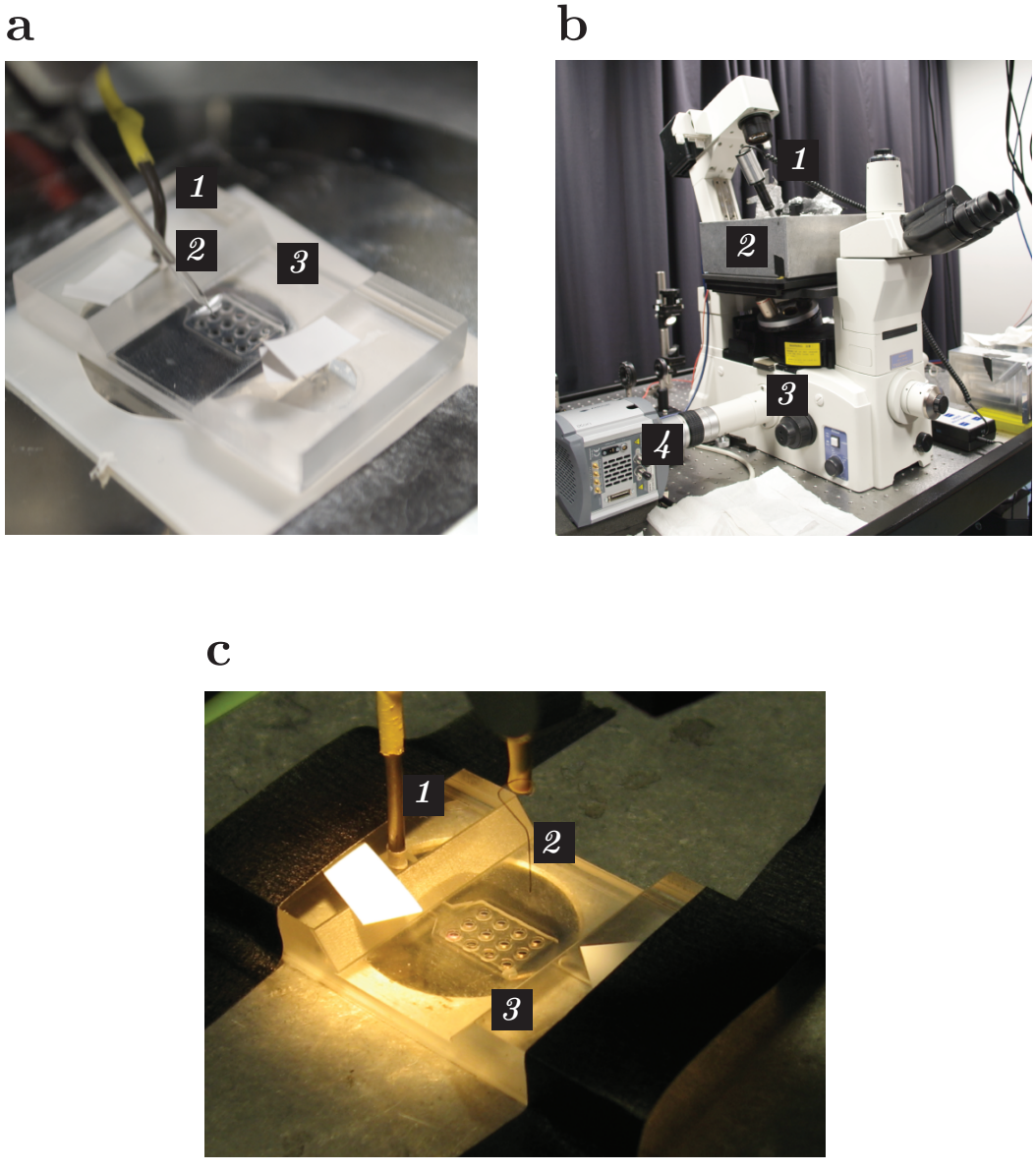

Figure 8.1: *Images showing DHB experimental apparatus. (A) 1 - A nanoinjection capillary in the vicinity of the DHB device. 2 - The ground Ag/AgCl electrode connecting to the substrate gel. 3 - The DHB device attached to the bottom of the Faraday cage. (B) 1 - The nanoinjector attached to a micro-manipulator attached within the faraday cage (2). 3 - The inverted microscope. 4 - The emCCD detector attached to the microscope. (C) 1 - The ground Ag/AgCl electrode connecting to the substrate gel. 2 - The 100 µm Ag/AgCl electrode used for electrical measurements inside droplets. 3 - the DHB device attached to the bottom of the Faraday cage.*

8.3 Patch-Clamp Amplification Details

The patch-clamp amplifier used in these experiments is essentially a low-noise and high-bandwidth current to voltage converter (I-V converter). The means to measure a picoampere current, such as is yielded in these experiments, is to measure the voltage drop across a large resistor. This is achieved through the use of a rapid and precise voltage-controlled voltage source, an op-amp. The op-amp in the probe acts to keep the voltage at its two inputs equalised, *i.e.* the probe electrode and the ground electrode. The limited bandwidth afforded by the feedback-resistor element is overcome through the use of a boost circuit, whose gain is proportional to the frequency. A diagram of such a circuit is shown 8.2. Thereafter the signals are digitised before being recorded to a computer.

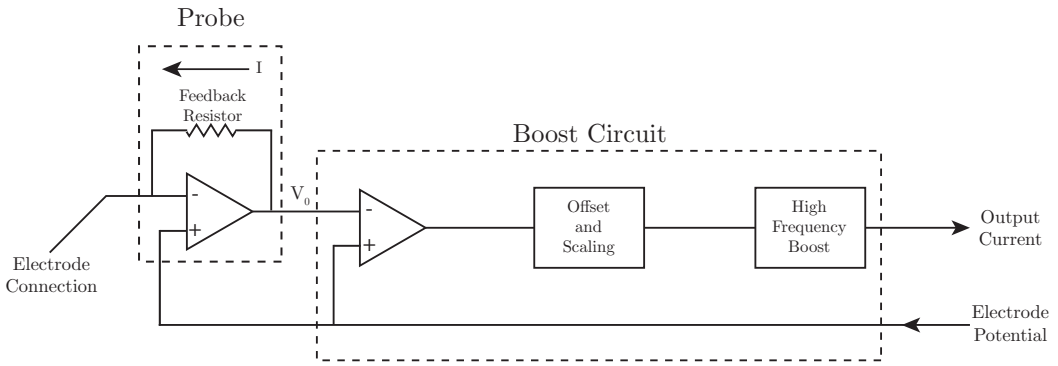

Figure 8.2: *A diagram of the resistive mode of the head-stage (Molecular Devices - CV 203BU) employed in the amplification of picoampere currents in single-channel resolution electrical recordings in this work. The op-amp in the probe acts to keep the voltage at its two inputs equalised. Hence, the voltage at its negative input equals the electrode potential, hence the feedback resistor voltage is V_0 minus the electrode potential, which is calculated by a differential amplifier maintained in the control box sequence of amplifiers. Later amplifiers add signal gain for the A-D process and remove voltage offsets. The circuit diagrams of the actual components used in this apparatus are proprietary and were unavailable for publication within this work.*